NASA Contractor Report 198389

A Computational Fluid Dynamic and Heat Transfer Model for Gaseous Core and Gas Cooled Space Power and Propulsion Reactors

S. Anghaie and G. Chen
University of Florida
Gainesville, Florida

April 1996

Prepared for
Lewis Research Center
Under Contract NAS3–26314

National Aeronautics and
Space Administration

TABLE OF CONTENTS

page

LIST OF SYMBOLS

English Symbols

A	pipe cross-sectional area
a	maximum eigenvalue
a_R	Rosseland mean opacity
c	speed of sound
C_p	specific heat at constant pressure
C_v	specific heat at constant volume
D	diameter
D_h	hydraulic diameter
e	total energy per unit volume
f_z	distance correction of Nusselt number
f_p	property correction of Nusselt number
h	enthalpy or heat transfer coefficient
k	thermal conductivity
I	unit matrix
l , L	pipe length
m	mass flow rate
Nu	Nusselt number, hD/k
p	pressure
Pr	Prandtl number, $C_p\mu/k$
q_c''	conductive heat flux
q_r''	radiative heat flux

q''_w wall heat flux

q''_t total heat flux

q''' volumetric heat generation rate

Q total heat flux

Q uniform heat generation

r radial position measured from the centerline

R pipe radius

gas constant

Re Reynolds number, uL/ν

t time

T temperature

T_s surrounding temperature

u axial velocity, z-component

v radial velocity, r-component

z axial position measured from the pipe entrance

Greek Symbols

α void parameter

β clustering parameter

δ Delta number $k\Delta T/(q\ D_h\alpha^2)$

δ_b thickness of laminar sublayer

δ_v velocity residual

δ_T temperature residual

ε internal energy

γ ratio of specific heats, C_p/C_v

η positioning parameter

Φ function of separation angle

κ	Boltzmann constant
μ	dynamic viscosity
ν	kinematic viscosity, μ/ρ
ρ	density
σ	Stefan-Boltzmann constant
σ_{ph}	photon collision cross section
τ	shear stress
$\|\omega\|$	magnitude of vorticity

Subscripts

1	inside wall boundary mesh point
2	inside fluid boundary mesh point
b	bulk conditions
c	convective components
e	eddy components
i	axial mesh point locations
j	radial mesh point locations
m	molecular component
	average
r	radial locations
	radiation components
t	turbulent component
w	wall conditions
z	axial locations

CHAPTER 1
INTRODUCTION

1.1 Motivation for the Heat Transfer Modeling

Numerical heat transfer is a key issue in nuclear reactor analysis. For a high temperature energy conversion system, energy from the nuclear fission process is transferred to the coolant system by conduction, convection and radiation. This study is especially focused on numerical analysis to solve the heat transfer problems in nuclear reactor core design, which include the Heterogeneous Gaseous Core Reactor [HGCR], High Temperature Gas Cooled Reactor [HTGR] and the XNR2000 nuclear rocket. Table 1-1 presents the applications of numerical modeling.

Table 1-1 Applications of numerical modeling.

Reactor	Fluid Flow	Heat Transfer	Thermal Boundary
HGCR	UF_4 gas	Convection & Radiation	Gas deposits heat to wall
HTGR	Helium gas	Convection	Gas removes heat from wall
XNR2000	Hydrogen gas	Convection	Gas removes heat from wall

A Heterogeneous Gas Core Reactor uses a gaseous fissile material as fuel for power generation.[13] This allows for power generation at temperatures much higher than the melting point of solid fuel nuclear reactors. Power generation and power conversion at very high temperatures can potentially reduce the system mass and improve the specific impulse performance of a nuclear thermal rocket. One of the most challenging issues related to design and operation of gas core reactors is the containment of the high

temperature fissioning plasma. The wall cooling is the most important issue in design of gaseous core nuclear reactors. The heat transfer process involved in an ultrahigh temperature gas core reactor systems is characterized by the convective flow of a radiating gas. Uranium compound gases at pressures in the range of 10 to 40 atm are optically thick. At temperatures close to 3500°K which is the typical exit temperature of the reactor core in a more recent design, the radiative heat transfer rate in these opaque gases is higher and comparable with the convective heat transfer rate.[37] Therefore, the heat transfer analysis of a fissioning gas must include both convective and radiative transfer. The flow and radiation transport equations must be solved simultaneously in order to determine the temperature distribution and heat transfer rate. Figure 1-1 shows the high temperature vapor reactor with advanced energy conversion system.

The HTGR primary system is composed of several loops, each housed within a large cylinder of prestressed concrete.[44] The flow is directed downward through the core by a circulator mounted above the steam generator in the cold leg. The reactor vessel and steam generator are connected by a short, horizontal cross duct. The coolant from the core exit plenum is directed laterally through the interior of the cross duct into the inlet of the steam generator. Coolant from the steam generator and circulator is directed laterally through the outer annulus of the cross duct into the core inlet plenum. The HTGR primary coolant flow path is illustrated in Figure 1-2.

XNR2000 is an expander cycle nuclear rocket engine powered by a fast-spectrum cermet-fueled nuclear reactor that heats hydrogen to a maximum propellant temperature.[4] The reactor is comprised of an outer annulus core of Mo-UO_2 prismatic fuel elements and a cylindrical inner core of W-UO_2 prismatic fuel elements. The baseline XNR2000 reactor core consists of a total of 151 prismatic fuel elements of 55 cm in active length. The core is arranged such that an inner-outer core configuration is obtained with 61 inner core fuel elements and 90 outer core fuel elements.[14] The purpose of inner-outer core configuration is to provide a folded flow path for the

hydrogen propellant flowing upward through the outer core and downward through the inner core. The XNR2000 coolant flow path is shown in Figure 1-3.

1.2 Computational Method for CFD and Heat Transfer

The development of heat transfer modeling has been a major area of research for several decades in the nuclear thermal hydraulics field. Most people attribute the first definitive Computational Fluid Dynamics (CFD) work to Richardson in 1910, who introduced point iterative schemes for numerically solving Laplace's equation and bihamonic equation. He clearly defined the difference between problems which must be solved by a relaxation scheme. In 1918, Liebmann presented an improved version of Richadson's method. Liebmann's methods used values of the dependent variable both at the new and old iteration level in each sweep through the computational grid. The beginning of modern numerical analysis is attributed to a famous paper by Courant, Fredrichs and lewy,[1] the CFL, frequently seen in the literature. In that paper, uniqueness and existence questions were addressed for the numerical solutions of partial differential equations. It is original source for the CFL stability requirement for the numerical solution of hyperbolic partial differential equations. However, limits to the above method still existed for steady-state and low temperature conditions at that time.

In 1940, Southwell introduced a relaxation scheme which was used in solving fluid dynamic problems where an improved relaxation scheme was required. During the decades of 1940s and 1950s, Southwell's methods were generally the first numerical techniques introduced to engineers. Allen applied Southwell's scheme to solve the incompressible, viscous flow over a cylinder. They used the empirical or semi-empirical information, wall function for the heat transfer studies.[46] However, this approach is too sensitive to the near wall grids and inaccurate at the flow separation region. Therefore, a highly-stretched fine grid near wall boundaries is required to solve unsteady and turbulent

flow problems. Unfortunately, the fine grid yields computational difficulties in terms of the stability limitation and the computation time. To remove the time step limitation, the fully-implicit numerical schemes were developed in the mid-1970's by Briley and McDonald.[7]

Professor John von Neumann developed his method for evaluating the stability of numerical methods for solving time-marching problems. O'Brien, Hyman and Kaplan later presented a detailed description of von Neumann method. This paper is significant because it presents a practical way of evaluating stability. At same time, progress was being made on the development of methods for both elliptic and parabolic problems. Peaceman and Rachford developed a new family of implicit method for parabolic and elliptic equations in which sweep directions were alternated and the allowed step size was unrestricted.[20] But those methods cannot be used to handle the discontinuity problems, such as shock capture problem. It was difficult to solve transonic and supersonic fluid flow problems.

Early efforts at solving flows with shock waves were part of Lax's approach.[9] Lax and Wendroff introduced a method for computing flows with shocks which was a second-order scheme that avoided the excessive smearing of earlier approaches. MacCormack has devised an implicit scheme that requires only the inversion of block bidiagonal systems rather than block tridiagonal systems, thus yielding savings in computer time and storage requirements. During the past 20 years, the explicit methods were developed to solve the compressible Navier-Stokes equations which include the Hopscotch method, DuFort-Frankel method, Brailovskaya method, Allen-Cheng method, Lax-Wendroff method and the MacCormack method.[17] All of above methods, except the MacCormack scheme, are first-order accurate so that they cannot be used to accurately compute the time evolution of a flow field.[23] In addition, all of the methods have a stability restriction which limits the maximum time step. The allowable time step is given by the CFL condition, which for 2-D problem becomes

$$(\Delta t)_{CFL} \leq \frac{\Delta z}{|u|+|v|+2\sqrt{a}}$$

where a is the maximum eigenvalue. For the other schemes, analytical stability conditions cannot be obtained[20] and a numerical investigation is presented in Figure 1-4. In this graph, the schemes are stable in the region below the corresponding curve. Figure 1-4 shows that the MacCormack method presents the best stability.

The MacCormack is the most popular two-step Lax-Wendroff method for solving problems with shock-capturing schemes.[8] This method is designed to solve time-dependent equations such as the complete Navier-Stokes equations without any artificial dissipation term or limiters. It is based on the second-order accurate explicit predictor-corrector method but adds an implicit procedure in the predictor-corrector sequence for points at which the local CFL number exceeds the stability limit. The method has been applied to two-dimensional internal supersonic flows, two-dimensional external flows, external axisymmetric flows and three-dimensional flows over a biconic body with a compression flap.[28] This scheme was applied to either the complete or thin layer forms of unsteady Navier-Stokes equations.

MacCormack's method is one of the most efficient of the second-order schemes from point of view of operation count. This approach is well adopted for time-dependent problems; it should be inserted in a multi-grid framework. The investigations on multi-grid Lax-Wendroff-type schemes can be found in reference [17].

The important conclusion is that among all second-order viscous Lax-Wendroff schemes, MacCormack scheme, with flux splitted operators, presents the best stability, consistency and efficiency.[25]

1.3 Objective and Overview

The main objective of this study is to develop a computational fluid dynamics and heat transfer model for convective, conductive and radiative heat transfer in high power density gas cooled and gaseous core nuclear reactors and the XNR2000 nuclear rocket core. To achieve this goal axisymmetric, thin-layer Navier-Stokes equations associated with 1-D integral approximation, Rosseland's diffusion approximation and algebraic 2-layer eddy viscosity turbulence model are used to simulate heat transfer in nuclear reactor cores. An implicit-explicit, finite volume, MacCormack method in conjunction with Gauss-Seidel line iteration procedure is utilized to solve the governing equations. An enthalpy-rebalancing scheme is implemented to allow the convergence solutions to be obtained with the applications of a wall heat flux. A two-dimensional method based on finite element technique is used to investigate the geometric behavior of a nuclear reactor fuel elements.

Chapter 2 describes MacCormack implicit-explicit model, Lomax and Baldwin's two-layer algebraic turbulence model, Rosseland's diffusion model, wall heat transfer model, enthalpy rebalancing scheme and the thermal conduction model. Chapter 3 provides the thermophysical properties of dissociated hydrogen, helium and UF_4 gases. Chapter 4 presents the assessment and validation of the numerical model with separation angle and drag force calculations around a sphere suspended in a cylinder, and heat transfer correlation comparison. Chapter 5 presents the applications of numerical models in gaseous core reactors, gas-cooled reactors and the XNR2000 nuclear rocket cores. Finally, the conclusions of this thesis are described in Chapter 6.

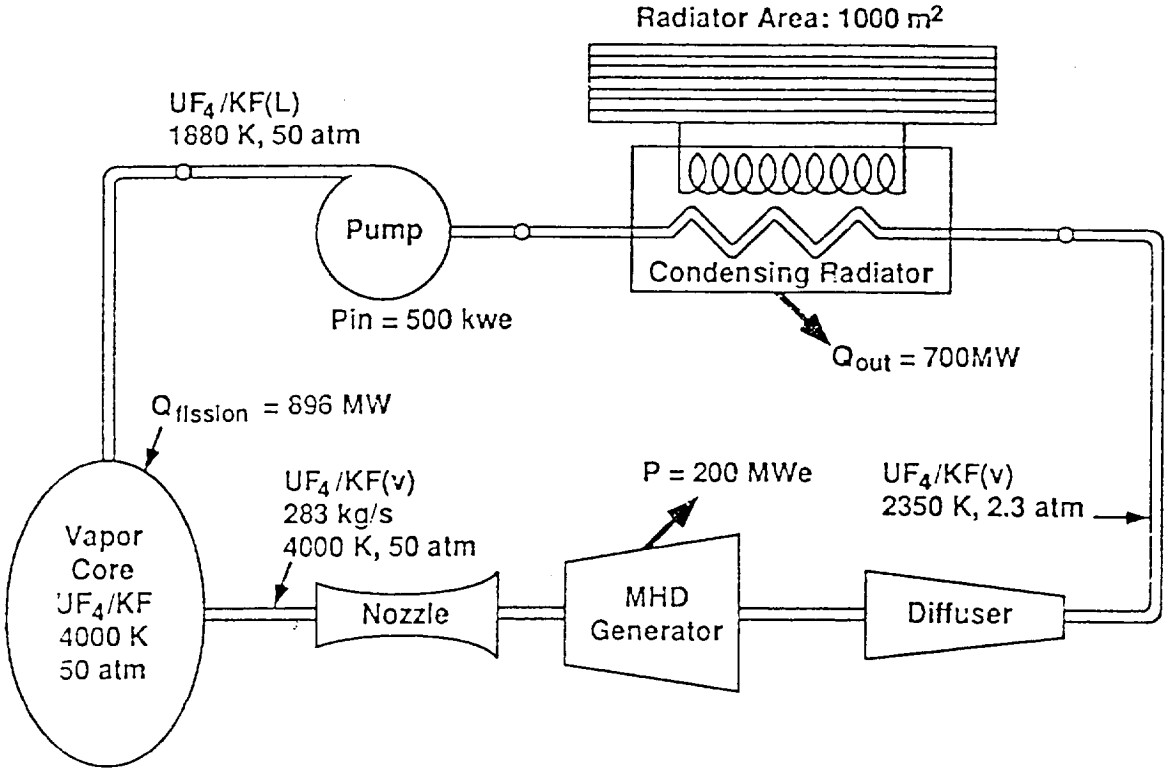

Figure 1-1 Gaseous core reactor with MHD generator space power system ([From Reference [13]).

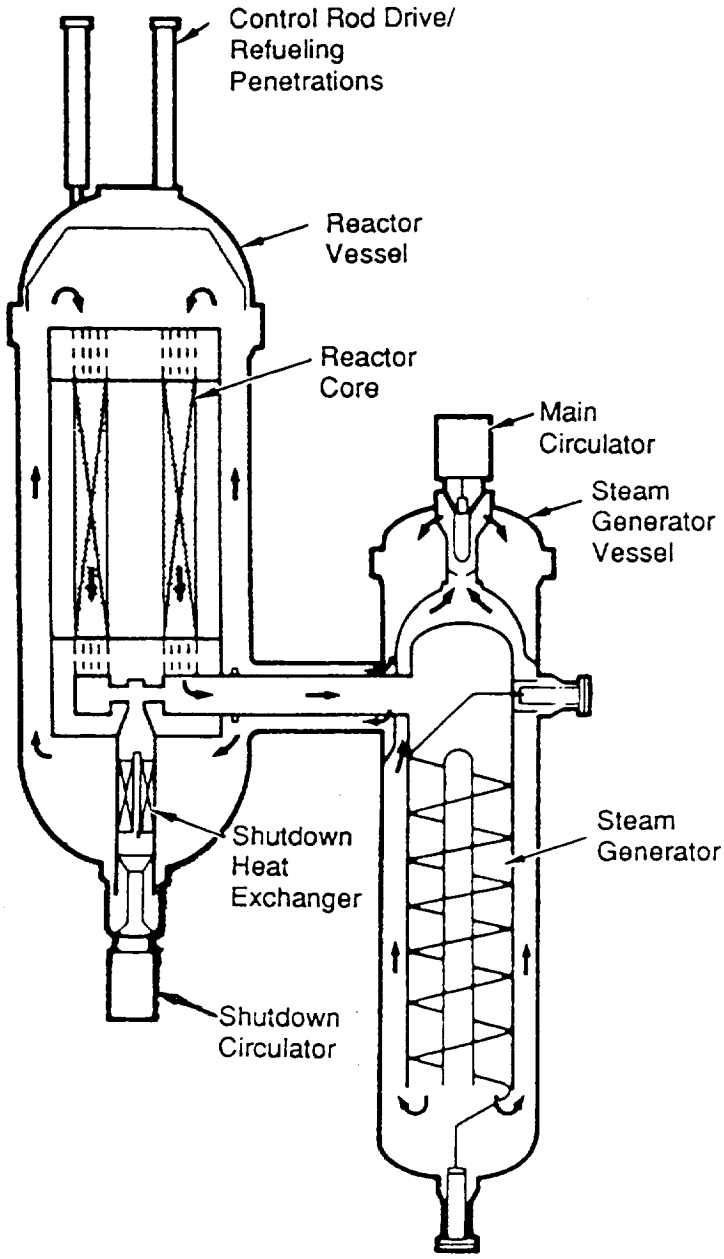

Figure 1-2 HTGR primary coolant flow path (From Reference [44]).

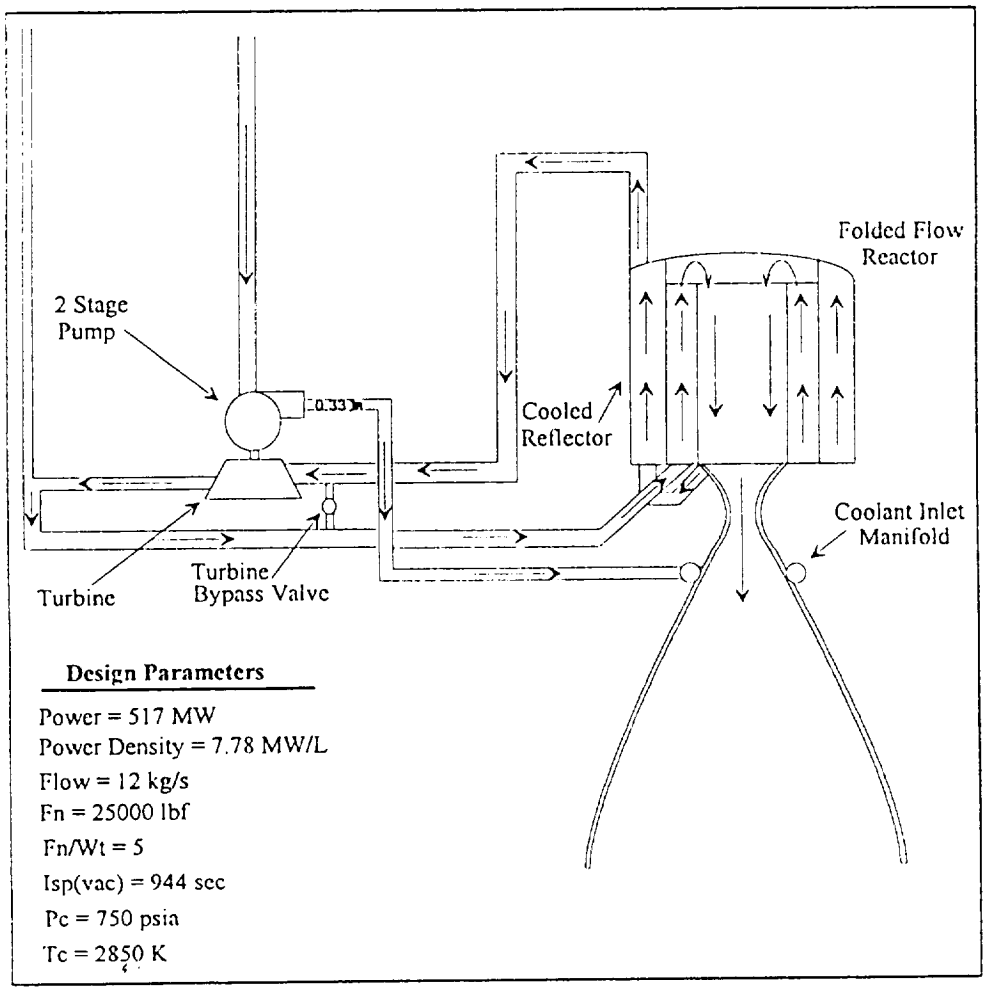

Figure 1-3 XNR2000 coolant flow path (From Reference [14]).

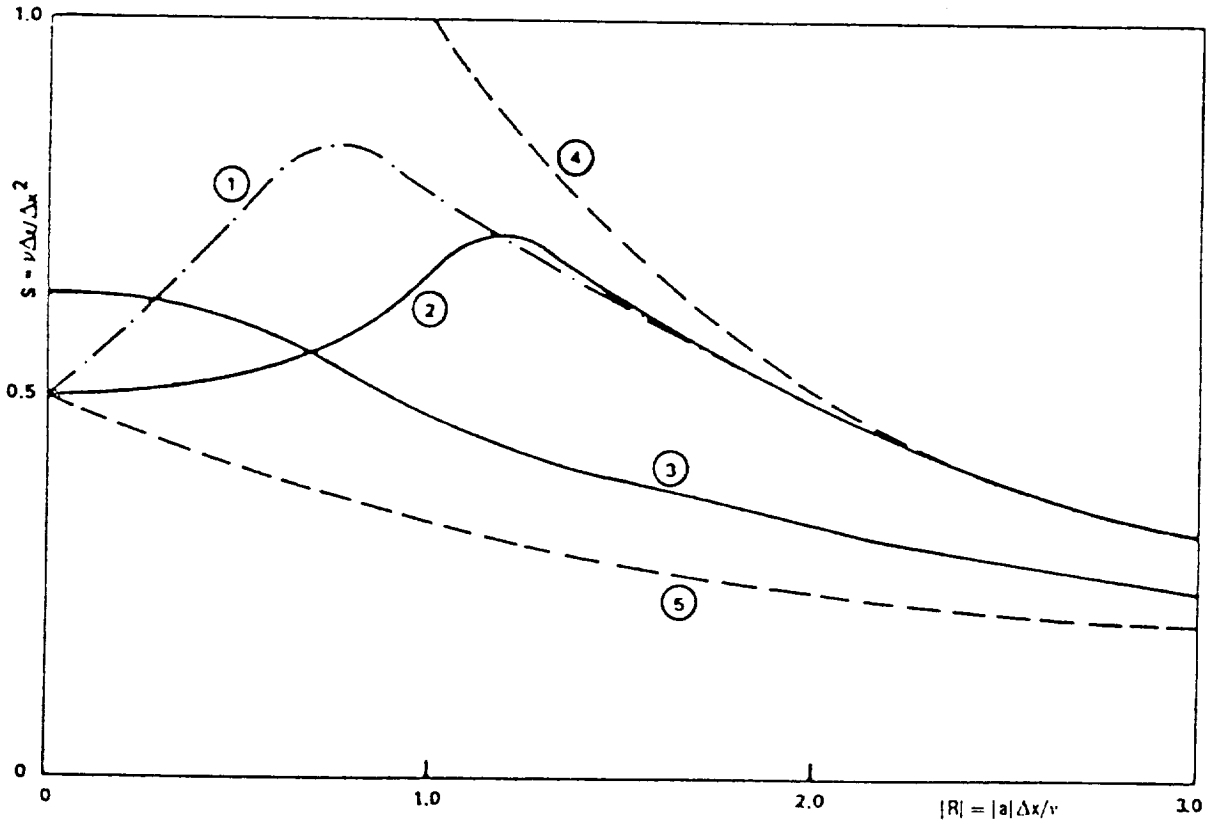

1- Richtmyer scheme
2- MacCormack scheme
3- Lerat-Peyret scheme
4- The CFD condition σ=1
5- Von Neumann scheme

Figure 1-4 Comparison of stability limits for the second-order schemes (From Reference [20]).

CHAPTER 2
NUMERICAL MODELING

2.1 Governing Equations

Combined convective and radiative heat transfer of simultaneously developing turbulent flow in a smooth circular tube with nongray gases is numerically modeled. Based on the physical considerations, the two-dimensional axisymmetric thin-layer compressible Navier-Stokes equations in strong conservation law form with Rosseland's approximation radiative heat transfer model and the algebraic two-layer eddy viscosity turbulence model are used to simulate the fluid flow and heat transfer in the gas core reactor. In order to derive the governing equations, the following assumption are made:[10]

1. The axial viscous dissipation and thermal radiation are negligible compared with the radial viscous dissipation and thermal radiation.

2. The axial heat conduction is negligible.

3. The gas absorbs and emits radiation but does not scatter.

4. The wall is a gray diffuse emitter and reflector.

5. There is no dissociation or phase change for UF_4 gas in the high temperature range.

Based on these assumptions, the time-dependent, mass-averaged and compressible Navier-Stokes equations in strong conservative and axisymmetric form are given as:[28]

$$\frac{\partial \overline{U}_i}{\partial t} + \frac{\partial \overline{F}_i}{\partial z} + \frac{\partial \overline{G}_i}{\partial r} = \frac{\partial \overline{G}_v}{\partial r} + \overline{H} \tag{2-1}$$

where

$$\overline{U}_i = \begin{bmatrix} \rho \\ \rho u \\ \rho v \\ e \end{bmatrix} \quad \overline{F}_i = \begin{bmatrix} \rho u \\ \rho u^2 + P \\ \rho uv \\ (e+P)u \end{bmatrix} \quad \overline{G}_i = \begin{bmatrix} \rho v \\ \rho uv \\ \rho v^2 + P \\ (e+P)v \end{bmatrix} \tag{2-2}$$

and the viscous and thermal source terms are

$$\overline{G}_v = \begin{bmatrix} 0 \\ \mu_T \dfrac{\partial u}{\partial r} \\ 4\dfrac{\mu_T}{3}\dfrac{\partial v}{\partial r} - \dfrac{2}{3}\mu_T \dfrac{v}{r} \\ \mu_T u \dfrac{\partial u}{\partial r} + \dfrac{4}{3}\mu_T v \dfrac{\partial v}{\partial r} - q_c'' - q_r'' \end{bmatrix} \tag{2-3}$$

and

$$\overline{H} = \begin{bmatrix} 0 \\ 0 \\ 0 \\ \dot{Q} \end{bmatrix} \tag{2-4}$$

In the above formulas,[43] u and v are the velocity components in z and r directions, respectively, ρ is the density, P is the pressure, μ_T is the total viscosity, q''_c is the conductive heat flux, and e is the total energy per unit volume which is related to the internal energy ε and kinetic energy.

$$e = \rho\left[\varepsilon + \frac{1}{2}\left(u^2 + v^2\right)\right] \tag{2-5}$$

The total viscosity μ is given as the sum of its molecular component μ_m and eddy component μ_e:

$$\mu = \mu_m + \mu_e \tag{2-6}$$

The eddy viscosity is obtained from the turbulent eddy viscosity model proposed by Baldwin and Lomax.[5] The heat flux term includes the conductive heat flux term, q_c'', and radiative heat flux term, q_r''. Based on Fourier's law, the conductive heat flux can be written as:

$$q_c'' = -k_c \frac{dT}{dr} \tag{2-7}$$

where

$$k_c = C_P\left(\frac{\mu_m}{P} + \frac{\mu_e}{P}\right) \tag{2-8}$$

Typical values of the molecular and turbulent Prandtl number at standard condition are 0.9 and 0.72, respectively. The radiative heat flux term is presented in a later section.

The complete set of Navier-Stokes equations (2-1) includes one continuity equation, two momentum equations, and one energy equation. In order to get six unknowns, ρ (density), u (axial velocity component), v(radial velocity component), e (total energy per unit volume), P (pressure) and T (temperature), two more supplement equations which are given by perfect gas law are required. Under perfect gas law, there are the following relations:

$$P = \rho RT \quad \varepsilon = C_v T \quad h = C_p T \quad \gamma = \frac{C_p}{C_v} \tag{2-9}$$

when using above relations, two additional equations are obtained as follows:

$$P = (\gamma - 1)\left[e - \frac{1}{2}\rho(u^2 + v^2)\right] \tag{2-10}$$

$$T = \frac{(\gamma - 1)}{R}\left[\frac{e}{\rho} - \frac{1}{2}(u^2 + v^2)\right] \tag{2-11}$$

Hence, combining above equations (2-1), (2-10) and (2-11), a set of governing equations is formed.

The Navier-Stokes equations are the coupled nonlinear mixed hyperbolic-parabolic system of partial differential equations. At high Reynolds number condition, these equations become stiff and are difficult to solve. Reynolds number is a measure of the ratio of the inertial to the viscous forces of a fluid. The viscous terms which cause the system to be parabolic are of the order of the reciprocal of the Reynolds number in magnitude. At high Reynolds number the system is almost everywhere hyperbolic, the viscous terms are negligible except in the boundary layers. Within these layers, the viscous terms are significant and control the important phenomenon of boundary layer separation. The disparity in magnitude at high Reynolds number between the inertial and viscous terms causes the system to be mathematically stiff. The only way to solve the complete Navier-Stokes equations is numerical procedure which will be discussed in the later sections.

2.2 Numerical Procedure

A hybrid implicit-explicit numerical method based on the finite volume discretization approach is used for computer implementation. The finite volume method

uses the integral forms of conservation equations on the finite cells. The equations are approximated by summing the fluxes of mass, momentum and energy from neighboring cells into each cell, thereby partial differential equations are changed to the discrete equations.

To derive an implicit form, equation (2-1) is differentiated with respect to time , t,

$$\frac{\partial\left(\frac{\partial U}{\partial t}\right)}{\partial t}+\frac{\partial A_i\left(\frac{\partial U}{\partial t}\right)}{\partial z}+\frac{\partial B_i\left(\frac{\partial U}{\partial t}\right)}{\partial r}=\frac{\partial B_v\left(\frac{\partial U}{\partial t}\right)}{\partial r}+\frac{\partial H}{\partial t} \tag{2-12}$$

where A_i, B_i and B_v are the Jacobians of F_i, G_i and G_v with respect to U, they are,

$$A_i=\frac{\partial F_i}{\partial U} \tag{2-13}$$

$$B_i=\frac{\partial G_i}{\partial U} \tag{2-14}$$

$$B_v=\frac{\partial G_v}{\partial U} \tag{2-15}$$

Letting

$$\Delta t\left(\frac{\partial U}{\partial t}\right)^n=\Delta U^n \tag{2-16}$$

$$\Delta t\left(\frac{\partial H}{\partial t}\right)^n=\Delta H^n \tag{2-17}$$

$$\Delta t\left(\frac{\partial U}{\partial t}\right)^{n+1}=\delta U^{n+1} \tag{2-18}$$

an implicit difference approximation to Equation (2-12) is

$$\left[I + \Delta t \frac{D.A}{\Delta z} + \Delta t \frac{D.B}{\Delta r} \right]_{i,j} \delta U_{i,j}^{n+1} = \Delta U_{i,j}^{n} + \Delta H_{i,j}^{n} \tag{2-19}$$

where

$$A = A_i$$
$$B = B_i - B_v$$

In the above equation, D indicates a difference operator. The forward difference operator D_+ and the backward difference operator D_-, are represented as follows:

$$D_+(A)_{i,j} = (A)_{i+1,j} - (A)_{i,j} \tag{2-20}$$

$$D_+(A)_{i,j} = (A)_{i,j+1} - (A)_{i,j} \tag{2-21}$$

$$D_-(A)_{i,j} = (A)_{i,j} - (A)_{i-1,j} \tag{2-22}$$

$$D_-(A)_{i,j} = (A)_{i,j} - (A)_{i,j-1} \tag{2-23}$$

In order to more realistically approximate the physics of the governing equations, improve efficiency for the implicit scheme and reduce the numerical errors, a flux vector splitting technique is used in this study. Steger and Warming pointed out that[41]

$$F = AU \tag{2-24}$$

and

$$G = BU \tag{2-25}$$

The Jacobian matrixes A and B con be diagonalized by similarity transformation S_x and S_y as follows

$$A = S_x^{-1} w^{-1} \begin{bmatrix} u & 0 & 0 & 0 \\ 0 & u+c & 0 & 0 \\ 0 & 0 & u & 0 \\ 0 & 0 & 0 & u-c \end{bmatrix} w S_x \tag{2-26}$$

$$B = S_y^{-1} w^{-1} \begin{bmatrix} v & 0 & 0 & 0 \\ 0 & v & 0 & 0 \\ 0 & 0 & v+c & 0 \\ 0 & 0 & 0 & v-c \end{bmatrix} w S_y \tag{2-27}$$

with

$$S_x = \begin{bmatrix} 1 & 0 & 0 & -1/c^2 \\ 0 & \rho c & 0 & 1 \\ 0 & 0 & 1 & 0 \\ 0 & -\rho c & 0 & 1 \end{bmatrix} \tag{2-28}$$

$$S_y = \begin{bmatrix} 1 & 0 & 0 & -1/c^2 \\ 0 & 1 & 0 & 0 \\ 0 & 0 & \rho c & 1 \\ 0 & 0 & -\rho c & 1 \end{bmatrix} \tag{2-29}$$

$$w = \begin{bmatrix} 1 & 0 & 0 & 0 \\ -u/\rho & 1/\rho & 0 & 0 \\ -v/\rho & 0 & 1/\rho & 0 \\ \alpha\beta & -u\beta & -v\beta & \beta \end{bmatrix} \tag{2-30}$$

where c is the speed of sound, $\alpha=1/2(u^2+v^2)$, $\beta=\gamma-1$, and γ is the ratio of the specific heats of the gases. In general some of the elements of the diagonalized matrix above are

positive and others are negative. Their signs determine the direction of information travel. So we can define the following matrices:[26,27]

$$
\begin{aligned}
A &= A_+ + A_- \\
&= S_x^{-1} w^{-1} \begin{bmatrix} \frac{u+|u|}{2} & 0 & 0 & 0 \\ 0 & \frac{u+c+|u+c|}{2} & 0 & 0 \\ 0 & 0 & \frac{u+|u|}{2} & 0 \\ 0 & 0 & 0 & \frac{u-c+|u-c|}{2} \end{bmatrix} w S_x + \\
&\quad S_x^{-1} w^{-1} \begin{bmatrix} \frac{u-|u|}{2} & 0 & 0 & 0 \\ 0 & \frac{u+c-|u+c|}{2} & 0 & 0 \\ 0 & 0 & \frac{u-|u|}{2} & 0 \\ 0 & 0 & 0 & \frac{u-c-|u-c|}{2} \end{bmatrix} w S_x
\end{aligned} \tag{2-31}
$$

$$
\begin{aligned}
B &= B_+ + B_- \\
&= S_y^{-1} w^{-1} \begin{bmatrix} \frac{v+|v|}{2} & 0 & 0 & 0 \\ 0 & \frac{v+|v|}{2} & 0 & 0 \\ 0 & 0 & \frac{v+c+|v+c|}{2} & 0 \\ 0 & 0 & 0 & \frac{v-c+|v-c|}{2} \end{bmatrix} w S_y + \\
&\quad S_y^{-1} w^{-1} \begin{bmatrix} \frac{v-|v|}{2} & 0 & 0 & 0 \\ 0 & \frac{v-|v|}{2} & 0 & 0 \\ 0 & 0 & \frac{v+c-|v+c|}{2} & 0 \\ 0 & 0 & 0 & \frac{v-c-|v-c|}{2} \end{bmatrix} w S_y
\end{aligned} \tag{2-32}
$$

Using the direction of information travel, the flux crossing the surface separating volumes i,j and i+1,j is

$$F_{i+1/2,j} = A_{+}U_{i,j} + A_{-}U_{i+1,j} \tag{2-33}$$

$$G_{i+1/2,j} = B_{+}U_{i,j} + B_{-}U_{i+1,j} \tag{2-34}$$

Considering the flux vector splitting technique and performing the operations indicated in Equation (2-19), we obtain the following equation in terms of block matrices C_1, C_2, C_3, C_4 and C_5:

$$C_2\delta U_{i,j+1} + C_1\delta U_{i,j} + C_3\delta U_{i,j-1} + C_4\delta U_{i+1,j} + C_5\delta U_{i-1,j} = \Delta U^n_{i,j} + \Delta H^n_{i,j} \tag{2-35}$$

where

$$C_1 = I + \Delta t\left(\frac{A_{+}}{\Delta z}i-1/2,j+\frac{A_{-}}{\Delta z}i+1/2,j\right)+$$
$$\Delta t\left(\frac{B_{-}}{\Delta r}i,j-1/2+\frac{B_{+}}{\Delta r}i,j+1/2+\frac{M_r N}{\Delta r^2}i,j-1/2+\frac{M_r N}{\Delta r^2}i,j+1/2\right)$$

$$C_2 = -\Delta t\left(\frac{B_{-}}{\Delta r}i,j+1/2+\frac{M_r N}{\Delta r^2}i,j+1/2\right)$$

$$C_3 = -\Delta t\left(\frac{B_{+}}{\Delta r}i,j-1/2+\frac{M_r N}{\Delta r^2}i,j-1/2\right)$$

$$C_4 = -\Delta t\left(\frac{A_{-}}{\Delta z}i+1/2,j\right)$$

$$C_5 = -\Delta t\left(\frac{A_+}{\Delta z} i-1/2, j\right)$$

$$M_r = \begin{bmatrix} 0 & 0 & 0 & 0 \\ 0 & \mu & 0 & 0 \\ 0 & 0 & \lambda+2\mu & 0 \\ 0 & u\mu & v(\lambda+2\mu) & \kappa \end{bmatrix}$$

$$N = \begin{bmatrix} 1 & 0 & 0 & 0 \\ \frac{-u}{\rho} & \frac{1}{\rho} & 0 & 0 \\ \frac{-v}{\rho} & 0 & \frac{1}{\rho} & 0 \\ \frac{\alpha - ei}{\rho} & \frac{-u}{\rho} & \frac{-v}{\rho} & \frac{1}{\rho} \end{bmatrix}$$

Equation (2-35) can be solved by line Gauss-Seidel iteration with alternating sweeps in the backward and forward z-directions,[29] as shown in Figure 2-1.

For k=1,3, ...

Backward Sweep:

$$C_2\delta U^k_{i,j+1} + C_1\delta U^k_{i,j} + C_3\delta U^k_{i,j-1} + C_4\delta U^k_{i+1,j} + C_5\delta U^{k-1}_{i-1,j} = \Delta U^n_{i,j} + \Delta H^n_{i,j} \qquad (2\text{-}36)$$

and

For k=2, 4, ...

Forward Sweep:

$$C_2\delta U^{k+1}_{i,j+1} + C_1\delta U^{k+1}_{i,j} + C_3\delta U^{k+1}_{i,j-1} + C_4\delta U^{k}_{i+1,j} + C_5\delta U^{k+1}_{i-1,j} = \Delta U^n_{i,j} + \Delta H^n_{i,j} \qquad (2\text{-}37)$$

The above implicit block matrix equation can be put the following form:

$$\begin{bmatrix} (C_2)_{jl} & (C_1)_{jl} & (C_3)_{jl} & & & & \\ & \ddots & & & & & \\ & & \ddots & & & & \\ & & (C_2)_j & (C_1)_j & (C_3)_j & & \\ & & & \ddots & & & \\ & & & & \ddots & & \\ & & & & (C_2)_2 & (C_1)_2 & (C_3)_2 \\ & & & & & -E & I \end{bmatrix} \begin{bmatrix} \delta U_{i,jl} \\ \vdots \\ \vdots \\ \delta U_{i,j} \\ \vdots \\ \vdots \\ \delta U_{i,2} \\ \delta U_{i,1} \end{bmatrix} = \begin{bmatrix} \Delta U_{i,jl} + \Delta H_{i,jl} - (C_4)_{i,jl}\delta U_{i+1,jl} - (C_5)_{i,jl}\delta U_{i-1,jl} \\ \vdots \\ \Delta U_{i,j} + \Delta H_{i,j} - (C_4)_{i,j}\delta U_{i+1,j} - (C_5)_{i,j}\delta U_{i-1,j} \\ \vdots \\ \Delta U_{i,2} + \Delta H_{i,2} - (C_4)_{i,2}\delta U_{i+1,2} - (C_5)_{i,2}\delta U_{i-1,2} \\ 0 \end{bmatrix} \quad (2\text{-}38)$$

where

$$E = \begin{bmatrix} 1 & 0 & 0 & 0 \\ 0 & 1 & 0 & 0 \\ 0 & 0 & -1 & 0 \\ 0 & 0 & 0 & 1 \end{bmatrix}$$

The last equation in Equation (2-38) is used to set the boundary conditions which will be discussed in the later section.

With the above numerical schemes the Upwind, Hybrid Explicit-Implicit equations have the following form:

The predictor step

$$\Delta U_{i,j}^n = -\Delta t \left[\frac{D_+ F_i}{\Delta z} + \frac{D_+ (G_i - G_v)}{\Delta r} - H \right]_{i,j}^n$$

$$I + \Delta t\left(\frac{D_+ . A_-}{\Delta z} + \frac{D_- . A_+}{\Delta z}\right) + \Delta t\left(\frac{D_+ . B_-}{\Delta r} + \frac{D_- . B_+}{\Delta r}\right) - \frac{\Delta t}{\delta r}(\delta G_v)\Big]_{i,j}^n \delta U_{i,j}^{n+1} = \Delta U_{i,j}^n + \Delta H_{i,j}^n$$

$$U_{i,j}^{n+1} = U_{i,j}^n + \delta U_{i,j}^{n+1} \quad (2\text{-}39)$$

The corrector step

$$\Delta U_{i,j}^{n+1} = -\Delta t\left[\frac{D_{-}F_i}{\Delta z} + \frac{D_{-}(G_i - G_v)}{\Delta r} - H\right]_{i,j}^{n+1}$$

$$I + \Delta t\left(\frac{D_{+}.A_{-}}{\Delta z} + \frac{D_{-}.A_{+}}{\Delta z}\right) + \Delta t\left(\frac{D_{+}.B_{-}}{\Delta r} + \frac{D_{-}.B_{+}}{\Delta r}\right) - \frac{\Delta t}{\delta r}(\delta G_v)\Big]_{i,j}^{n} \delta U_{i,j}^{n+1} = \Delta U_{i,j}^{n+1} + \Delta H_{i,j}^{n}$$

$$U_{i,j}^{n+1} = \frac{1}{2}(U_{i,j}^{n} + U_{i,j}^{n+1} + \delta U_{i,j}^{n+1}) \qquad (2\text{-}40)$$

where $\delta U_{i,j}^{n+1}$ is calculated from Equation (2-38).

2.3 Turbulence Model

Turbulence modeling is the most important factor influencing the convergence of the Navier-Stokes equation solver, which is classified according to the number of supplementary partial differential equations. This number ranges from zero (algebraic model) to two (κ-ε model). The turbulent shear stresses in the mean-momentum equations are replaced by product of an effective viscosity and a mean rate of strain. The zero-equation model uses algebraic formulae to find the turbulent viscosity, which involve only properties of the mean velocity profile as unknowns. This is implied that the mean motion is unaffected by turbulence intensity and the length scale, which can be specified by an algebraic equation. One- and two-equation models obtain the velocity scale from a solution of the modeled form of turbulent kinetic energy equation and the specified length scale equation. In this study, the algebraic model has been used to yield faster convergence at reasonable accuracy.

The algebraic turbulence model used in this analysis is a two-layer algebraic eddy viscosity model proposed by Baldwin and Lomax.[5] The effects of turbulence are

simulated in terms of the eddy viscosity coefficient, μ_t, which is calculated for an inner and an outer region.

$$\mu = \begin{cases} \mu_{inner} \, z \le z_b \\ \mu_{outer} \, z > z_b \end{cases}$$

where z is the normal distance from wall, and z_b is the smallest value of z at which values from the inner and outer formulas are equal.

For the inner region, the Prandtl-Van Driest formulation for turbulent viscosity is used:

$$(\mu_t)_{inner} = \rho k^2 y^2 [1 - e^{(\frac{y^+}{A^+})}]^2 |\omega| \qquad (2\text{-}41)$$

where ω is the vorticity which is given by

$$|\omega| = \sqrt{\left(\frac{\partial u}{\partial z} - \frac{\partial v}{\partial r}\right)^2}$$

and

$$y^+ = \frac{\sqrt{\rho_w \tau_w} y}{\mu_w}$$

$$A^+ = 26$$

where τ_w, ρ_w and μ_w are the local shear stress, density, and laminar viscosity evaluated at the wall.

For the outer region, the Clauser formulation for turbulent viscosity is used:

$$(\mu_t)_{outer} = kC_{cp} \rho \; F_{wake} F_{kleb}(y) \qquad (2\text{-}42)$$

where κ is the Clauser constant, C_{cp} is an additional constant, and

$$F_{wake} = \min\left\{ \begin{matrix} y_{MAX} F_{MAX} \\ C_{WK} y_{MAX} u_{DIF}^2 / F_{MAX} \end{matrix} \right\} \tag{2-43}$$

The quantities y_{MAX} and F_{MAX} are determined from the function

$$F(y) = y|\omega|[1 - e^{(\frac{y^+}{A^+})}] \tag{2-44}$$

In wakes, the exponential term of Equation (2-44) is set equal to zero. The quantity F_{MAX} is the maximum value of F(y) that occurs in a profile and y_{MAX} is the value of y at which it occurs. The F_{kleb} (y) is the Klebanoff intermittency factor given by

$$F_{kleb}(y) = \left[1 + 5.5\left(\frac{C_{kleb} y}{y_{max}} \right)^6 \right]^{-1} \tag{2-45}$$

The quantity u_{DIF} is the difference between maximum and minimum total velocity in the profile

$$u_{DIF} = \left(\sqrt{u^2 + v^2} \right)_{max} - \left(\sqrt{u^2 + v^2} \right)_{min} \tag{2-46}$$

The constants used for this model have been determined by requiring agreement with the Cebeci formulation for a constant pressure boundary layer. The values determined are C_{cp}=1.6, C_{wk}=0.25, C_{kleb}=0.3, κ=0.4 and K=0.0168.

In effect the voticity ω is used to determine the length scale, so that the necessity for finding the outer edge of boundary layer is removed. This model has the advantage of avoiding the necessity for finding the edge of the boundary layer and exhibits good accuracy.

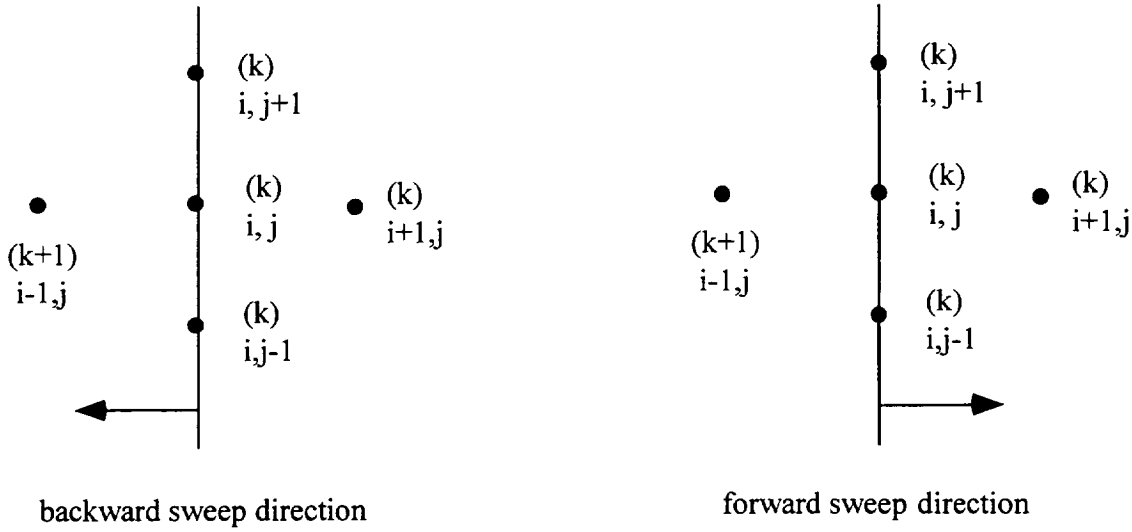

Figure 2-1 Sweep direction for line Gauss-Seider iteration (From Reference [27]).

2.4 Diffusion Model for Thermal Radiation

Under high temperature conditions of gaseous core reactor the radiative heat transfer rate in these opaque gases is comparable with the convective heat transfer rate. Therefore, the heat transfer analysis of a fissioning gas must include both convective and radiative heat transfer. The flow and radiation transport equation must be solved simultaneously to determine the temperature distribution and heat transfer rate. For such numerical model, radiative and convective heat fluxes are combined in the energy equation. Although there are several ways to obtain the radiative heat flux, for example, the Monte Carlo method, the zoning method, and the p-n approximation, the Rosseland diffusion approximation is widely used because it is simple to formulate and calculate. In order to use the Rosseland diffusion approximation the following assumptions are required:

(1) The flow is an opaque and gray dense medium with only absorption and emission.

(2) The radiation arriving at any location comes only from the immediate surroundings because any other radiation is absorbed before arriving at that location.

(3) The particles are locally in thermal equilibrium and near velocity equilibrium.

(4) The axial radiative dissipation is neglected.

Under above assumption the radiative heat flux is proportional to the temperature gradient and can be written as:[47]

$$q_r = -K_r \nabla T \tag{2-47}$$

where K_r is the radiative conductivity and is defined by[40]

$$K_r = \frac{16\sigma T_w^3}{3a_R} \tag{2-48}$$

where a_R is the Rosseland mean opacity and σ is the Stefan-Boltzmann constant ($5.67*10^{-8}$ $W/m^2.K^4$). To obtain the Rosseland mean opacity a_R, the spectral absorption coefficient is averaged over the entire frequency range as the following:[11]

$$a_R = \frac{\int_0^\infty \frac{\partial B_v}{\partial T} dv}{\int_0^\infty \frac{n^2}{a_v} \frac{\partial B_v}{\partial T} dv} \tag{2-49}$$

where ν is the photon wave number, B_v is the Planck function, a_v is the spectral absorption coefficient, and n is the real index of refraction. Direct calculation of the Rosseland mean opacity for UF_4 is difficult due to the lack of experimental data for the spectral absorption coefficient of UF_4. However for this study, the Rosseland mean opacity can be estimated by[12]

$$a_R = N\sigma_{ph} \tag{2-50}$$

where N is the molecular number density of the gas and σ_{ph} is the photon collision cross section per molecule. For UF_4 gas σ_{ph} is estimated to be equal to $2.76x10^{-22}$ m^2. [10] Using the assumption of the perfect gas law the molecular number density can be estimated as

$$N = \frac{p}{\kappa T} \tag{2-51}$$

where κ is the Boltzmann constant ($1.3806*10^{-23}$J/K), p is the gas pressure, and T is the gas temperature. Therefore, the radiative conductivity can be written as

$$K_r = \frac{16\sigma\kappa}{3\sigma_{ph}p} T^4 \tag{2-52}$$

Using the estimated opacities the Rosseland approximation leads to a considerable simplification in the expression for radiative heat flux. The radiative heat flux is added to the Equations (2-3) and (2-4) to establish the balance of the energy equations. Since

radiation leaving from the surface is not taken into account, the coefficient of radiation conductivity in Equation (2-52) has to be changed from 16/3 to 8/3.[47]

2.5 Wall Heat Transfer Model

The system is limited to smooth, straight tubes within which the fluid flow is turbulent. In the system, two boundary conditions, constant wall temperature and constant wall heat flux on the outside surface of the tube, are of particular interest and considered here. There are two ways to describe the convective heat transfer into the wall boundary. One way is to use Newton's cooling law. That is

$$q'' = h(T_w - T_b) \tag{2-53}$$

where h is the convective heat transfer coefficient or so-called unit thermal conductance, which is not a material property as thermal conductivity. It is a complex function of the composition of the fluid, the geometry of solid wall and the hydrodynamics of the fluid motion, in particular, the temperature distribution near the solid wall. So it is impossible to estimate the heat transfer coefficient without solving the Navier-Stokes equations.

The other way is to apply Fourier's law. That is

$$q'' = -k_w\left(\frac{dT}{dr}\right)_{gas} \tag{2-54}$$

where k_w is the thermal conductivity which is evaluated at the wall temperature. The temperature gradient in equation (2-54) is calculated using the wall temperature and adjacent cell temperature. It may be numerically written as

$$q'' = -k_w \frac{T_2 - T_w}{r_2 - r_1} \tag{2-55}$$

The condition of the above equation is that the temperature distribution near the wall has to be linear. This means that equation (2-55) can only be applied in the viscous sublayer.

The turbulent boundary layer is composed of three different sublayers, such as viscous sublayer, buffer layer and turbulent core, which is presented in Figure 2-2. In the viscous sublayer, heat transfer is dominated by diffusion. The temperature distribution is linear, as shown in Figure 2-3. In order to use equation (2-55), it is important to determine the thickness of the viscous sublayer which may be estimated by the following relation:[35]

$$\delta_b = \frac{72.94z}{(\mathrm{Re}_z)^{0.9}} \tag{2-56}$$

The magnitude of δ_b is about 2-5 μm. This means that at least 3 cells have to locate in the 2-5 μm region near the solid-fluid interface. A simple sketch of finite volume mesh to express the boundary index system is shown in Figure 2-4.

2.6 Boundary Conditions

Following the above wall heat transfer model, three kinds of thermal boundary condition are applied in this study, which are adiabatic boundary condition, a constant wall temperature condition and constant heat flux condition.

The adiabatic boundary condition

The general form and numerical expression are

$$q'' = 0$$
$$T_1 = T_2 = T_w \tag{2-57}$$

The physical meaning of this boundary condition is that no heat transfer passes through the boundary.

The constant wall temperature condition

The general form and numerical expression are

$$T_w = f(z) \tag{2-58}$$
$$T_1 = 2T_w - T_2 \tag{2-59}$$

The physical meaning of this boundary is that temperature is on the isothermal condition. This boundary condition can be specified for the solid-fluid interface, which is indicated in Figure 2-5.

The constant heat flux condition

The general form and numerical expression are

$$q'' = const \tag{2-60}$$

$$T_1 = T_2 + \frac{q_r'}{k}(r_2 - r_1) \tag{2-61}$$

Because both T_1 and T_2 are unknown before each iteration, it is difficult to specify the boundary condition which is indicated in Figure 2-6. An enthalpy-rebalancing scheme is developed to apply this boundary condition. It is performed in the next section.

2.7 Enthalpy-Rebalancing Scheme

For the problem with constant heat flux condition, which is shown in Figure 2-4, it is difficult to obtain convergent solutions. The reason is that integrating solution is impossibly found just from its first derivative. In order to solve problems under an arbitrary heat flux boundary condition, a novel method of enthalpy-rebalancing at the transverse flow surface has been developed. This scheme is based on the fact that under steady conditions the gas enthalpy rise at each transverse flow surface is equal to the heat removal from the wall. Mathematically, it can be written as follows:

$$(\Delta Q)_i = 2\pi R \Delta z q_i'' \tag{2-62}$$

Equation (2-62) is explicitly solved to obtain the balancing bulk temperature $(T_b)_i$, that is

$$(T_b)_{i+1} = (T_b)_i + \frac{2\Delta z q_i''}{Cp_i (\rho u)_i R} \tag{2-63}$$

where T_b is the bulk temperature, and Cp_i is the local specific heat. In this section, $(T_b)_i$ is known. $(T_b)_{i+1}$ can be found from Equation (2-63) which is always true in the transient procedure based on the enthalpy-balancing principle. The bulk temperature $((T_b)_{i+1})_{num}$ is calculated from temperature fields under every iteration. Since these two bulk temperatures should be equal, their relation may be used as a convergence criterion as follows:

$$\delta = \frac{(T_b)_{i+1}}{((T_b)_{i+1})_{num}} \tag{2-64}$$

Before achieving the steady-state flow conditions, the mass flux ρu, is always smaller than the final steady value. Therefore, during the transitory pre-steady state conditions the value of δ is greater than one. Whenever the mass flux approaches its steady-state value, the convergence parameter δ approaches its asymptotic value which is one. At this moment, the wall boundary condition (2-61) is used to calculate the wall temperature. As soon as δ is equal to one, a thermal steady-state condition is achieved. At this point, the wall temperature is fixed to control the heat transfer through the solid wall until a global thermal convergence is achieved. This scheme has been proven successful when problems with heat flux boundary condition are to be solved.

2.8 Conduction Model

The temperature distribution in the fuel elements is the essential to the prediction of the lifetime behavior of these components. The temperature distribution in the fuel dependents on the volumetric heat generation rate, fuel material properties, dimension of the fuel element and geometric configuration. Of these the first 3 parameters are related the neutronic design considerations, so geometric configuration is the only optional factor via a thermal analysis. There are four types of geometric configuration, plate, pin, tubular and square lattice honeycomb, which are commonly used in reactor fuel element design. The configurations can be found in Figure 2-7. In order to evaluate the geometric configuration and predict the temperature distribution, a dimensionless number is defined as the following:

$$\delta(\alpha) = \frac{k\Delta T}{q''' D_h(\alpha)^2} \tag{2-65}$$

where q''' is the volumetric heat generation rate, D_h is the hydraulic diameter, k is conductivity of the fuel materiel and ΔT is the difference between maximum temperature and wall temperature and α is void parameter which is defined as

$$\alpha = \frac{A_{Flow}}{A_{Total}} \tag{2-66}$$

The physical concept behind this definition is the efficiency of the conductive heat transfer. The focus of the Delta number is on the geometric behavior of the fuel element which is strongly dependent on the temperature distribution. The thermal conduction equation describes the temperature distribution in the fuel element. Under the assumption of negligible thermal expansion, the general equation of heat conduction becomes:[31]

$$\nabla^2 T(x,y) + \frac{q'''}{k} = 0 \tag{2-67}$$

where T is temperature distribution function (K)

q''' is the volumetric heat generation (w/cc)

k is thermal conductivity (J/cm/K)

2.8.1 Plate and Pin Configurations

Because of the symmetric geometry, at steady state the general conduction equation for geometries of plate and pin reduce to a ordinary differential equation which can be written as:

For plate,

$$\frac{dT(x)^2}{d^2x} + \frac{q_r''}{k} = 0$$
$$T\left(x = \frac{l}{2}\right) = T_w \tag{2-68}$$

For pin

$$\frac{1}{r}\frac{d}{dr}\left(r\frac{dT(r)}{dr}\right) + \frac{q_r''}{k} = 0$$
$$T\left(r = \frac{D}{2}\right) = T_w \tag{2-69}$$

Equations 2-68 and 2-69 can be integrated, respectively:

$$T(x) = T_w + \frac{q'''}{8k}\left(l^2 - 4x^2\right). \tag{2-70}$$

$$T(r) = T_w + \frac{q'''}{16k}\left(D^2 - 4r^2\right). \tag{2-71}$$

Therefore,

$$\delta_{Plate} = \frac{(1-\alpha)^2}{32\alpha^2} \tag{2-72}$$

$$\delta_{Pin} = \frac{(1-\alpha)^2}{16\alpha^2} \tag{2-73}$$

2.8.2 Tubular and Square Lattice Honeycomb Configurations

For complex geometry, such as tubular and square lattice honeycomb, partial differential equation (2-55) can not be solved analytically. The computer code ANSYS is used to get the numerical results.

The general purpose Finite Element code ANSYS developed by Del Salvo et al. uses a set of elements whose stiffness matrices have already been set up. These elements are referred to by a pair of numbers, each identifying the type of analysis and the degrees of freedom per node. ANSYS uses the following relationships for heat transfer analysis:

$$\nabla^2 T(x,y) + \frac{q'''}{k} = 0 \tag{2-74}$$

These equations are solved by the Finite Element (FE) technique. To start with, a temperature distribution is obtained based on an input reference temperature and then properties such as thermal conductivity, are evaluated at nodal temperatures. This procedure is continued until a convergence in nodal temperature is achieved. Physical properties of the structural material at each node are then evaluated based on this calculated nodal temperature. These nodal temperatures are stored in a file for later use.

The input parameters and sample input file are listed below:

Table 2-1 Input parameters for ANSYS analysis.

Parameter	Symbol	Value and Unit
Volumetric heat-generation rate	q'''	9 (W/mm^2)
Surrounding temperature	T_s	2500 (K)
Heat-transfer coefficient	h	0.0655 ($w/mm^2.K$)
Thermal conductivity	k	0.036 (W/mm.K)
Specific heat, constant pressure	C_p	4.44 (J/kg.K)

The sample data for ANSYS analysis:

```
/title, tubular
kan, -1
treff,2500
et,1,55
iter,-1
ktemp,-1
k,1,0.0
k,2,0.278
k,3,0.62
k,4,0.791
k,5,0.791,0.53
k,6,0.371,0.6425
k,7,0.1855,0.3213
k,8,0.11,0.19
L,1,2
L,2,3
L,3,4
L,4,5
larc,5,6,4,-0.84
elsiz, ,50
L,6,7
L,7,8
L,8,1
a,1,4,5,6
amesh,all
wsort,x
wsort,y
lssel,line,1,4,1,1
hflow,all,heat,0.0
nall
lsall
lssel,line,5,,,1
eall
cvsf,all,z,,0.0655,2500
nall
lsall
lssel,line,6,8,1,1
hflow,all,heat,0.0
```

nall
eall
kxx,1,0.036
kyy,1,0.036
c,1,4.44
q,all,9
lwrite
afwrite
FINI

The Figures 2-8 to 2-12 show the typical computation grids and temperature distribution for tubular and square lattice honeycomb, respectively. The numerical results are presented in the following tables:

Table 2-2 Variation of Delta number in tubular fuel element.

α	D_h	$\Delta T(K)$	δ
0.1	1.021	162	0.7826
0.2	1.286	111	0.2681
0.3	1.576	72	0.1161
0.4	1.822	49	0.0592
0.5	2.034	33	0.0319
0.6	2.228	24	0.0193
0.7	2.407	17	0.0117
0.8	2.573	14	0.0085

Table 2- 3 Variation of Delta number in SLHC fuel element.

α	D_h	$\Delta T(K)$	δ
0.1	0.947	298	1.3297
0.2	1.341	188	0.4178
0.3	1.643	128	0.1896
0.4	1.897	88	0.0977
0.5	2.121	59	0.0525
0.6	2.324	38	0.0282
0.7	2.512	22	0.0141
0.8	2.683	9	0.0052

After polynomial fitting, the relations between Delta number and void parameter are given as follows:

Table 2-4 Polynomial formula of the Delta number.

Configuration	Delta Number
Plate	$\frac{(1-\alpha)^2}{32\alpha^2}$
Pin	$\frac{(1-\alpha)^2}{16\alpha^2}$
Tubular	$2.1-18.9\alpha+73.6\alpha^2-142.1\alpha^3+135.7\alpha^4-50.6\alpha^5$
SLHC	$3.8-36.5\alpha+147.2\alpha^2-294.4\alpha^3+286.7\alpha^4-109.4\alpha^5$

The above relations are presented in Figure 2-13.

2.8.3 Applications of Delta Number

The delta number is similar to other dimensionless numbers in heat transfer, such as Mach number and Reynolds number. It expresses the relationship between several thermal parameters which are heat-generation rate, thermal conductivity, surrounding temperature, maximum temperature and the geometric parameter. There are at lest two important applications related to design of the nuclear fuel element: (1) to evaluate the coolant channel configuration and (2) to predict the maximum temperature.

Delta number is function of the void parameter for several different coolant channel configurations. From conduction of view, the optimum configuration can be determined based on Figure 2-8. The smaller Delta number means the lower maximum temperature in the fuel element. So the Delta number can be used to control temperature gradients, which is important for the lifetime of reactor components.

Once the fuel surface temperature and volumetric heat generation rate have been determined, the centerline temperature, maximum temperature of fuel element, can be calculated from equation (2-65). This method to calculate centerline temperature, instead of the time-consuming CFD and other iterative procedures, will remarkably simplify the centerline temperature calculation. This method has been used by Reference [15] and proved to be accurate and efficient.

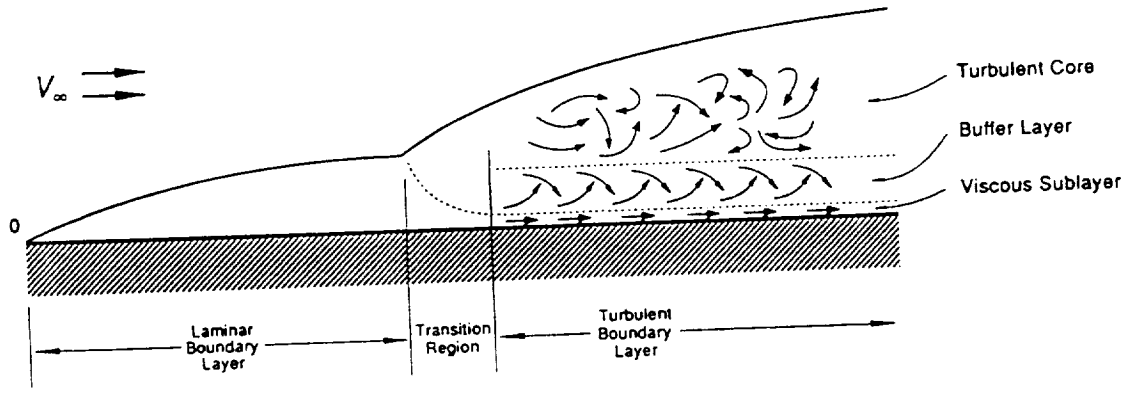

Figure 2-2 Boundary layer of turbulent flow (From Reference [42]).

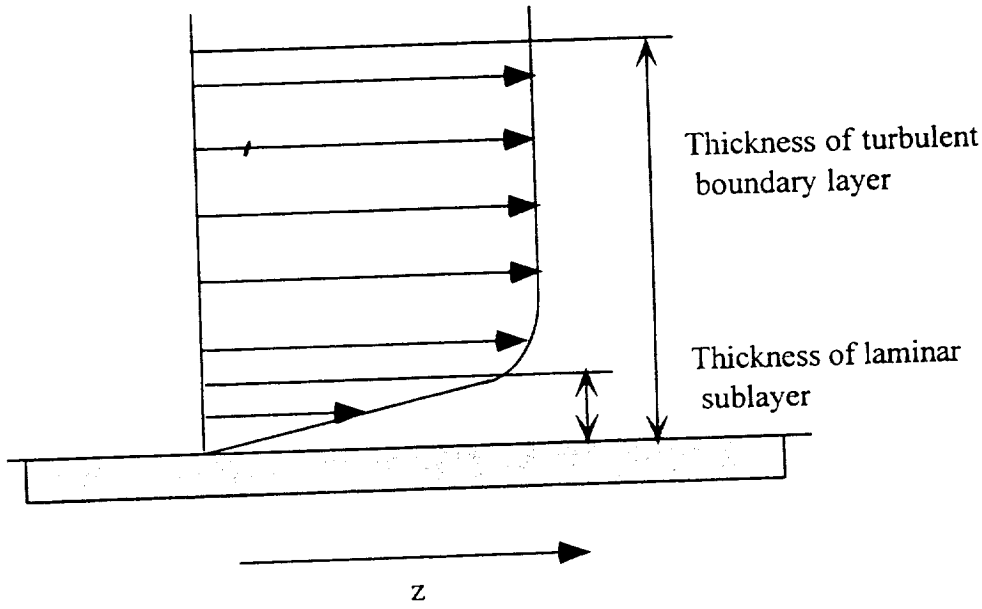

Figure 2-3 Turbulent boundary layer and laminar sublayer.

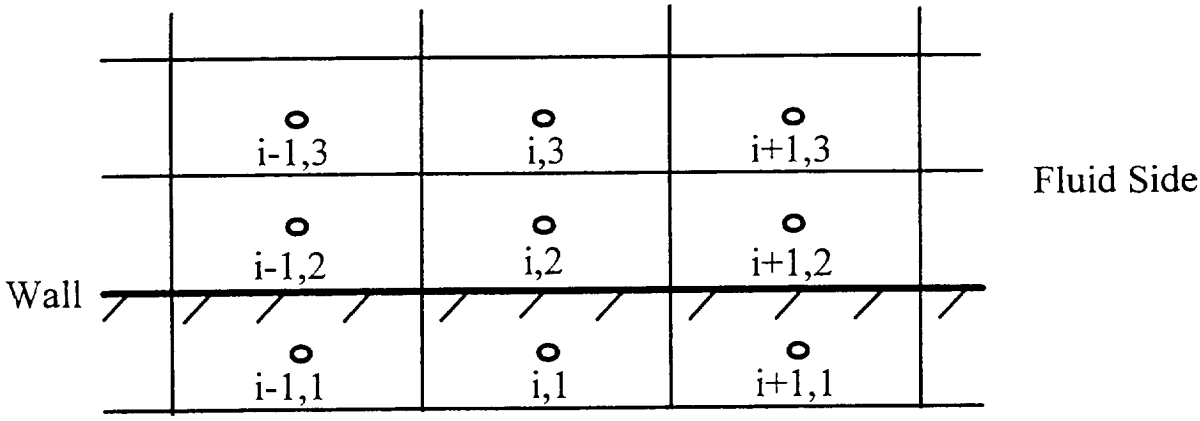

Fig. 2-4 Finite volume grid system.

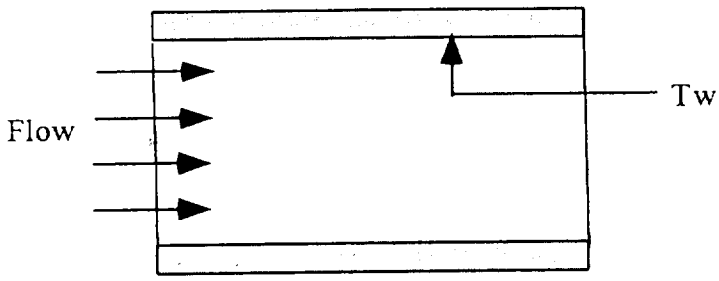

Figure 2-5 The isothermal wall boundary condition.

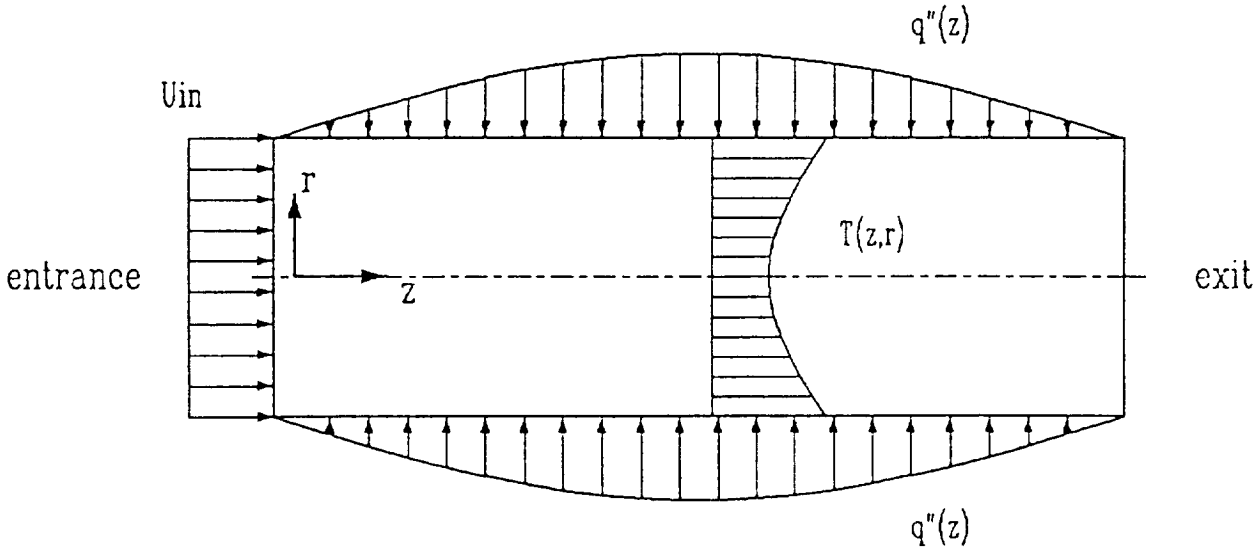

Figure 2-6 The heat flux boundary condition.

(1) Plate

(2) Pin

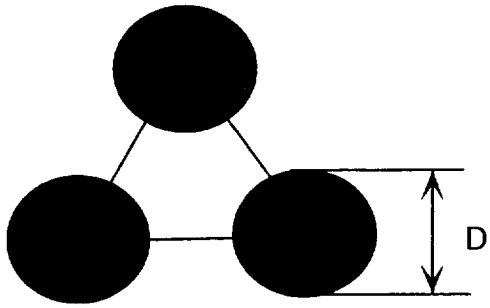

(3) Tubular

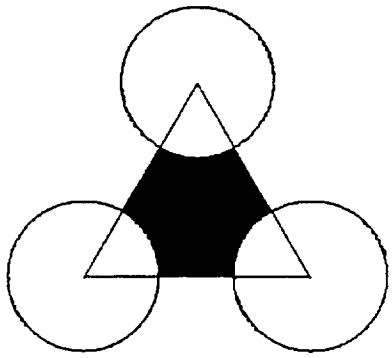

(4) Square Lattice
Honeycomb

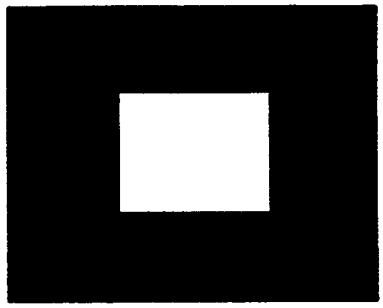

Figure 2-7 Configuration of reactor fuel elements.

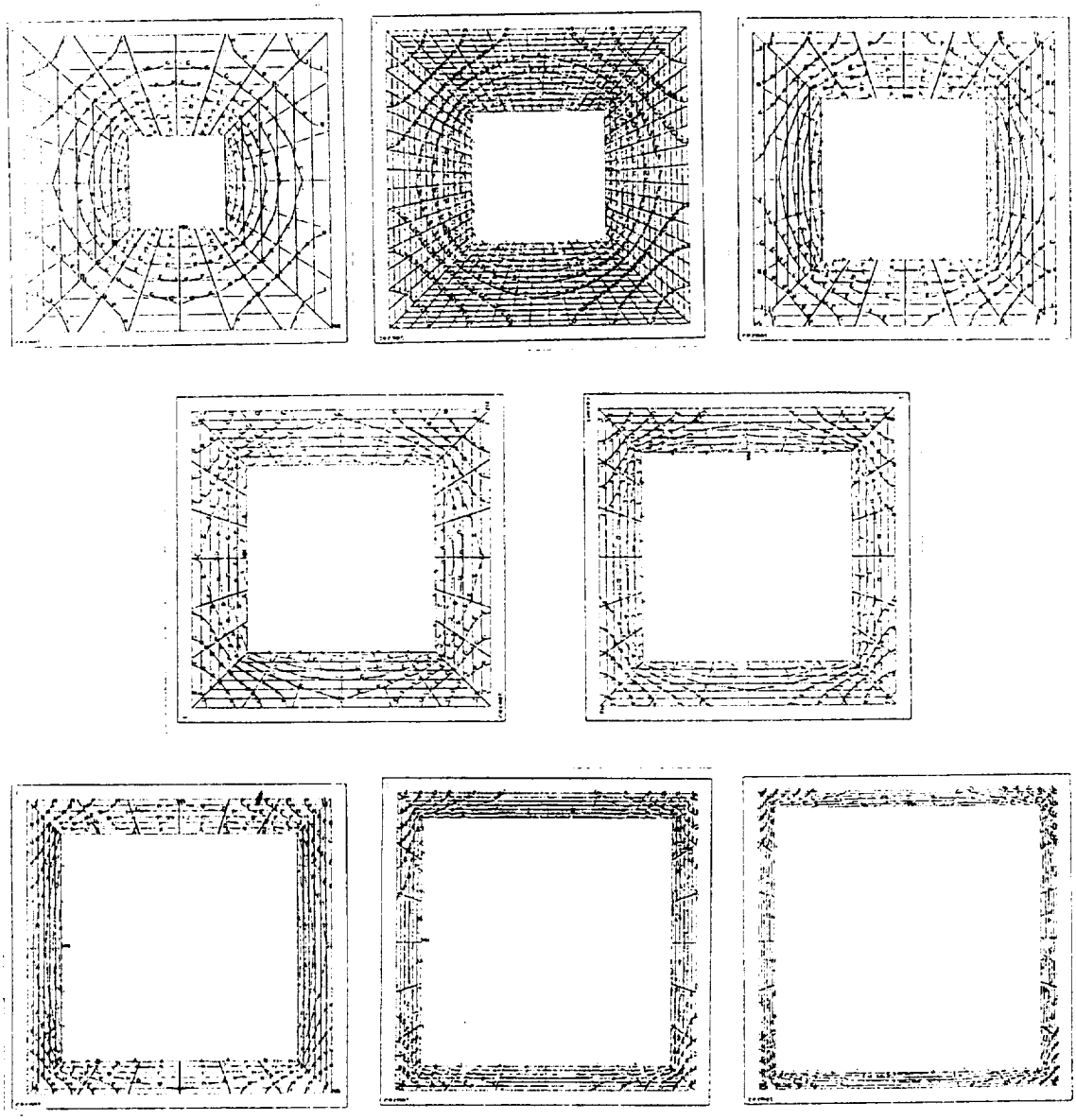

Figure 2-8 Temperature distribution in square lattice honeycomb fuel element (α is ranged from 0.1 to 0.8).

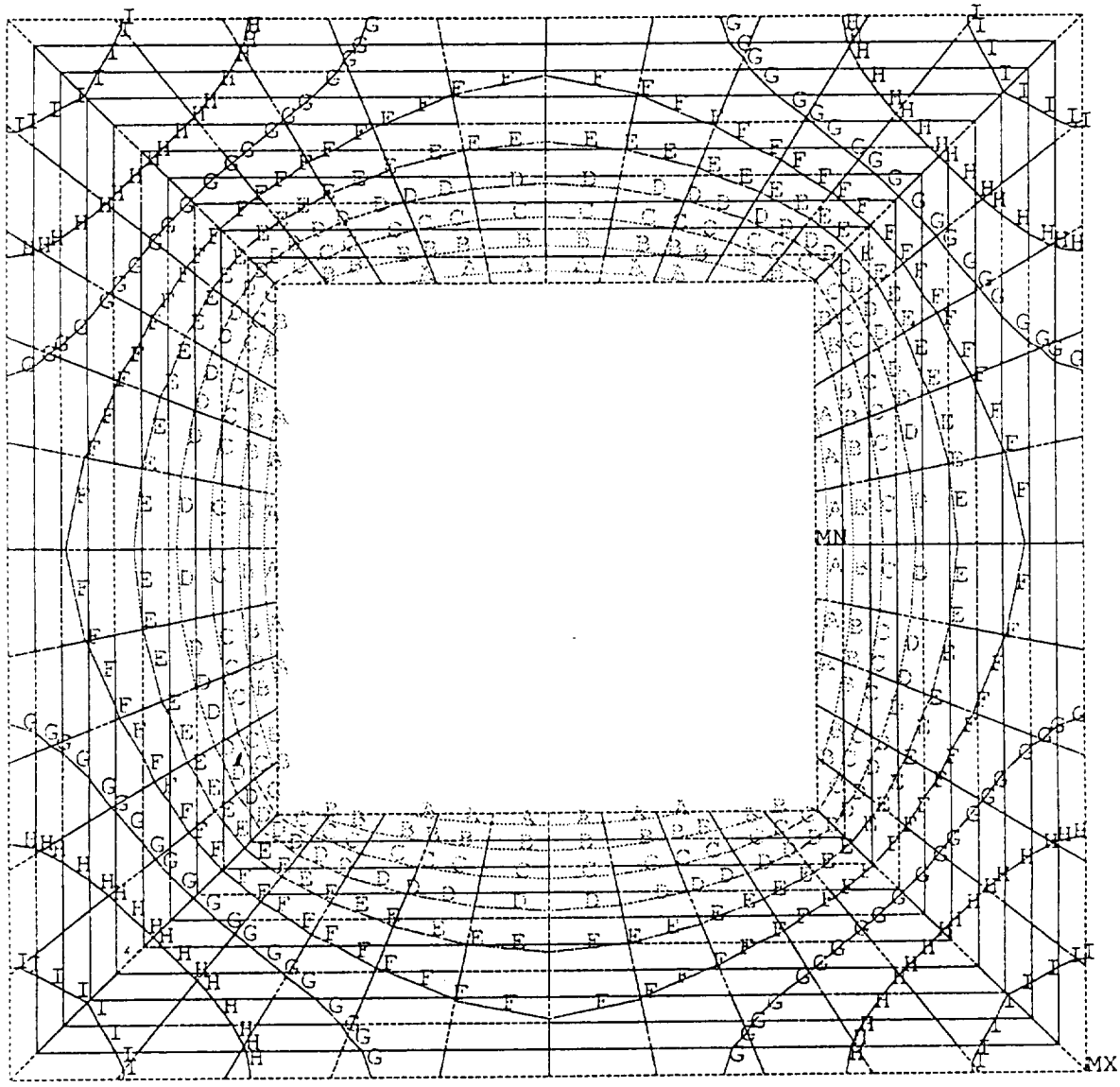

Figure 2-9 Temperature distribution in square lattice honeycomb fuel element (α=0.25).

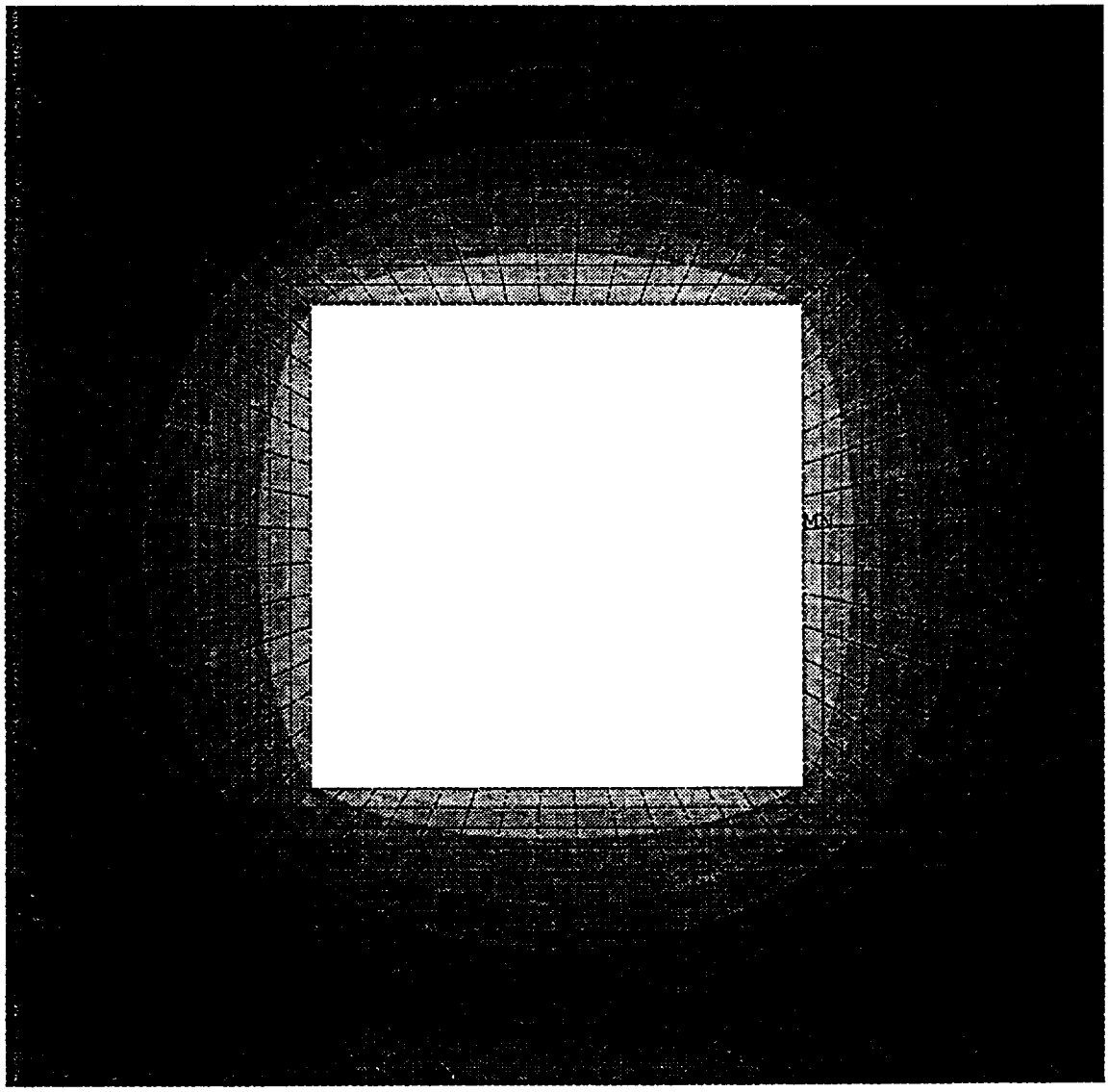

Figure 2-10 Temperature distribution in square lattice honeycomb fuel element (α=0.2).

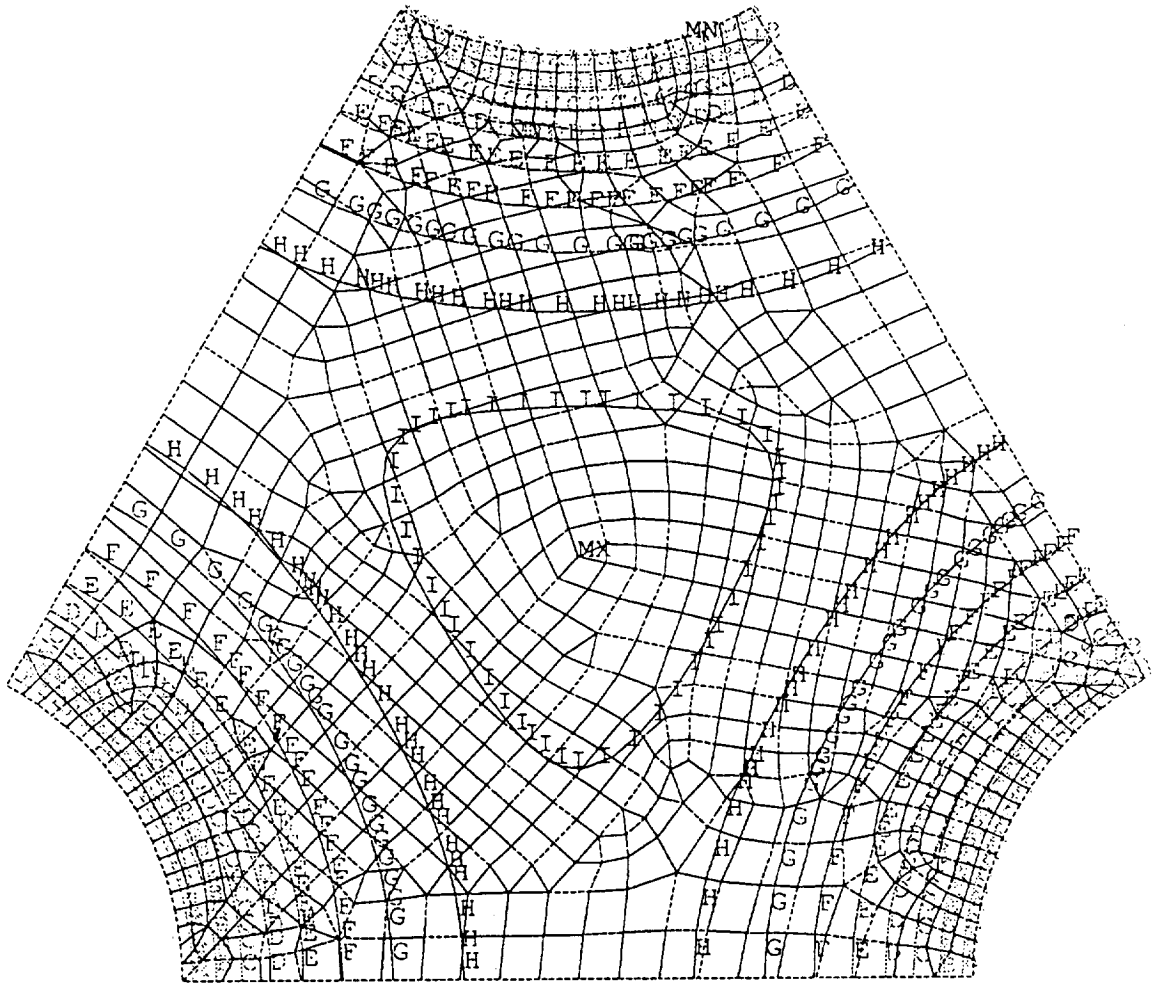

Figure 2-11 Temperature distribution in tubular fuel element (α=0.2).

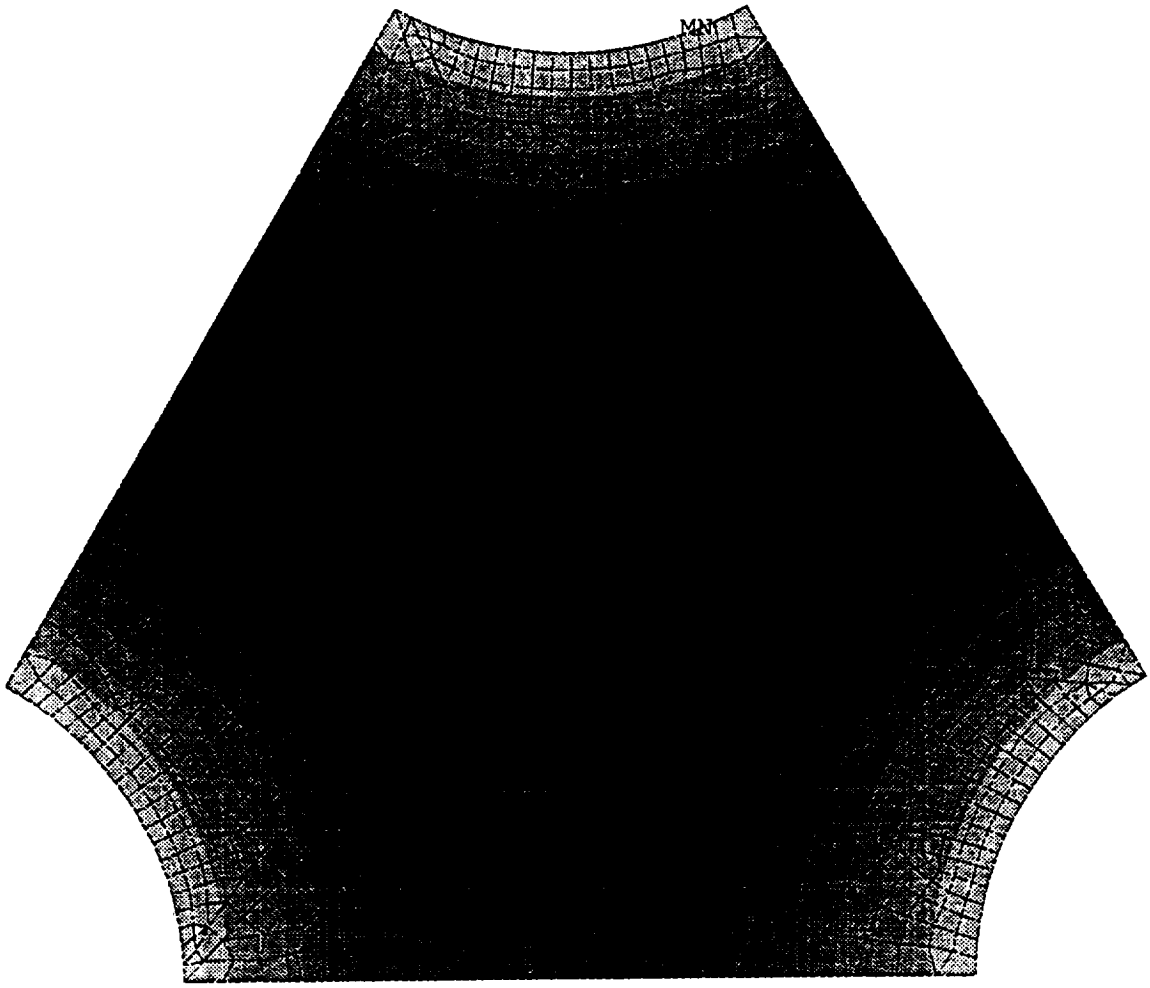

Figure 2-12 Temperature distribution in tubular fuel element (α=0.2).

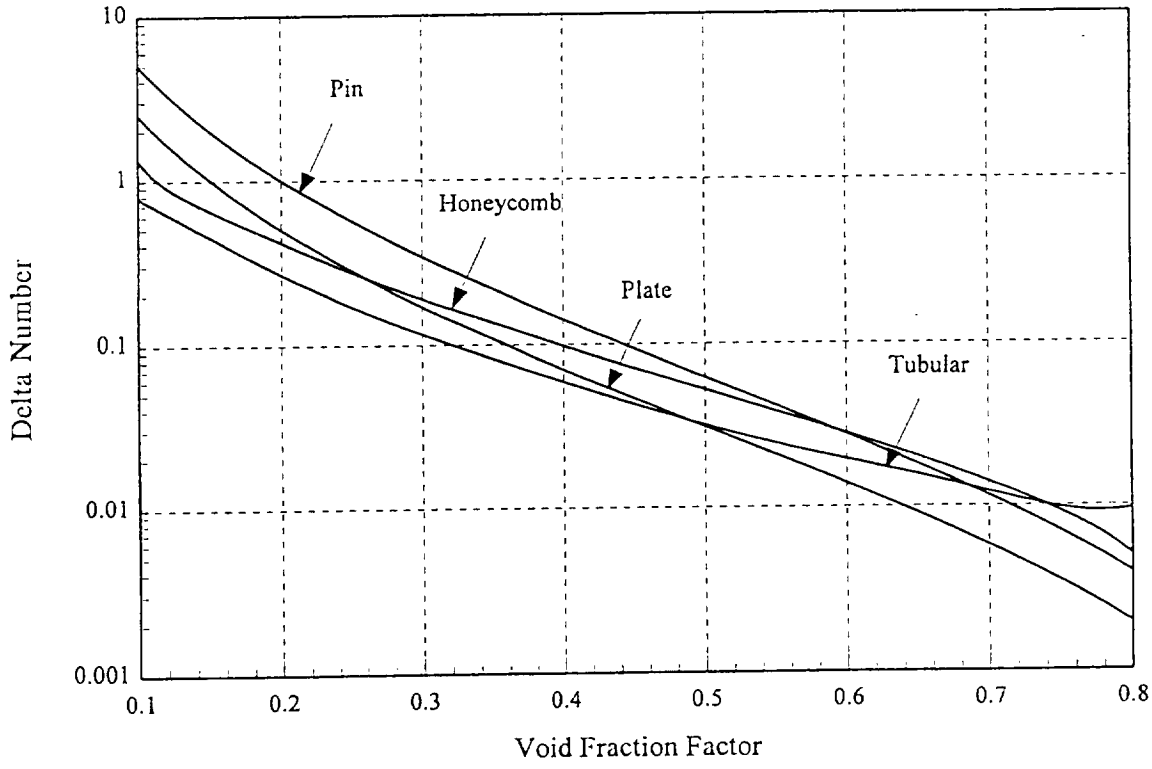

Figure 2-13 Delta number vs. void fraction factor.

CHAPTER 3
THERMOPHYSICAL PROPERTIES

Thermophysical properties are very important parameters in CFD calculation. In order to get accurate results, the real thermophysical properties of hydrogen, helium and UF_4 gases are used in this study.

3.1 Dissociated Hydrogen

The data of the hydrogen property package comes from three different sources which provide information in different temperature regions. From temperatures ranging from 13.8° to 3000 °K, data is based on the National Bureau of Standards. Above 3000°K and up to 10,000°, the data is obtained from NASA computer programs. Above 10,000°K, the data is generated by extrapolation of the data base. For the hydrogen properties, the data provided by the hydrogen package is the best available at this time.

In order to get the hydrogen properties for given condition, a numerical code based on cubic spline interpolation was developed. This code interpolates with respect to temperatures or enthalpies and pressures to find all other thermodynamic properties, such as density, viscosity, thermal conductivity, entropy, specific heat, speed of sound and ratio of specific heats.

The concept of the cubic spline interpolation is to construct a cubic function $S_k(x)$ on each interval $[x_k, x_{k+1}]$ so that the resulting curve $y = S(x)$ and its first and second derivatives are all continuous on the large interval $[x_0, x_N]$. The function S(x) is called a cubic spline which has to satisfy the following equations:[36]

$$\text{I. } S(x) = A_k + B_k(x - x_k) + C_k(x - x_k)^2 + D_k(x - x_k)^3 \tag{3-1}$$

$$\text{II. } S(x) = y_k \tag{3-2}$$

$$\text{III. } S_k(x_{k+1}) = S_{k+1}(x_{k+1}) \tag{3-3}$$

$$\text{IV. } S'_k(x_{k+1}) = S'_{k+1}(x_{k+1}) \tag{3-4}$$

$$\text{V. } S''_k(x_{k+1}) = S''_{k+1}(x_{k+1}) \tag{3-5}$$

The above properties of cubic spline function are shown in Figure 3-1.

The general form of cubic spline equation $S_k(x)$ is the following expression:

$$S_k(x) = \frac{S''(x_k)(x_{k+1} - x)^3}{6(x_{k+1} - x_k)} - \frac{S''(x_{k+1})(x_k - x)^3}{6(x_{k+1} - x_k)} + \left(\frac{y_k}{x_{k+1} - x_k} - \frac{S''(x_k)(x_{k+1} - x_k)}{6}\right)(x_{k+1} - x) - \left(\frac{y_{k+1}}{x_{k+1} - x_k} - \frac{S''(x_{k+1})(x_{k+1} - x_k)}{6}\right)(x_k - x) \tag{3.6}$$

Now use the properties IV and V to obtain an important relation with respect to x_k, x_{k+1}, y_k and y_{k+1}:

$$\frac{S''(x_{k-1})(x_k - x_{k-1})}{6} + \frac{S''(x_k)(x_{k+1} - x_{k-1})}{3} + \frac{S''(x_{k+1})(x_{k+1} - x_k)}{6} = \frac{(y_{k+1} - y_k)}{x_{k+1} - x_k} + \frac{(y_k - y_{k-1})}{x_k - x_{k-1}} \tag{3.7}$$

This equation is a system of n-1 linear algebraic equations to be solved simultaneously. Its coefficient matrix is tridiagonal matrix. The linear system is diagonally dominant and has a unique solution. After the linear system is solved, the unknowns, $S''(x_{k-1})$, $S''(x_k)$ and $S''(x_{k+1})$, are determined. The interpolation value can be calculated from equation (3.7).

This code was used to draw 8 sets of curves that look very smooth when viewed by the eye. The curves are shown in Figures 3-2 to 3-9.

3.2 Helium Gas

The thermophysical properties, heat capacity C_p, viscosity μ and thermal conductivity K_c, based on the references [34] and [45] are used throughout the calculation. The formula of polynomial fitting are generated as follows:

$$C_p(kJ/kg.K) = -8.3799x10^{-8}T^2 + 3.51145x10^{-4}T + 0.87076 \quad (3\text{-}8)$$

$$\mu(N.s/m^2) = \frac{3.5761x10^{-7}T^3 - 8.4466x10^{-4}T^2 + 0.909139T + 1.59283}{1.0^7} \quad (3\text{-}9)$$

$$K_c(W/m.K) = \frac{0.257455T + 95.4545}{10^3} \quad (3\text{-}10)$$

3.3 Uranium Tetrafluoride Gas

Thermophysical properties of UF_4 gas used throughout the calculation are given by Equations (3-11)-(3-13).[3] In these equations, C_p is heat capacity, μ is dynamic viscosity and K_c is thermal conductivity.

Analysis of existing data and rigorous theoretical calculations are used to developed the following heat capacity equations for the gaseous UF_4 in 1000° to 10,000°K range.

$$C_p(J/mol.K) = 121.5 + 2.24\times10^{-3}T - \frac{3.06\times10^9}{T^3} \qquad [\,T < 3500°K\,] \quad (3\text{-}11)$$

$$C_p(J/mol.K) = 124.12 - 1.28\times10^{-3}T \qquad [\,T > 3500°K\,] \quad (3\text{-}12)$$

Using the semi-empirical relations for related transport parameters, the viscosity of UF_4 in 1000° to 10,000°K range is developed[30] as follows:

$$\mu(Pa.s) = \frac{3.357 \times 10^{-6} \sqrt{T}}{a + bT} \tag{3-13}$$

where $a = 0.8$ $b = -7.1 \times 10^{-5}$ [T < 3500°K]

$a = 0.67$ $b = -2.04 \times 10^{-5}$ [T > 3500°K]

Thermal conductivity of UF_4 gas is estimated as:

$$K_c(W / m.K) = 3.2\,\mu\left(C_p + 10.393\right) \tag{3-14}$$

where heat capacity C_p is in J/mol.K, and the viscosity μ is in Pa.s.

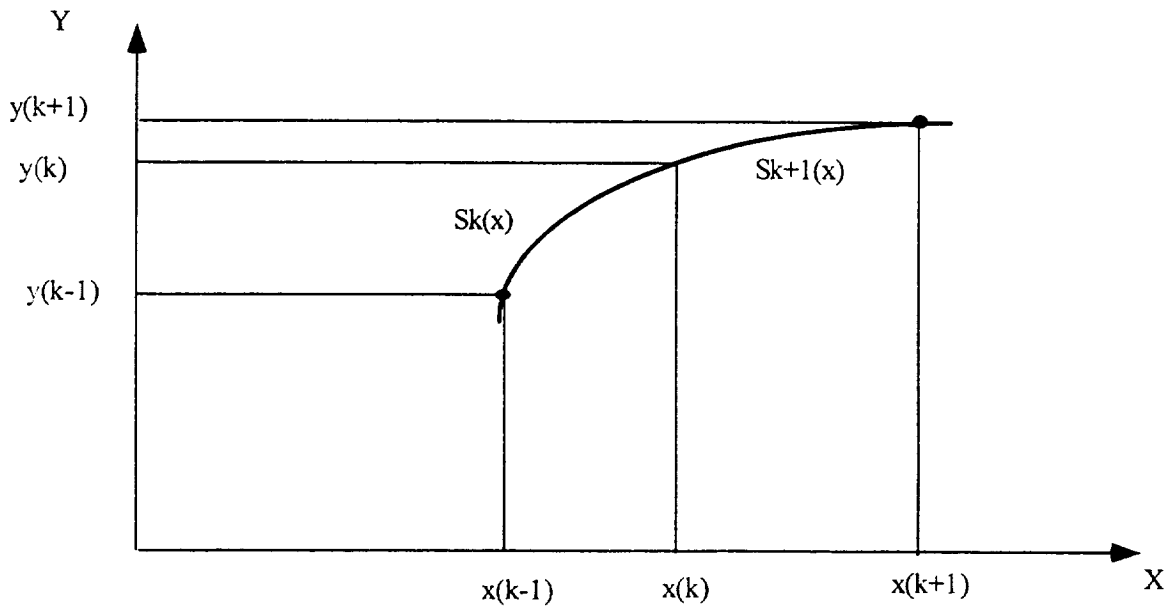

Figure 3-1 ‹ Cubic spline interpolation.

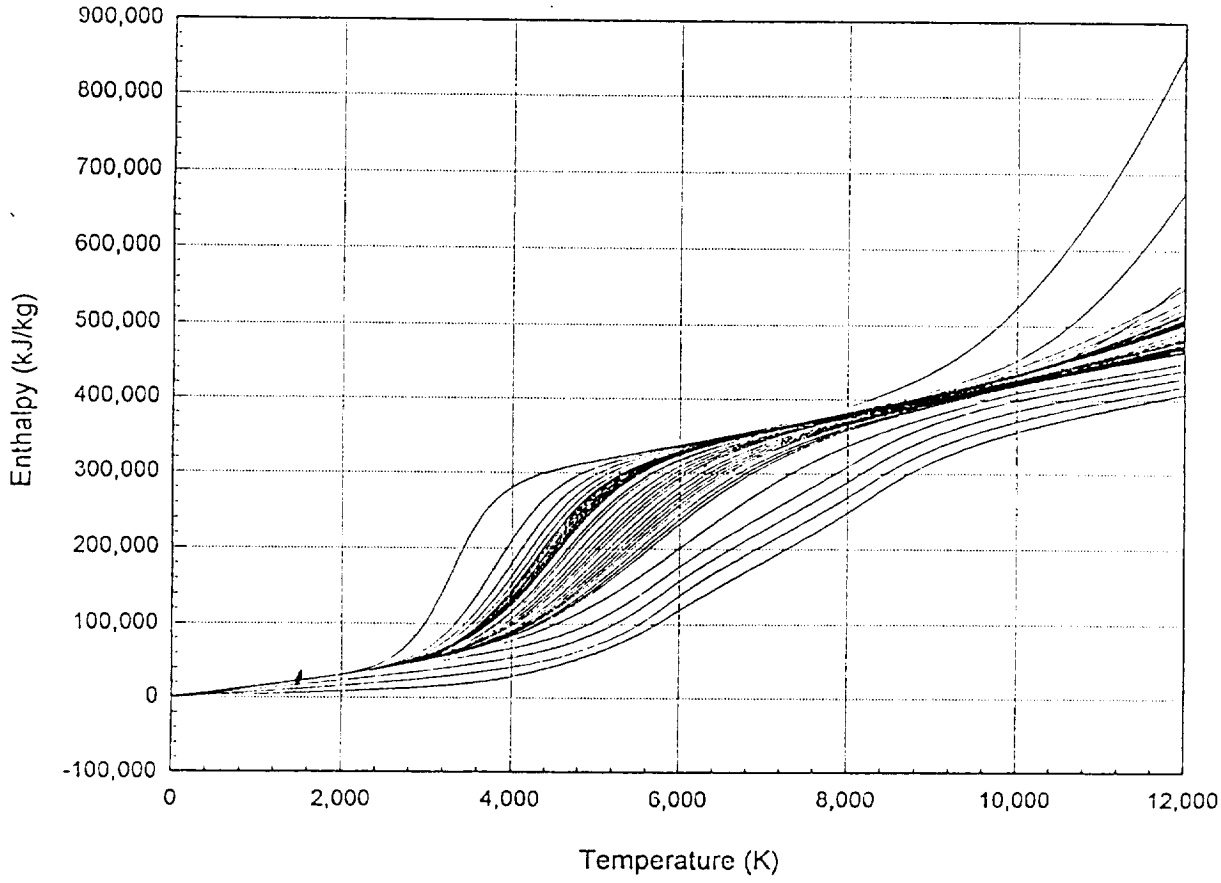

Figure 3-2 Enthalpy of dissociated hydrogen for different pressure.

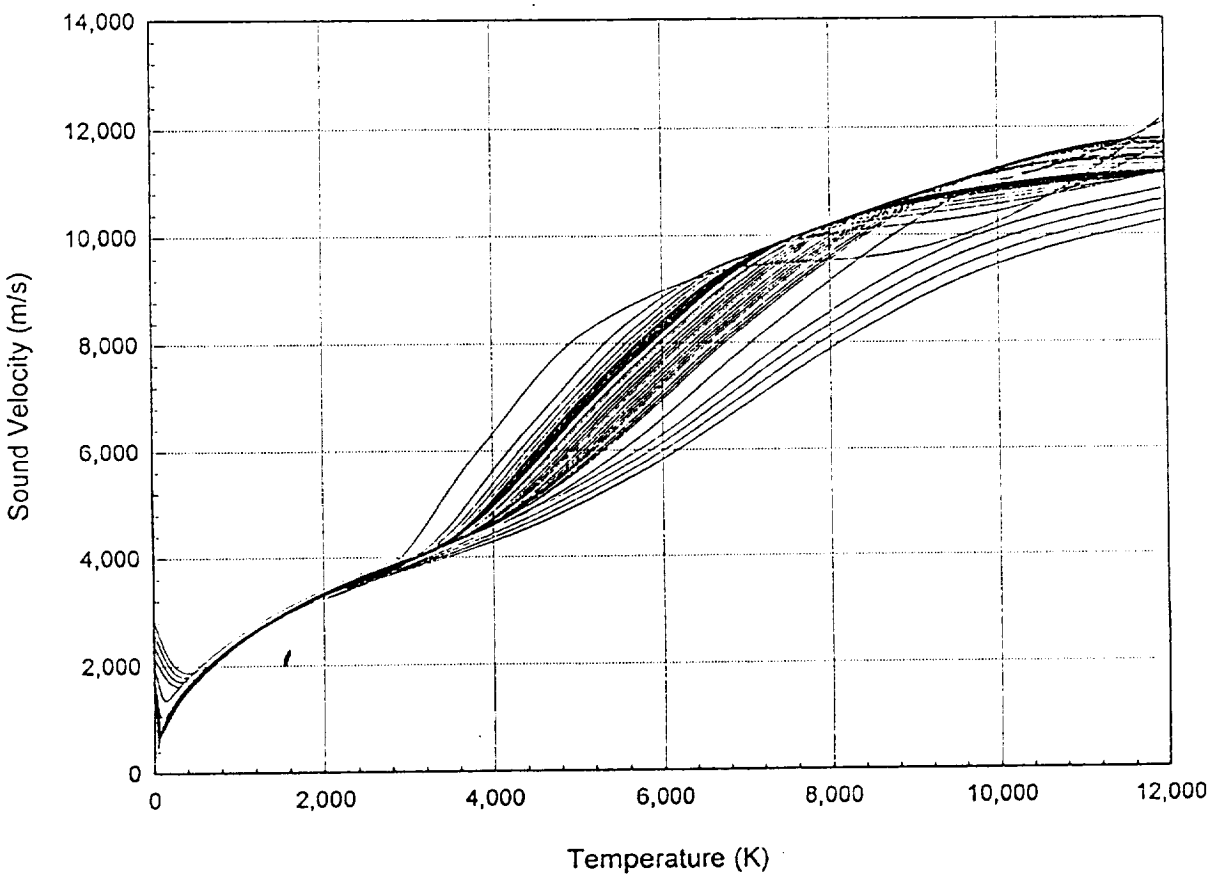

Figure 3-3 Sound speed in dissociated hydrogen for different pressure.

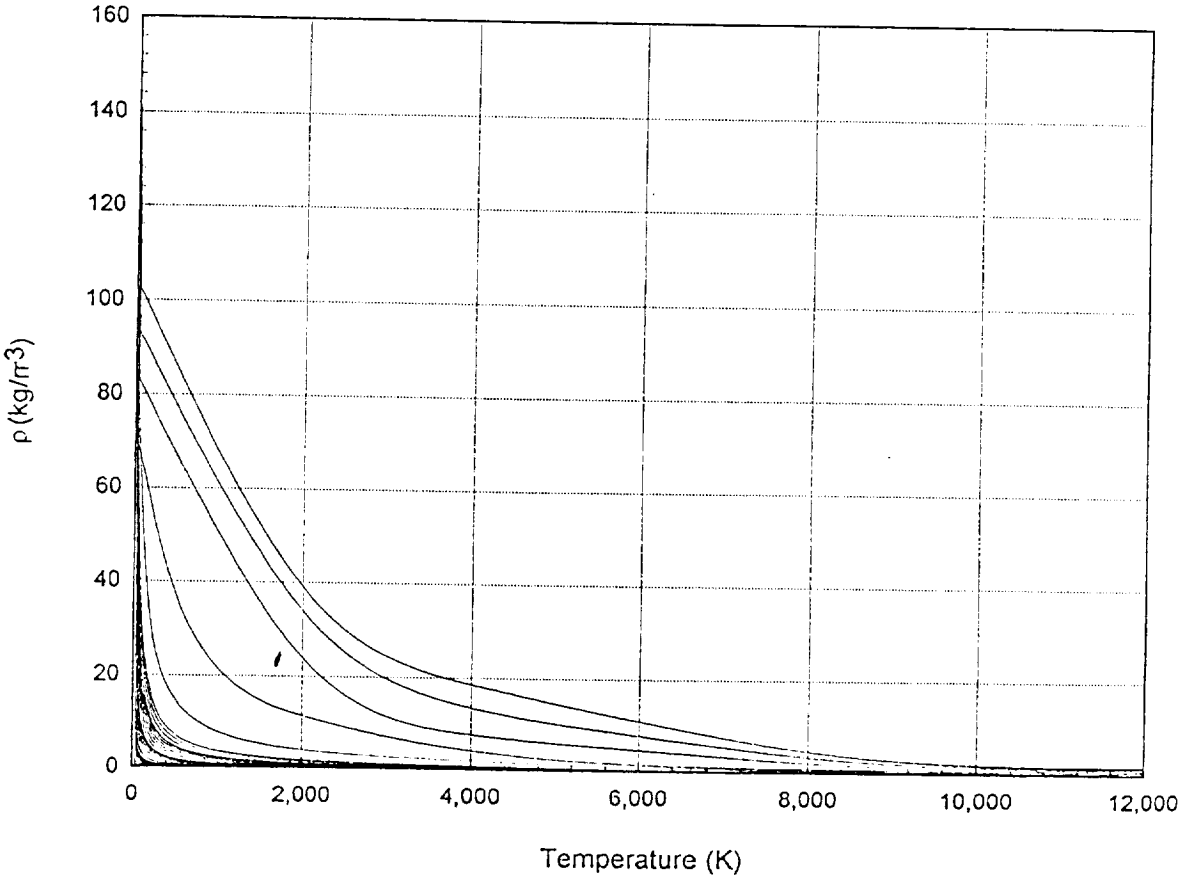

Figure 3-4 Density of dissociated hydrogen for different pressure.

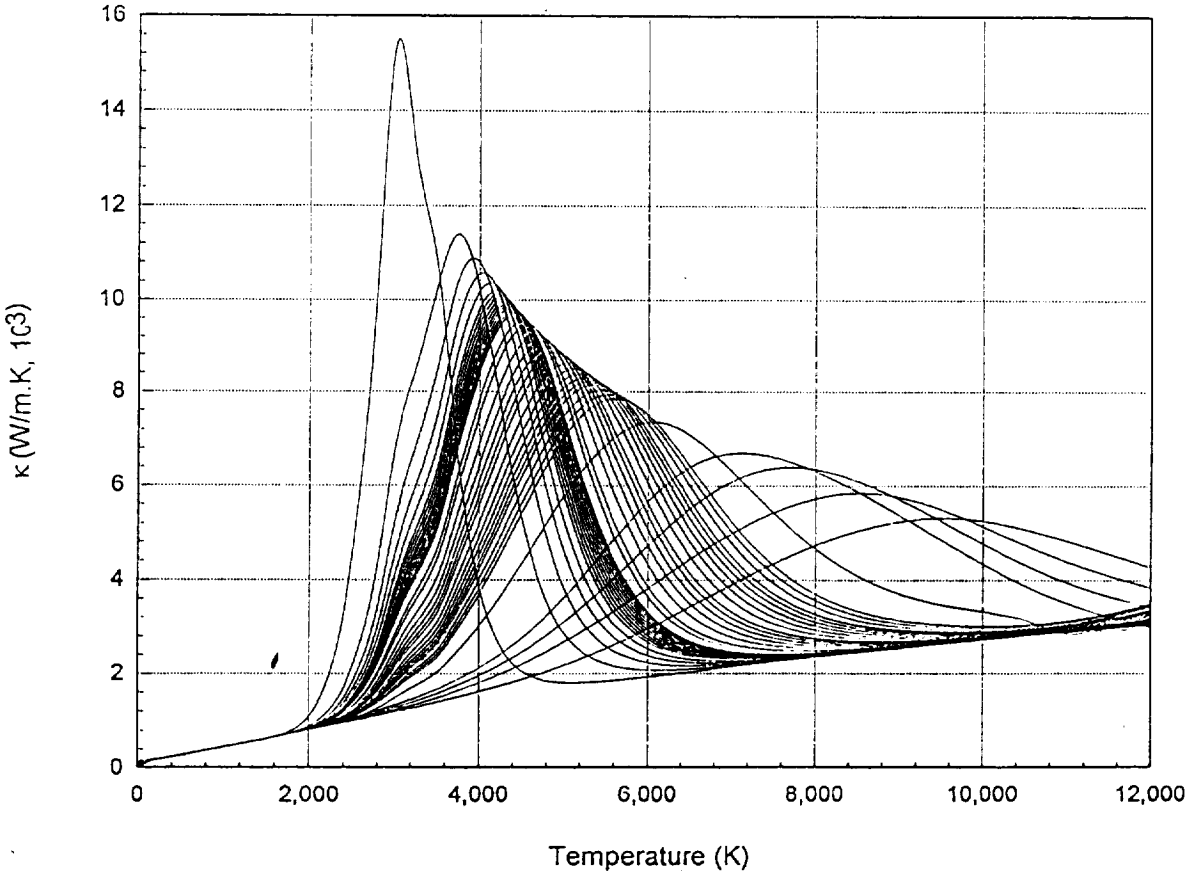

Figure 3-5 Thermal conductivity of dissociated hydrogen for different pressure.

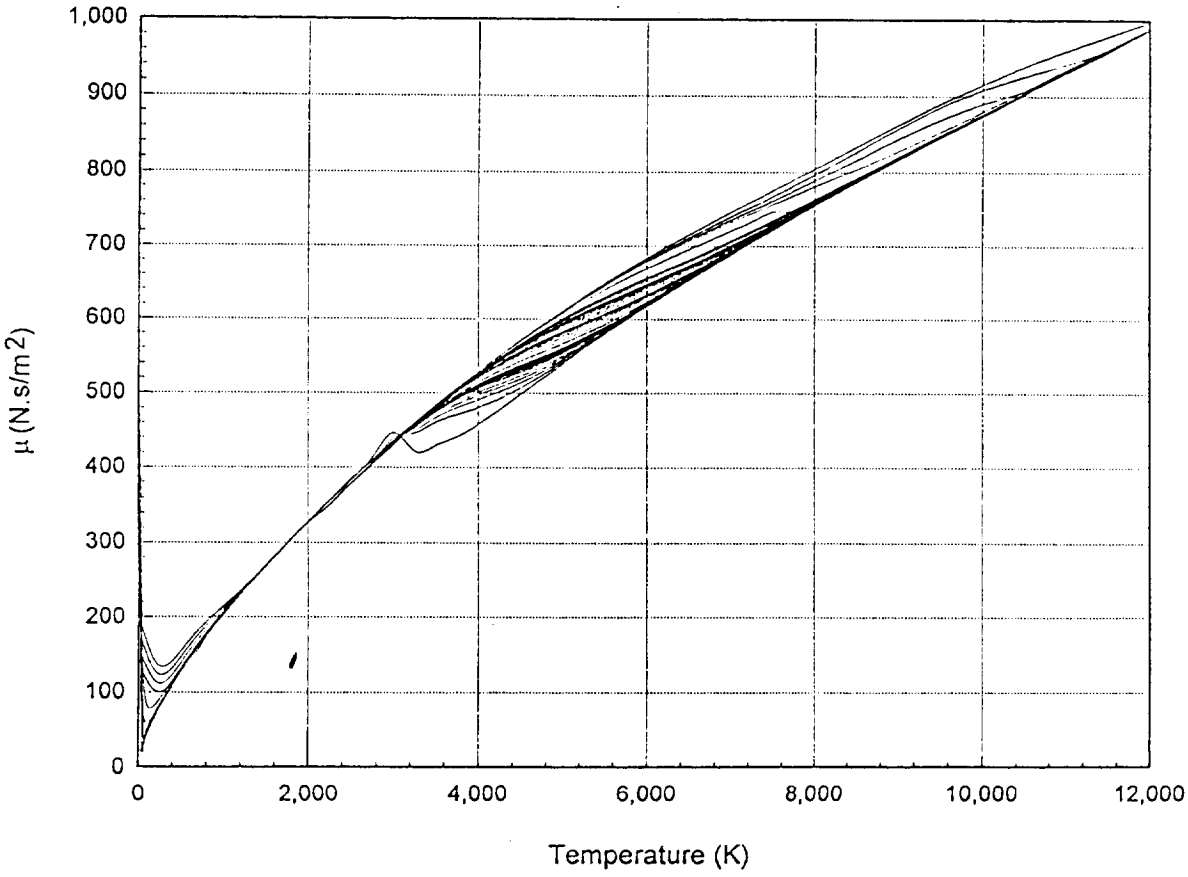

Figure 3-6 Viscosity of dissociated hydrogen for different pressure.

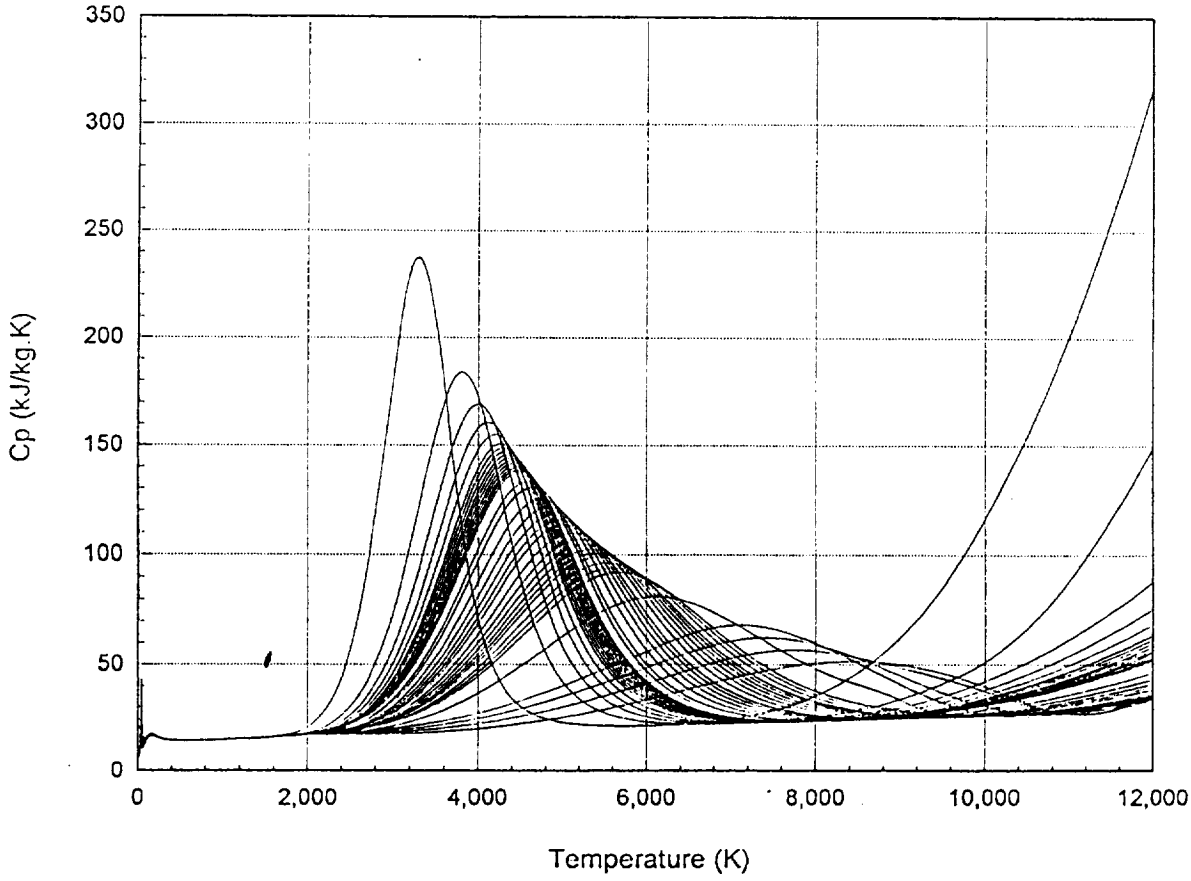

Figure 3-7 Specific heat of dissociated hydrogen for different pressure.

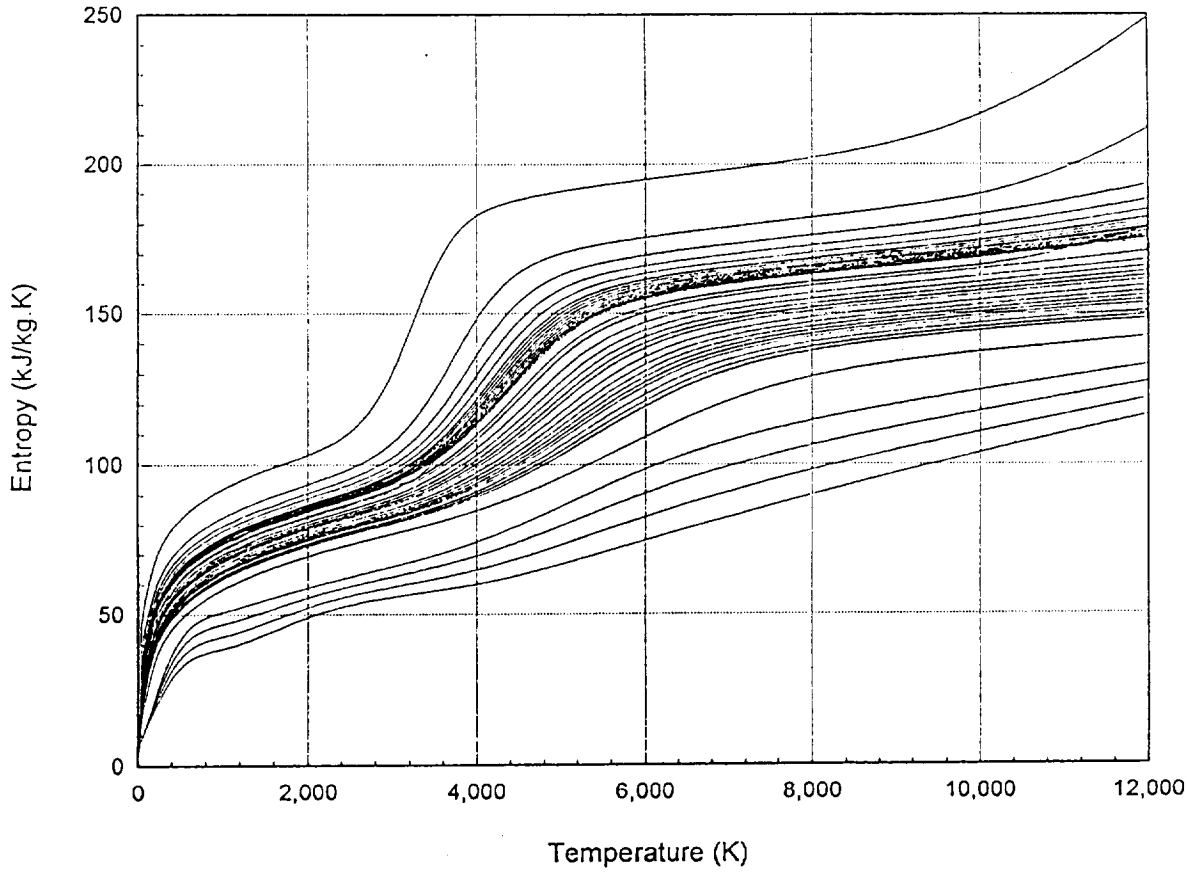

Figure 3-8 Entropy of dissociated hydrogen for different pressure.

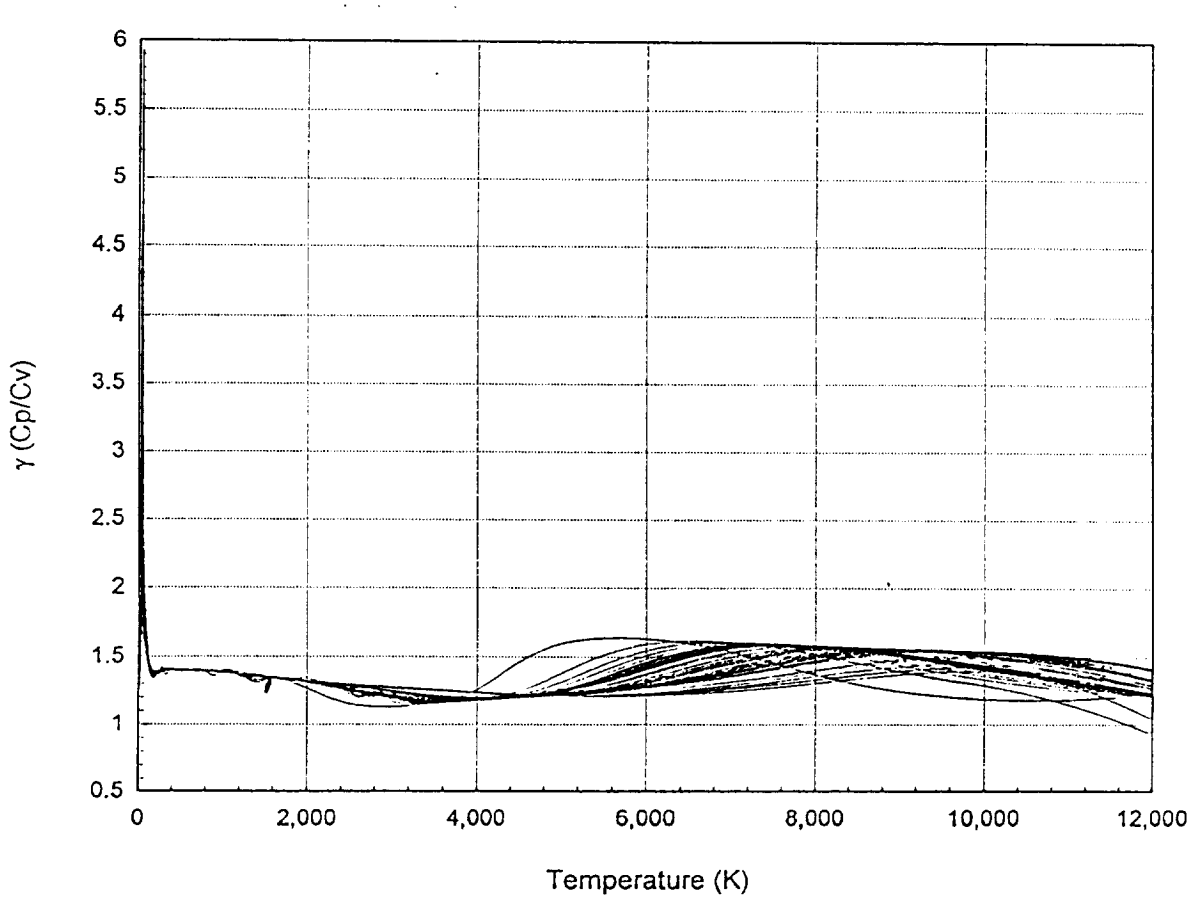

Figure 3-9 Ratio of specific heat of dissociated hydrogen for different pressure.

CHAPTER 4
ASSESSMENT OF NUMERICAL MODELING

In order to check the assessment and validation, several problems have been carried out to compare with published results. Excellent agreement with theoretical and experimental results has been obtained. The details of the tests are indicated in the following sections.

4.1 Drag Measurement and Separation Angle

Fluid flow studies over a sphere which is bounded in a cylindrical tube is of fundamental importance and has received attention for bounded flow. This is typical model for the low-drag measurement and determination of fluid viscosity. One of the parameters of paramount importance for the fluid flow over a bluff body is the separation angle. It is required for the drag force calculation and very difficult to ascertain by experimentation. In this study a numerical analysis is performed to observe the dependence of the separation angle on the diameter ratio between the sphere and the cylinder (γ). This study is based on the assumption that the Reynolds number is fairly high but low enough to have a laminar boundary layer. Figure 4-1 to 4-4 illustrate the flow patterns and separation angles for the cases γ=0.3, γ=0.4, γ=0.6 and γ=0.8, respectively. The results show that the separation angle reaches a minimum around γ=0.5. This result provides very good agreement with following semi-empirical equation which is based on the boundary layer analysis:[35]

$$\Phi(0.9277)+\Phi^3(2.095\gamma^2-0.3641)+\Phi^5(3.2466\gamma^4-1.5495\gamma^2+0.039)+ \\ +\Phi^7(4.396\gamma^6-13.4907\gamma^4+0.4687\gamma^2-0.0015)=0 \quad (5\text{-}1)$$

where Φ is function of separation angle. The following table provides the numerical results to compare the boundary layer approximation:

Table 4-1 Comparison of separation angle between numerical calculation and boundary layer approximation

DIAMETER RATIO	SEPARATION ANGLE (DEGREE)	
γ	Numerical Calculation	Boundary Layer Approximation
0.3	110.0	108.46
0.35	107.8	102.59
0.4	105.8	92.61
0.45	103.9	90.33
0.5	104.0	88.35
0.55	105.7	88.98
0.6	107.6	90.53
0.65	109.1	96.03
0.7	110.5	106.16

The comparison is shown in Figure 4-5.

An experiment was performed to measure drag force on a ball by using a Cahn instrument manufactured C2000 model microbalance. Teflon balls of different diameter were centrally hung in a long cylindrical tube of diameter 22.54 mm. The spheres were

suspended by means of a fine nylon string (d=0.07 mm), which can be found in reference [24]. A numerical investigation was carried out to compare with the experimental results. The drag force can be found from the following formula:

$$Drag = \sum_{i=1}^{i\max} \mu_i \frac{du}{dr} \tag{5-2}$$

where μ_i is viscosity.

Figure 4-6 provides the comparison between the numerical and experimental results. It is shown that by increasing the number of grid points on the sphere, the drag force results finally approach the experimental values.

4.2 Empirical Correlations of Nusselt Number

Among the long list of correlations for the Nusselt number, axial distance corrections and property corrections, the following correlations which have the more relevance to heat transfer in a nuclear reactors are chosen to justify the validity of computational results.[15,38]

(1) Empirical Correlations of Nusselt Number

1. Colburn correlation (1933)

$$Nu = 0.023\,\mathrm{Re}^{0.8}\,\mathrm{Pr}^{\frac{1}{3}} \tag{4-3}$$

2. Dittus-Boelter correlation (1930)

$$Nu = 0.023\,\mathrm{Re}^{0.8}\,\mathrm{Pr}^{n} \qquad n = \begin{cases} 0.4 & T_w > T_b \\ 0.3 & T_w < T_b \end{cases} \tag{4-4}$$

3. Seide-Tate correlation (1936)

$$Nu = 0.027\,\mathrm{Re}^{0.8}\,\mathrm{Pr}^{1/3}\left(\frac{\mu_b}{\mu_w}\right)^{0.14} \tag{4-5}$$

4. Gnielinski-Petukov correlation (1970)

$$Nu = \frac{(\mathrm{Re}-1000)\,\mathrm{Pr}\left(\frac{f}{2}\right)}{1.07 + 12.7\left(\mathrm{Pr}^{\frac{2}{3}}-1\right)\sqrt{\frac{f}{2}}} \tag{4-6}$$

5. Karman-Boelter-Martinelli correlation (1960)

$$Nu = \frac{\mathrm{Re}\,\mathrm{Pr}\sqrt{\frac{f}{2}}}{0.833\left\{5\,\mathrm{Pr} + 5\ln(5\,\mathrm{Pr}+1) + 2.5\ln\left(\mathrm{Re}\frac{\sqrt{\frac{f}{2}}}{60}\right)\right\}} \tag{4-7}$$

where

$$f = 0.0014 + \frac{1}{8}\mathrm{Re}^{-0.32}$$

6. Notter-Sleicher correlation (1975)

$$Nu = 5.0 + 0.015\,\mathrm{Re}^{a}\,\mathrm{Pr}^{b} \tag{4-8}$$

where

$$a = 0.88 - \frac{0.24}{\mathrm{Pr} + 4}$$

$$b = \frac{1}{3} + 0.5e^{-0.6\,\mathrm{Pr}}$$

7. Churchill correlation (1977)

$$Nu = \left\{ a^{10} + \left[\frac{e^{\frac{(2300-\mathrm{Re}}{365}}}{b^2} + \left(\frac{1}{c + \frac{0.079\,\mathrm{Re}\,\mathrm{Pr}\sqrt{f}}{\left(1+\mathrm{Pr}^{4/5}\right)^{5/6}}} \right)^2 \right]^{-5} \right\}^{\frac{1}{10}} \tag{4-9}$$

where

$$a = 4.364\left[1 + \left(\frac{\mathrm{Re}\,\mathrm{Pr}\,D}{7.3L} \right)^2 \right]^{\frac{1}{6}}$$

$$b = 4.364\left[1 + \left(\frac{287\,\mathrm{Re}\,\mathrm{Pr}\,D}{L} \right)^2 \right]^{\frac{1}{6}}$$

$$c = 6.3$$

(2) Axial Distance Corrections for Nusselt Number

1. Perkins and Worsoe-Schmidt correction (1965)

$$f_z = \left[1 + \left(\frac{z}{D} \right)^{-0.7} \left(\frac{T_w}{T_b} \right)^{0.7} \right] \tag{4-10}$$

2. Pierce correction (1963)

$$f_z = \left[1 + 0.3\left(\frac{z}{D}\right)^{-0.7} \right] \tag{4-11}$$

3. Bussard correction (1965)

$$f_z = \left[1.957\left(1 + \frac{z}{D}\right)^{-0.15} \right] \tag{4-12}$$

4. Reynolds-Swearington correction (1965)

$$f_z = \left[1 + 0.8\left(1 = 70{,}000\,\mathrm{Re}^{-1.5}\right)\left(\frac{z}{D}\right)^{-1} \right] \tag{4-13}$$

(3) Property Corrections for Nusselt Number

1. Notter-Sleicher property correction

$$f_p = \left(\frac{T_w}{T_b}\right)^{0.3-\left(\log_{10}\left(\frac{T_w}{T_b}\right)\right)^{0.25}} \tag{4-14}$$

2. Volkov-Vanov property correction

$$f_p = \left(\frac{T_w}{T_b}\right)^{-0.55} \tag{4-15}$$

3. Perkins and Worsoe-Schmidt property correction

$$f_p = \left(\frac{T_w}{T_b}\right)^{-0.7} \tag{4-16}$$

Figure 4-7 compares the numerical results with four Nusselt number correlations. These correlations include the Colburn equation, the Gnielinski correlation, the Karman-Boelter-Martinelli equation and the Notter-Sleicher correlation. Figure 4-7 shows that numerically calculated Nusselt number with some of empirical correlation results is almost undistinguished. This comparison not only evaluated the empirical correlations of Nusselt number, but also assessed the validation of numerical modeling.

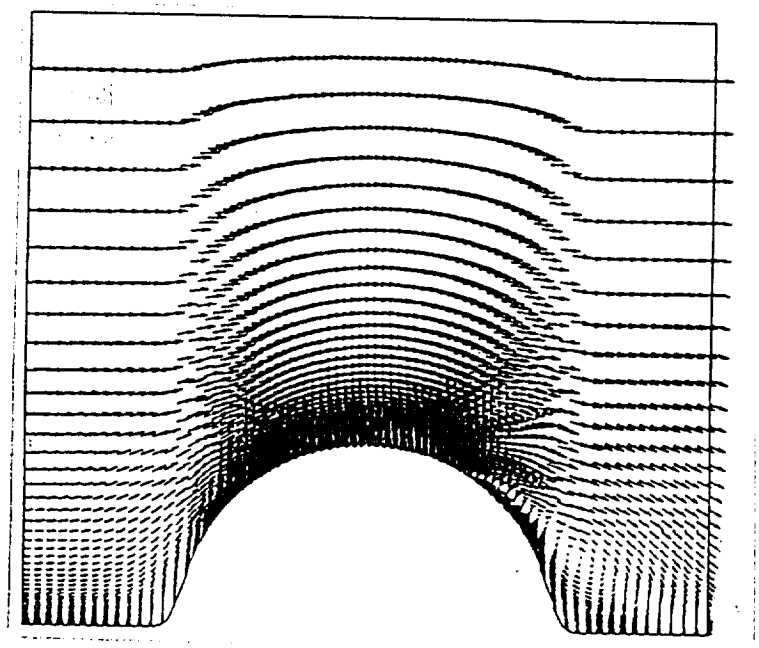

Figure 4-1 Flow pattern and separation angle for γ=0.3 (Φ=110°).

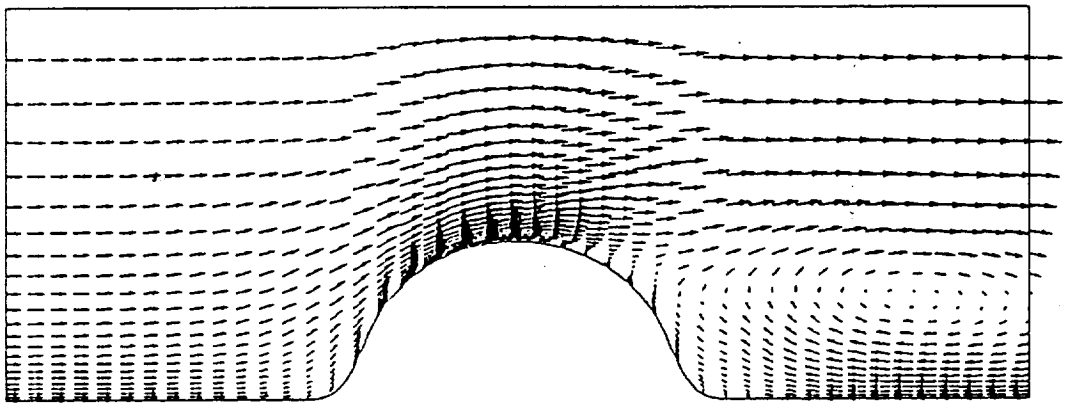

Figure 4-2 Flow pattern and separation angle for γ=0.4 (Φ=105.8°).

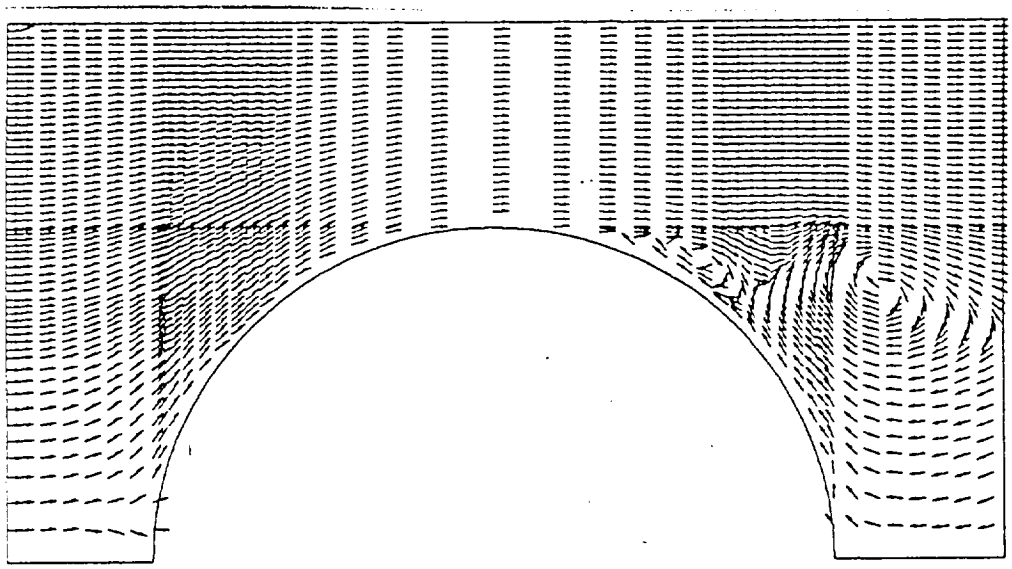

Figure 4-3 Flow pattern and separation angle for γ=0.6 (Φ=107.6°).

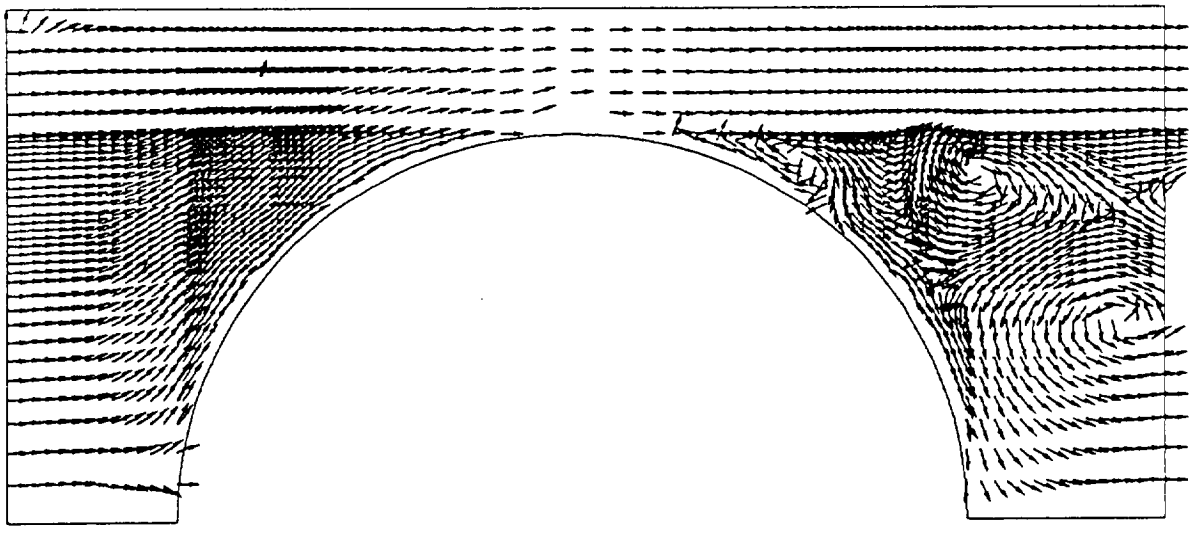

Figure 4-4 Flow pattern and separation angle for γ=0.8 (Φ=114.3°).

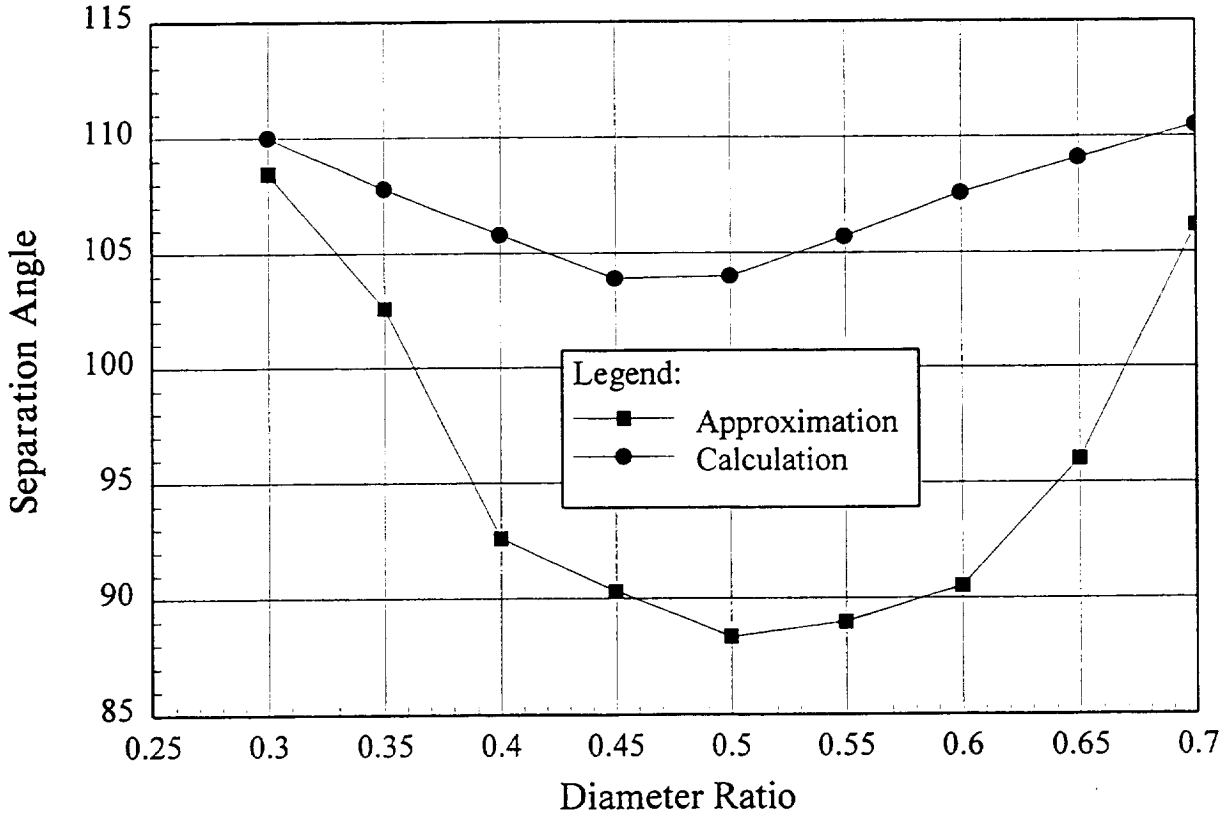

Figure 4-5 Comparison of separation angle between numerical calculation and boundary layer approximation.

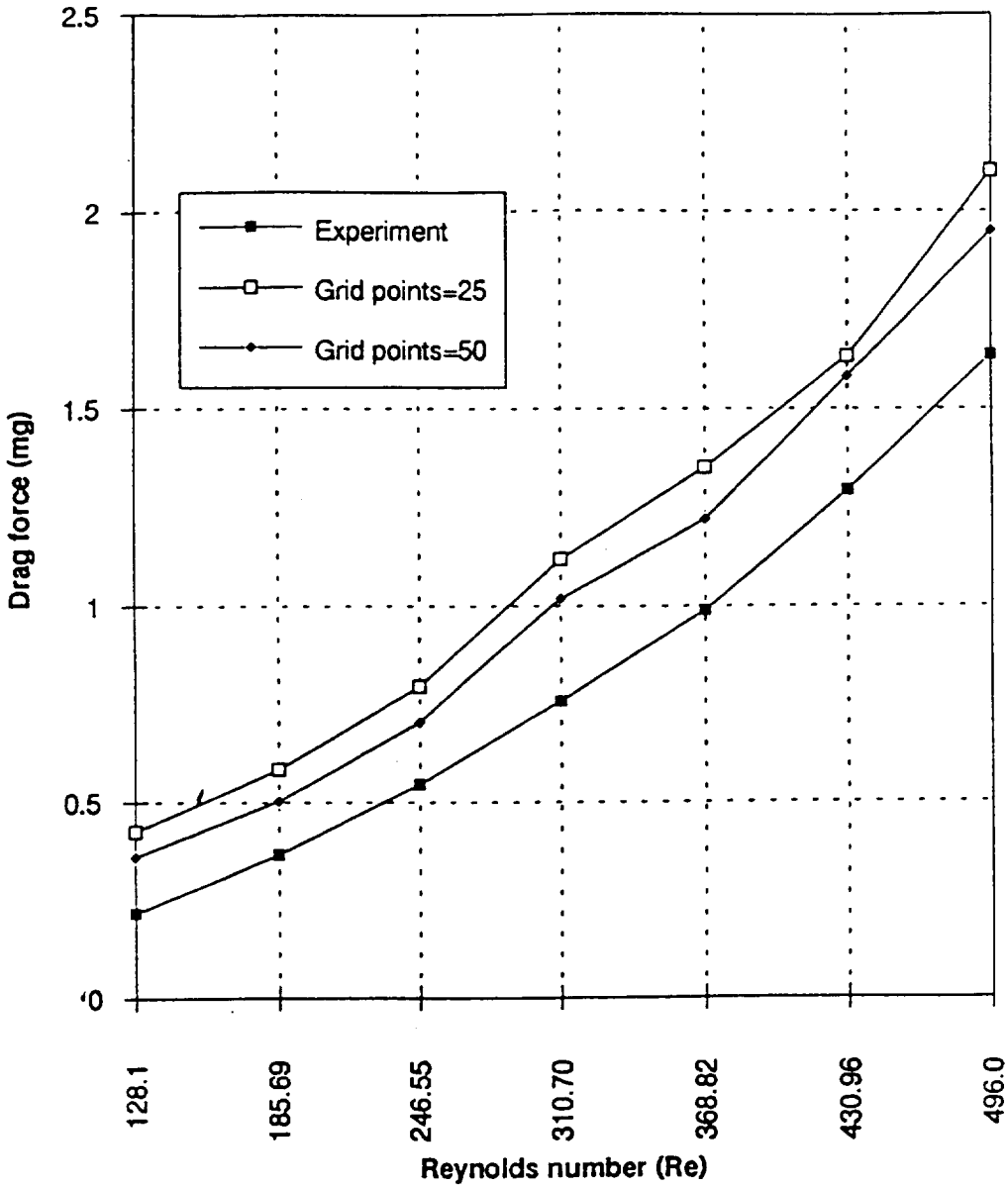

Figure 4-6 Comparison between calculated and experimental values of drag force (From Reference [23]).

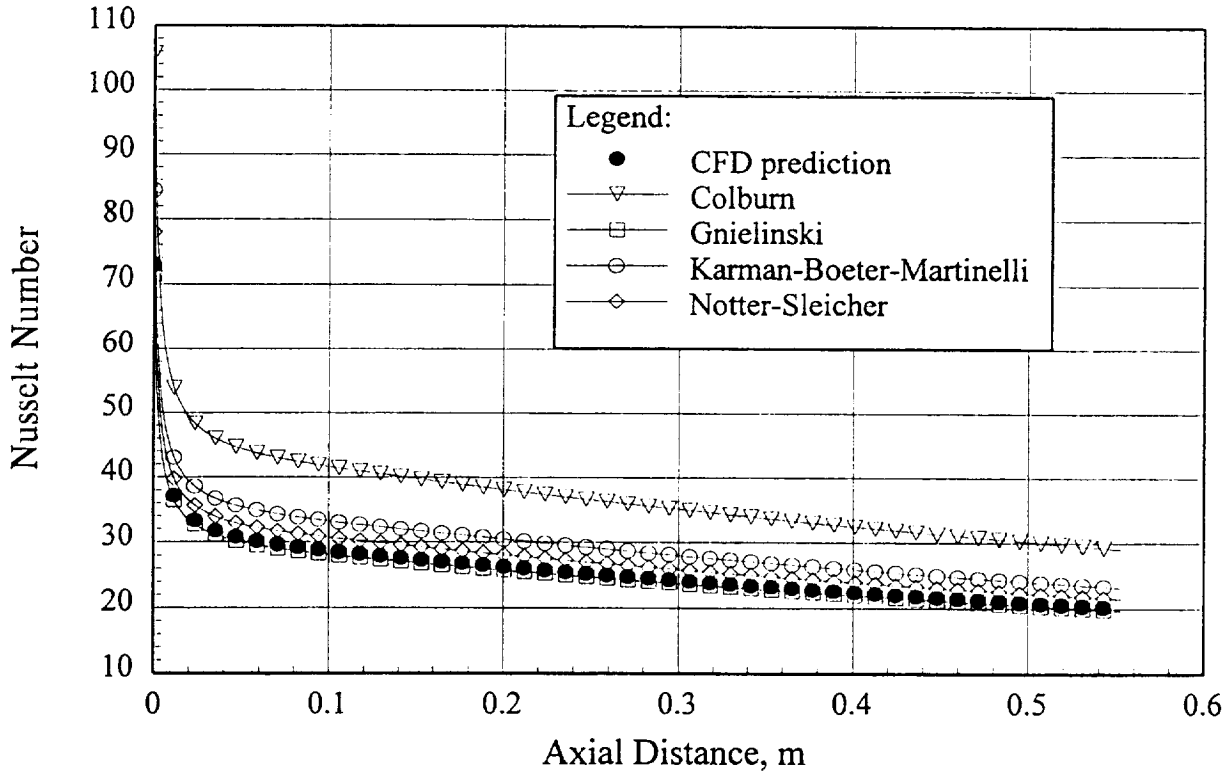

Figure 4-7 Comparison of the numerically calculated Nusselt number with the empirical correlations.

CHAPTER 5
RESULTS AND DISCUSSION

This chapter is composed of three parts. The first part presents the numerical results for the fluid flow and heat transfer in the core of a gaseous core nuclear reactor. UF_4 gas is used to simulate the flow of a Ultrahigh Temperature Vapor Core Reactor with Magnetohydrodynamic generator (UTVR-MHD) system. The second part describes the numerical results for fluid flow and heat transfer in the core of a gas cooled reactor. Helium gas is utilized in this part. The last part indicates the results for the fluid flow and heat transfer in XNR2000 nuclear rocket core. Hydrogen gas is considered in this study.

5.1 Calculations for a Gaseous Core Reactor

A gas core reactor uses a gaseous fissile material as fuel for power generation. This allows for power generation at temperatures much higher than the melting point of solid fuel nuclear reactors. Power generation and power conversion at very high temperatures can potentially reduce the system mass and improve the specific impulse of a nuclear thermal rocket. One of the most challenging issues related to design and operation of gas core reactors is the containment of the fissioning plasma. The wall cooling is the most important issue in design of gaseous core nuclear reactors. The heat transfer process involved in an ultrahigh temperature gas core reactor systems is characterized by the convective flow of a radiating gas. Uranium and uranium compound gases even at pressures in the range of 10 to 40 atm are optically thick. At temperatures close to 3500°K which is the typical exit temperature of the reactor core in a recent design,[13] the radiative heat

transfer rate in these opaque gases is higher and comparable with the convective heat transfer rate.[12] Therefore, the heat transfer analysis of a fissioning gas must include both convective and radiative transfer. The flow and radiation transport equations must be solved simultaneously in order to determine the temperature distribution and heat transfer rate.[39,42]

The model presented in this paper considers combined convection and radiation of compressible, turbulent and developing flow of a radiating gray gas under very high temperature conditions. Although the combined convective and radiative heat transfer problem has been the target of many investigations, a comprehensive numerical solution of this problem has not yet been published.[21,32]

The case selected for this analysis consists of a cylindrical tube 1m long and 0.05m in diameter, i.e. z/D=20. The constant wall temperature is set at 1600°K, and total inlet temperature is specified as 2000°K, which is a typical design temperature at the core inlet of the ultrahigh temperature vapor core reactor system. A stagnation inlet pressure of 2 MPa, the back pressure of 1.8 MPa and three different values of internal heat generation rate of 100 MW/m^3, 500 MW/m^3 and 1000 MW/m^3 are used. The Reynolds number is ranged from 10^4 to 10^6.

The flow domain is divided into 54 radial and 54 axial control volumes spaced non-uniformly. A fine grid, defined by algebraic method, was used near the wall to ensure more than two grid points in the laminar sublayer, as shown in Figure 5-1.

5.1.1 The Temperature Distribution

The temperature distributions, which are obtained at a constant wall temperature of 1600°K and inlet stagnation temperature of 2000°K, are used for verification of effect of internal heat generation rate and are presented in Figure 5-2. The relations between temperature distribution and internal heat generation rate will be discussed in the next section. The numerical results are compared with the results of Hoogenboom et al.[18]

Figure 5-3 shows that the maximum temperature and the trend are almost undistinguished. The Nusselt number for pure convection is compared with the results of Petukhov-Kirillov-Grielinski equation, which is shown in Figure 5-4. The differences between those two results are less than 3% at the tube exit (z=1m). The excellent agreement between the present model and the previous literature indicates the validity of the numerical modeling for gaseous core reactors.

All of the above results are obtained from the solution of the flows at the steady-state. In order to verify the steady state solution, the convergence history for the velocity and temperature residual is examined, as shown in Figure 5-5. In this case, the steady state is reached when the root-mean-squared residuals of velocity and temperature drop 5 and 4 orders of magnitude in about 900 iterations or 300 minutes of CPU time using a 486-66 computer. The velocity and temperature residuals are defined by

$$\delta_v = \frac{\sum_{i=1}^{imax}\sum_{j=1}^{jmax}\left[\left(u_{i,j}-u_{i,j}^{n+1}\right)^2+\left(v_{i,j}-v_{i,j}^{n+1}\right)^2\right]^{\frac{1}{2}}}{(i\max)(j\max)} \tag{5-1}$$

$$\delta_T = \frac{\sum_{i=1}^{imax}\sum_{j=1}^{jmax}\left[\left(T_{i,j}-T_{i,j}^{n+1}\right)^2\right]^{\frac{1}{2}}}{(i\max)(j\max)} \tag{5-2}$$

5.1.2 Effect of Heat Generation Rate

Gas core nuclear reactors are characterized by high internal heat generation rate in the fissile gas. The numerical model is used to predict the temperature distribution and heat transfer rate for the gases with internal heat generation. Uniform heat generation rates ranging from 100MW/m^3 to 1000MW/m^3 are included in the energy equation as source terms.

In Figure 5-6, the temperature distribution is presented for the three different values of heat generation rate. Because of the radiative heat transfer, the curves become more flat and grow faster than those of pure convection. The convective heat flux at the wall increases as the power generation rate increases. The Figure 5-6 also shows that the temperature at a heat generation rate of 1000 MW/m^3 increases more rapidly than others because the radiation at high temperature is more dominant.

The maximum temperature, corresponding to the heat generation rates, are 2150°K , 2750°K and 3550°K, respectively. This is indicates that a heat generation rate higher than $1000MW/m^3$ is necessary to maintain the gas temperature at about 3500°K, which is typical temperature required to achieve high efficiency in the gas core reactors.[32] The bulk temperature gradient at the wall is steeper than it would be in pure convection, which is shown in Figure 5-2. These results indicate that the maximum temperature in the reactor is strongly dependent on the value of heat generation rate.

5.1.3 Convective and Radiative Heat Fluxes

The heat fluxes are presented for both convective and radiative heat transfer. The convective, radiative and total heat flux transferred to the wall are calculated using the following equations:[37]

$$q_t = \frac{\int_0^R \rho u C_p T r dr \Big|_{x+\Delta x} - \int_0^R \rho u C_p T r dr \Big|_x}{R\Delta x} - \dot{Q}\Big|_x^{x+\Delta x} \tag{5-3}$$

$$q_c = -k\left(\frac{\partial T}{\partial r}\right)_{r=R} \tag{5-4}$$

$$q_r = q_t - q_c \tag{5-5}$$

where q_t, q_c and q_r are the total, convective and radiative heat fluxes, respectively. The convective and radiative heat fluxes for the three different cases are presented in Figure 5-7. As the heat generation rate increases, the corresponding heat flux increases. It is found that at temperature close to 3500°K the radiative heat transfer rate is comparable with the convective heat transfer. It is seen that the radiative fluxes increase as higher wall temperatures. This behavior is due to the fact that the radiative wall heat flux is dependent on the local conditions at the wall.

5.1.4 Nusselt number calculation

Nusselt number is the parameter which characterizes the heat transfer rate at the wall boundary. The total, convective and radiative Nusselt number can be defined as:

$$Nu_c = \frac{q_c D}{k(T_w - T_b)} \tag{5-6}$$

$$Nu_r = \frac{q_r D}{k(T_w - T_b)} \tag{5-7}$$

$$Nu_t = Nu_c + Nu_r \tag{5-8}$$

Figure 5-8 illustrates the relation between local Nusselt number and Reynolds number. It is found that the Nusselt number increases as the heat generation rate decreases. This is mainly due to the increase of dynamic viscosity of UF_4 gas as temperature increases. Figure 5-8 also shows that the entrance length increases as the Nusselt number decreases.

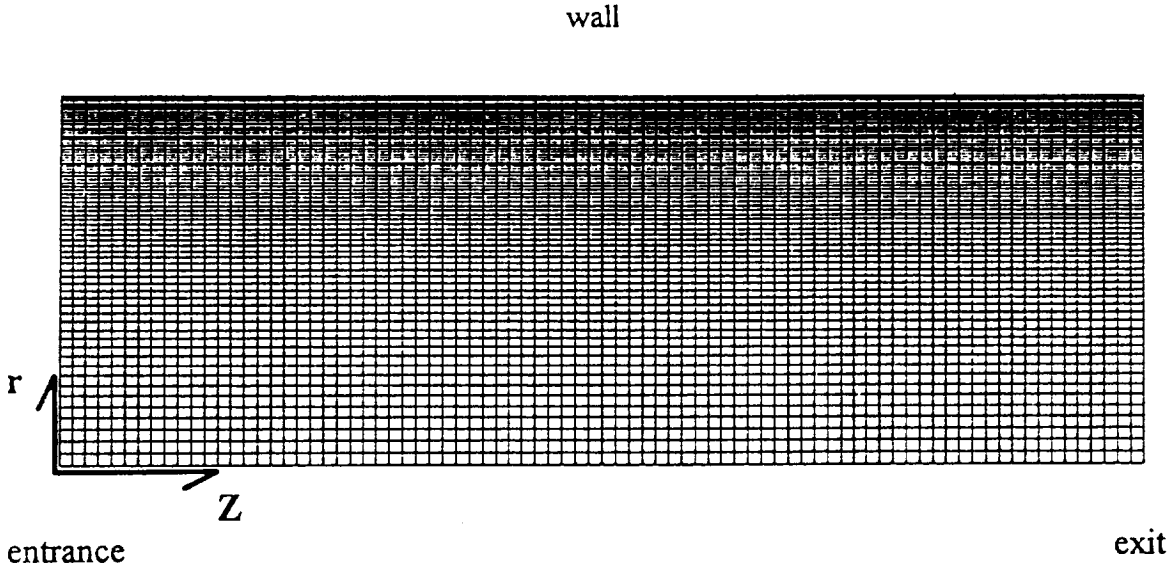

Figure 5-1 Overall view of grid system.

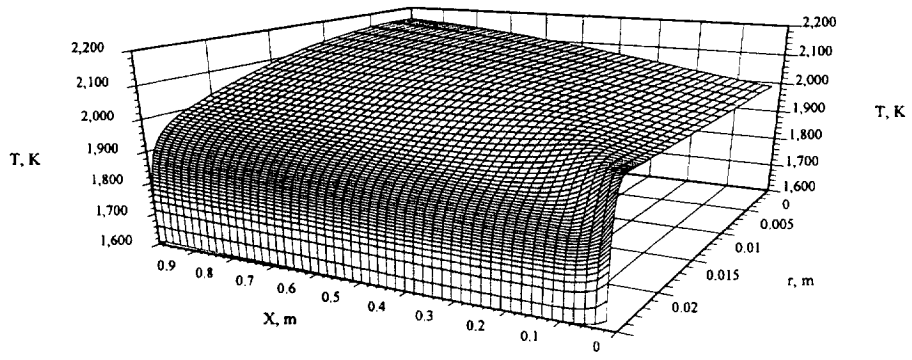

(1)

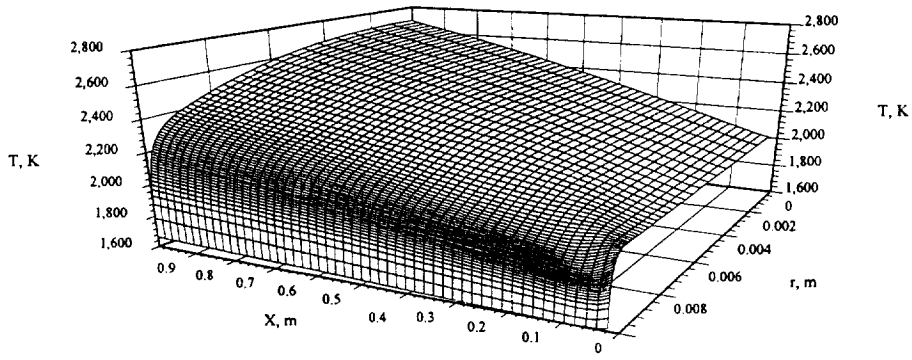

(2)

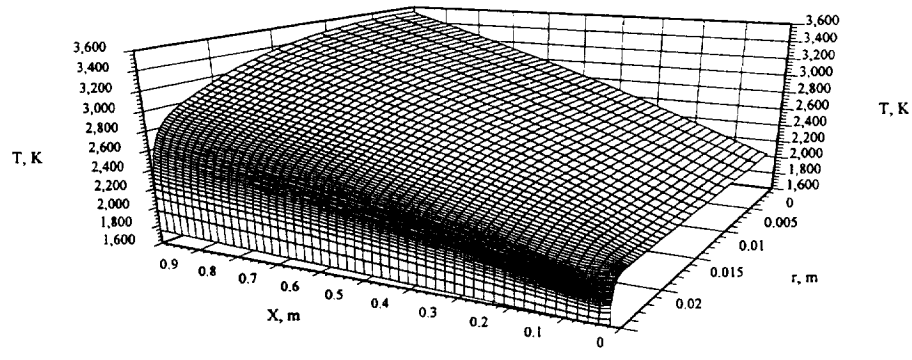

(3)

Figure 5-2 Comparison of temperature distribution for different values of heat generation rate: (1) Q=100 MW/m^3, (2) Q=500 MW/m^3 and (3) Q=1000 MW/m^3.

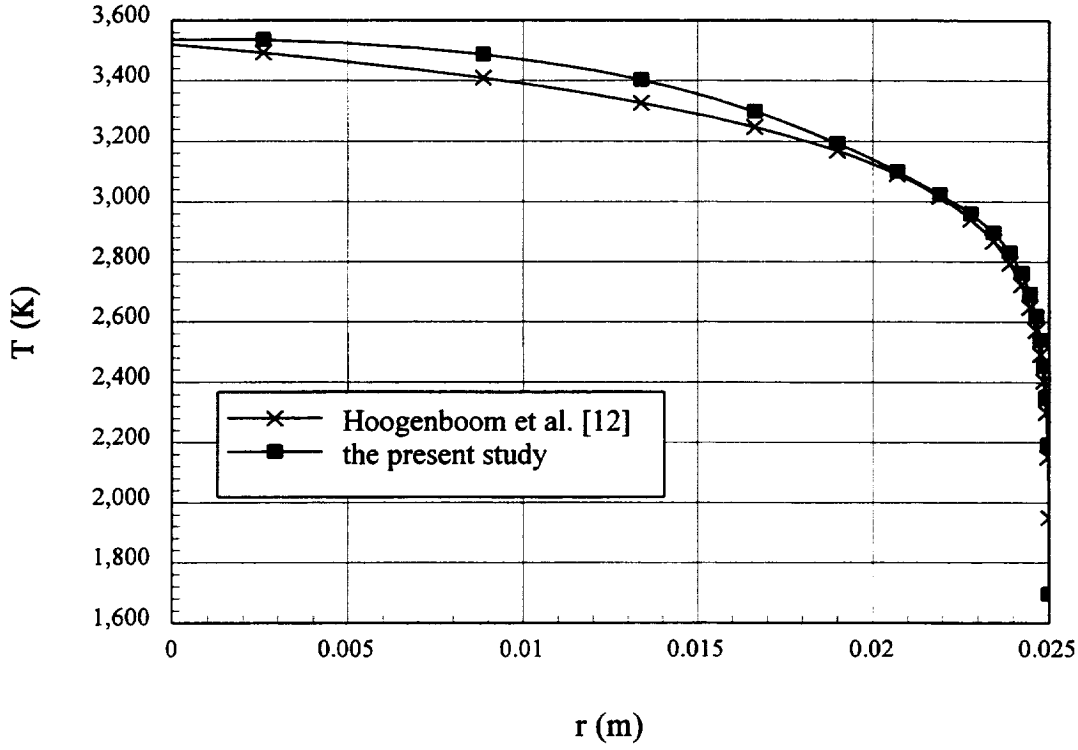

Figure 5-3 Temperature distribution comparison between results obtained with the present methodology and by Hoogenboom et al.

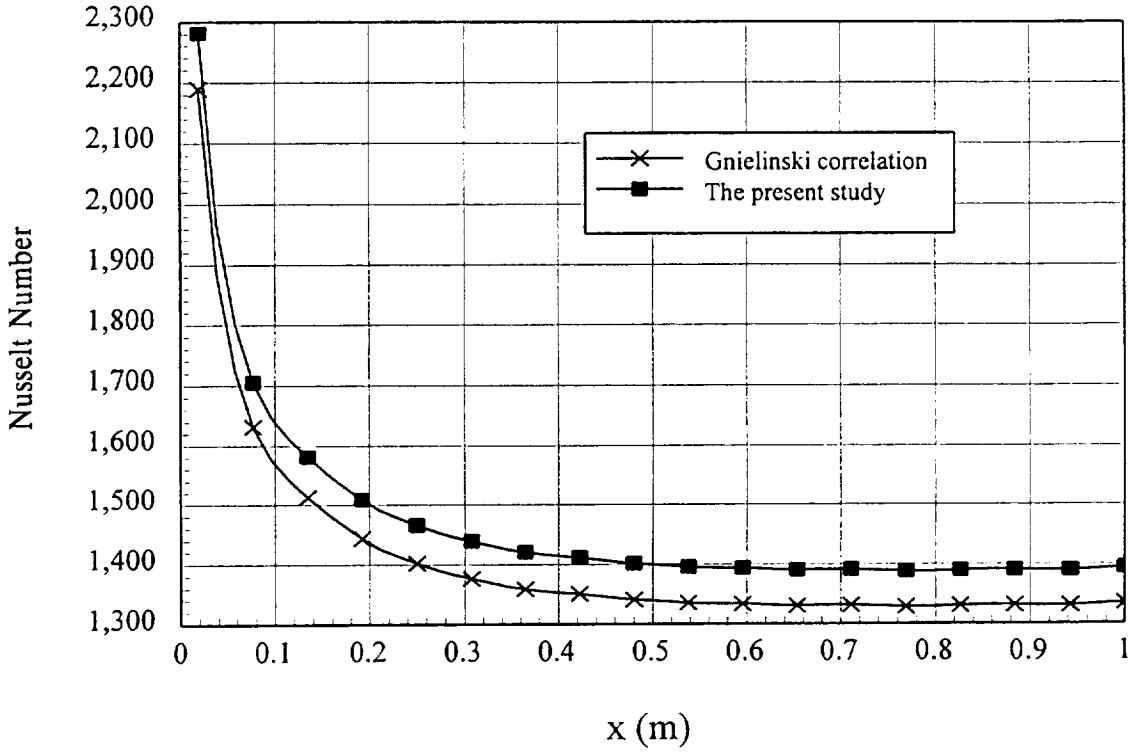

Figure 5-4 Convective Nusselt number comparison between results obtained with the present methodology and by using Petukhov-Kinllov-Gnielinski correlation.

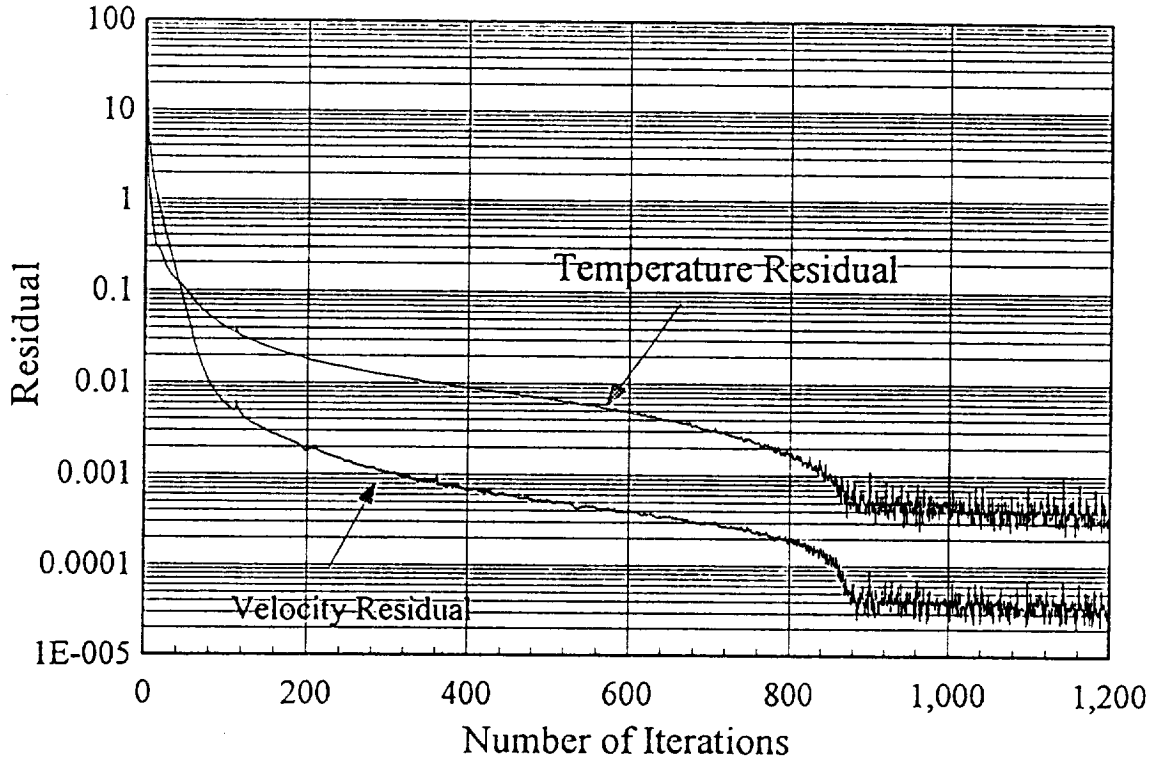

Figure 5-5 Convergence history (Q=1000 MW/m^3).

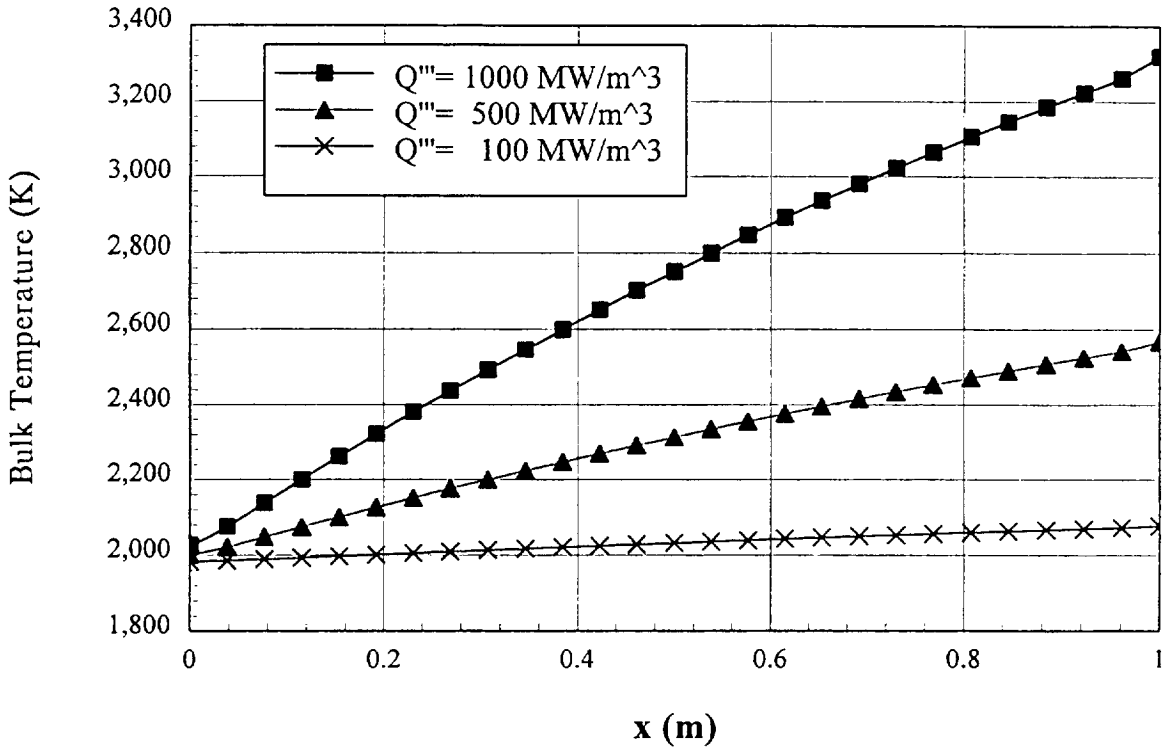

Figure 5-6 Comparison of bulk temperature for different values of heat generation rate.

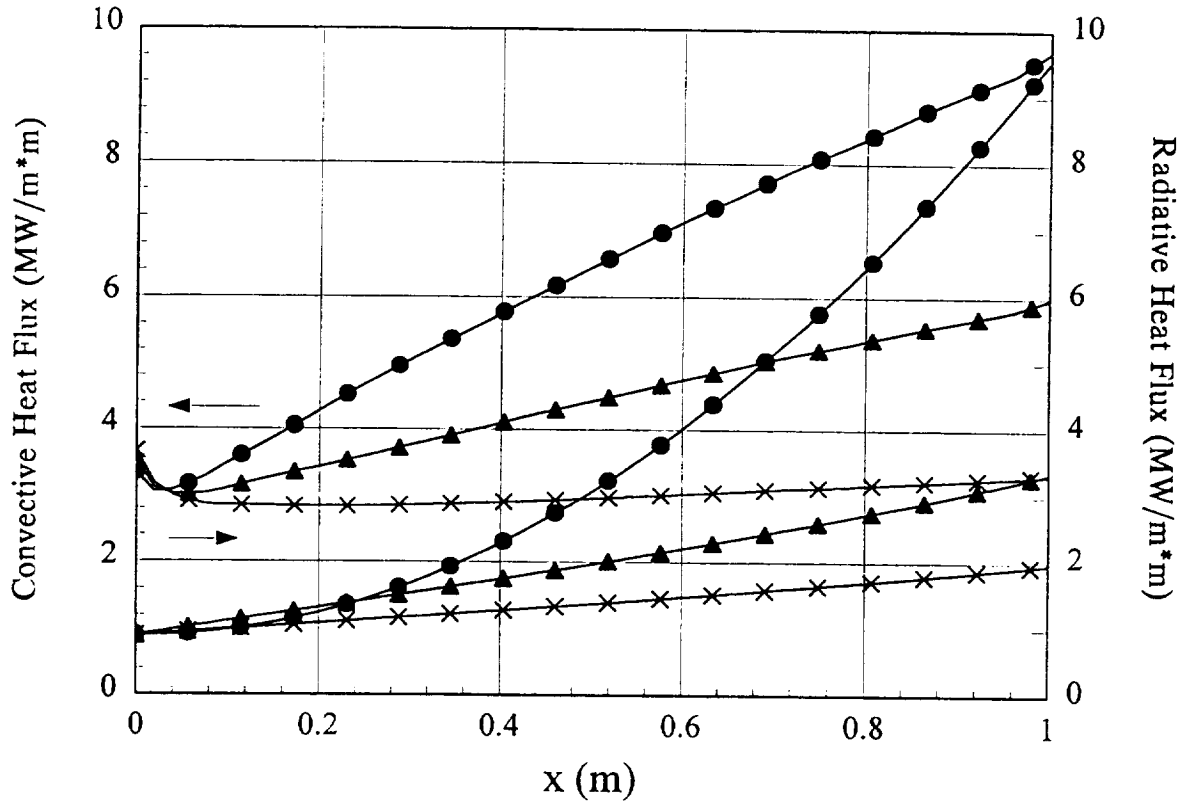

Figure 5-7 Convective and radiative heat flux as a function of axial location: -×- Q= 100 W/m^3, -Δ- Q=500 MW/m^3, -O- Q=1000 MW/m^3.

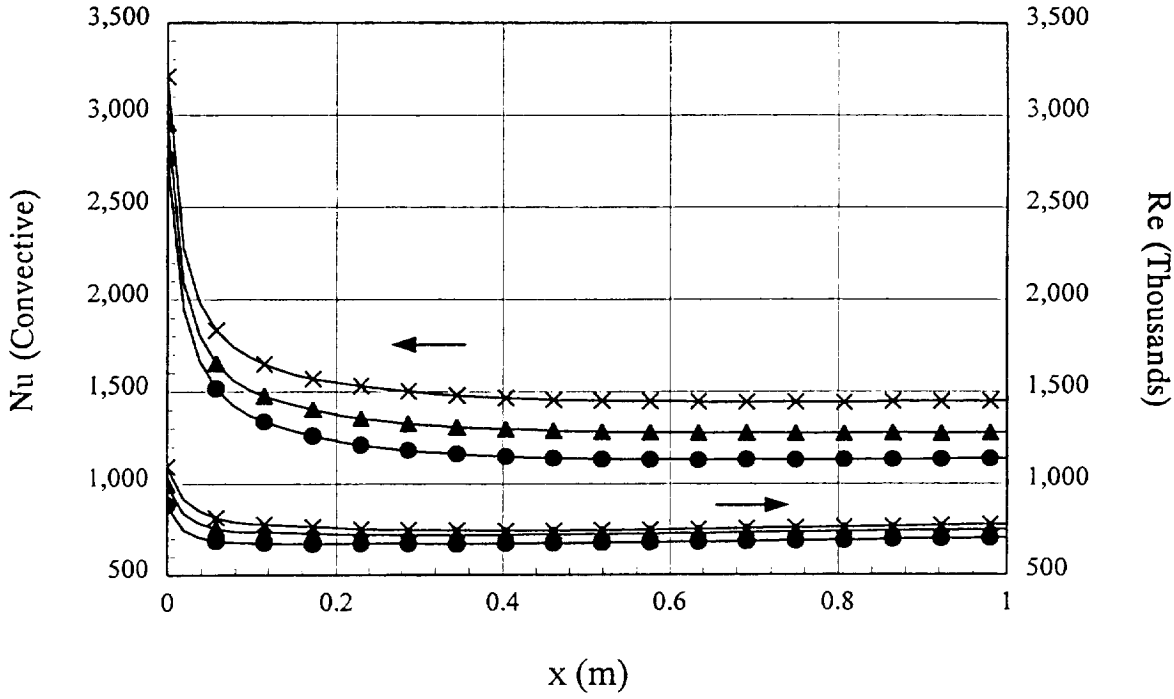

Figure 5-8 Local Reynolds number and Nusselt number variation: -×- Q= 100 W/m^3, -Δ- Q=500 MW/m^3, -O- Q=1000 MW/m^3.

5.2 Calculations for a Gas Cooled Reactor

Over the past few decades, high temperature gas cooled reactors (HTGRs) have been considered for a wide range of applications. Compactness, high efficiency and very high temperature capability of these reactors are of great importance to power generation in space. Other applications of HTGRs include: terrestrial electric power generation, nuclear thermal propulsion and direct use of high temperature gas for a variety of industrial processes such as steel-making.[19] The technology of HTGRs for commercial power generation, as well as the computational methods for analysis of thermal fluid performance of these reactors are well developed. The majority of existing HTGR thermal fluid analysis methods use empirical correlation to resolve heat and momentum transfer at the fuel-coolant boundary. However for HTGR concepts with operating parameters beyond those of commercial HTGRs, the issue of the accuracy and applicability of empirical correlations are not fully resolved. In particular, energy transport in very compact space power reactor concepts may require flow at very high velocities and high Reynolds numbers. This study presents a non-correlation based computational thermal-fluid model to analyze flow and heat transfer in HTGR cores. The computational model is also used to assess the performance of several mechanistic correlations for calculation of pressure drop in HTGR

A dual path cermet fuel fast spectrum reactor is used as a computational model to analyze the high-temperature gas-cooled reactor system. The core consists of 631 fuel rods and 37 holes per fuel rod which has a flow-equivalent diameter of 3.2 mm and heated length of 0.544 m. The stagnation inlet pressure of 6.5 MPa, the back pressure of 5 MPa and the core power of 25 MW, 50 MW, 75 MW and 100 MW are used, respectively. The Reynolds number of the flow is in the range of 10^4 to 10^5.

The flow domain was divided into 54 radial and 54 axial control volumes spaced non-uniformly. A fine grid, defined by an algebraic method, was used near the wall to

ensure more than two grid points in the laminar sublayer which is used to control the heat flux near the wall. Figure 5-9 shows the flow pattern which presents the typical velocity distribution of turbulent flow.

5.2.1 Temperature Distribution

The maximum temperature in the HTGR reactor is strongly dependent on the power density. To demonstrate the influence of power density, a calculation was done with core power of 25 MW, 65 MW and 100 MW. The temperature distributions under three different core powers are shown in Figure 5-10. The maximum temperatures, corresponding with the core power, are 1500°K , 2200°K and 3000°K, respectively. This is indicates that a core power higher than 100MW is necessary to maintain the gas temperature at about 3000°K. Because of high heat flux the derivative of temperature at the wall is much higher than the derivative of temperature at the center area. The temperature at Q=100 MW grows much faster than temperature at Q=65 MW. The bulk temperature and pressure distributions for different mass fluxes are shown in Figures 5-11 and 5-12, respectively.

5.2.2 Nusselt Number Calculations

Nusselt number correlations are of great importance to calculation of heat transfer. However, almost all of these correlations are developed under fully developed and constant wall heat flux conditions. In some cases the heat flux used for the generation of the experimental data base is rather low. The low wall heat flux indicates small temperature gradient in the flow boundary layer. Therefore the changes in flow properties due to temperature gradient may not be important. Under flow, temperature and heat flux conditions of ultrahigh temperature and compact HTGRs, similar to those

proposed for space power and propulsion applications, the flow is not fully developed, so the temperature gradient could be very large. So, the wall thermal boundary conditions may be different from what is used for the development of the experimental data base used for the derivation of the particular heat transfer empirical correlation. Thus, the detailed computational analysis developed in this work is used to evaluate the most common experimental correlations for wall heat transfer in HTGRs.

Nusselt number variation along the tube length is shown in Figures 5-13 and 5-14. From the results of this study, the Nusselt number increases as the core power increases. The differences of the Nusselt number of core power of 25 MW, 50 MW, 75 MW and 100 MW at x=0.554 m are about 14% and differences of the Nusselt number of mass flux of 45, 60, 75 and 90 kg/m^2.s is about 29.5%. It is interesting to note that the core power and mass flux have similar effects to Nusselt number.

5.2.3 Pressure Drop Calculations

Similarly, simplified equations are used to calculate the pressure drop in heated channels of HTGRs. These equations may or may not be applicable to the flow and thermal conditions of ultrahigh-temperature gas-cooled reactors. An analysis is performed to evaluate the accuracy and validity of the pressure drop equations for HTGRs. Equations which are conveniently used to calculate the accelerational and frictional pressure drop in HTGR cores are:

$$\Delta P = \rho V^2 \left[\left(\frac{T_2}{T_1} - 1 \right) + 2f \frac{\Delta Z}{D} \left(\frac{T_1 + T_2}{2T_1} \right) \right] \tag{5-9}$$

$$\Delta P = \frac{RG^2 T_m}{P_m} \left(\ln \frac{\rho_1}{\rho_2} + 2f \frac{\Delta Z}{D} \right) \tag{5-10}$$

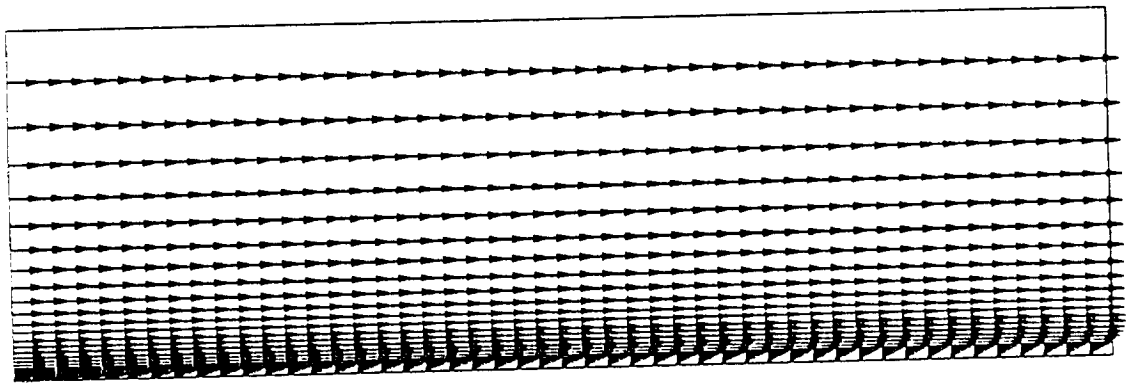

Figure 5-9 Flow pattern for gas cooled reactors.

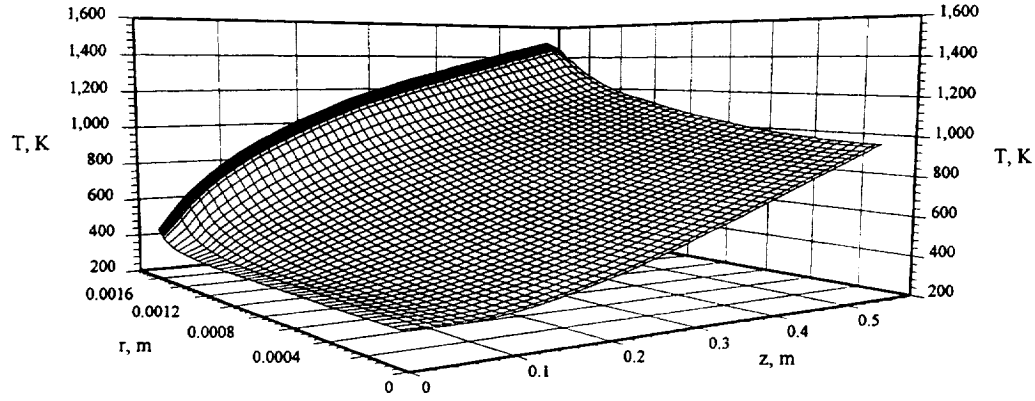

(1)

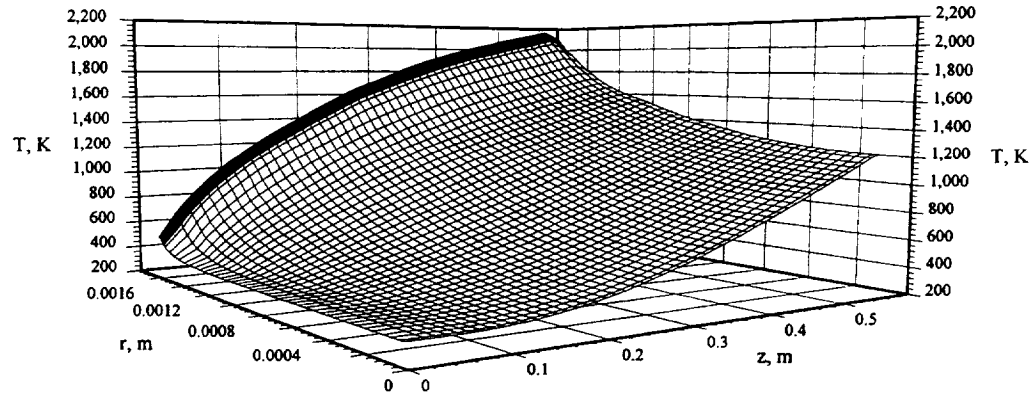

(2)

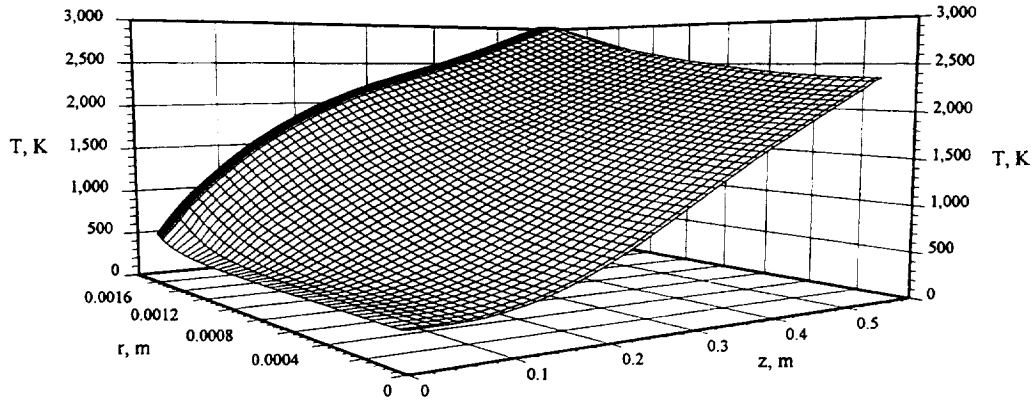

(3)

Figure 5-10 Comparison of temperature distribution for different valued of core power: (1) Q=25 MW, (2) Q=65 MW, (3) Q=100 MW.

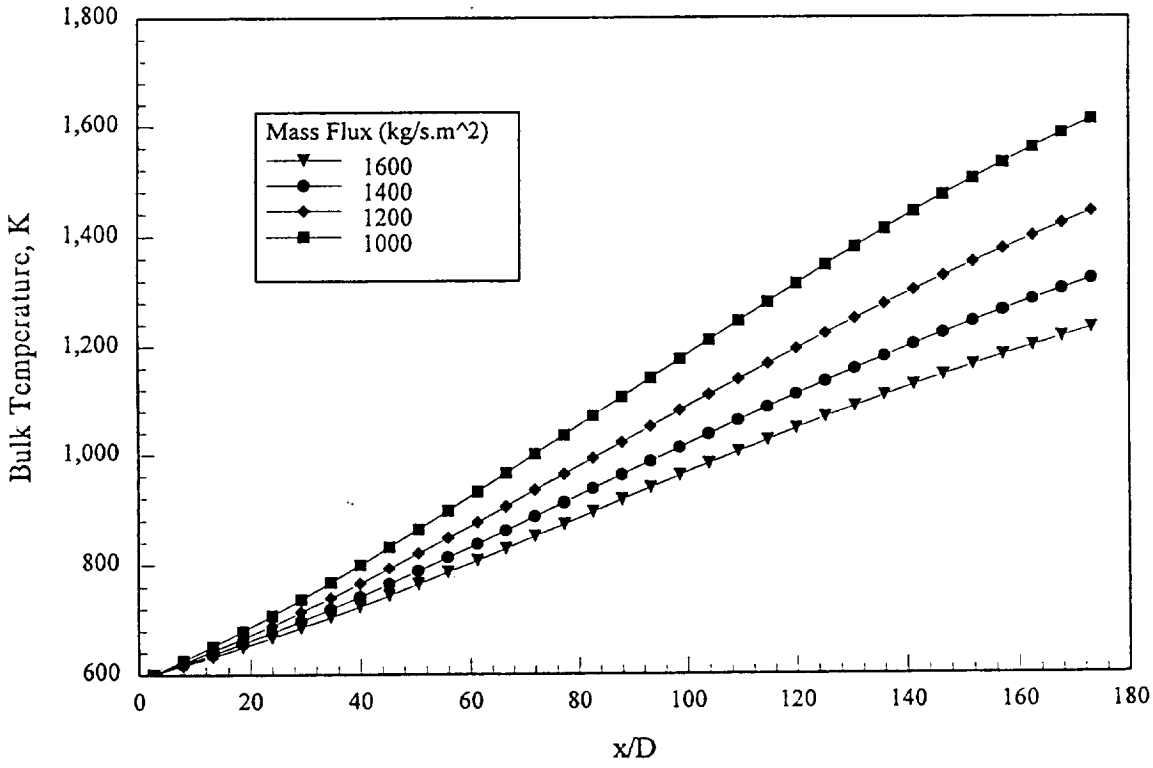

Figure 5-11 Bulk temperature distribution for various mass flux.

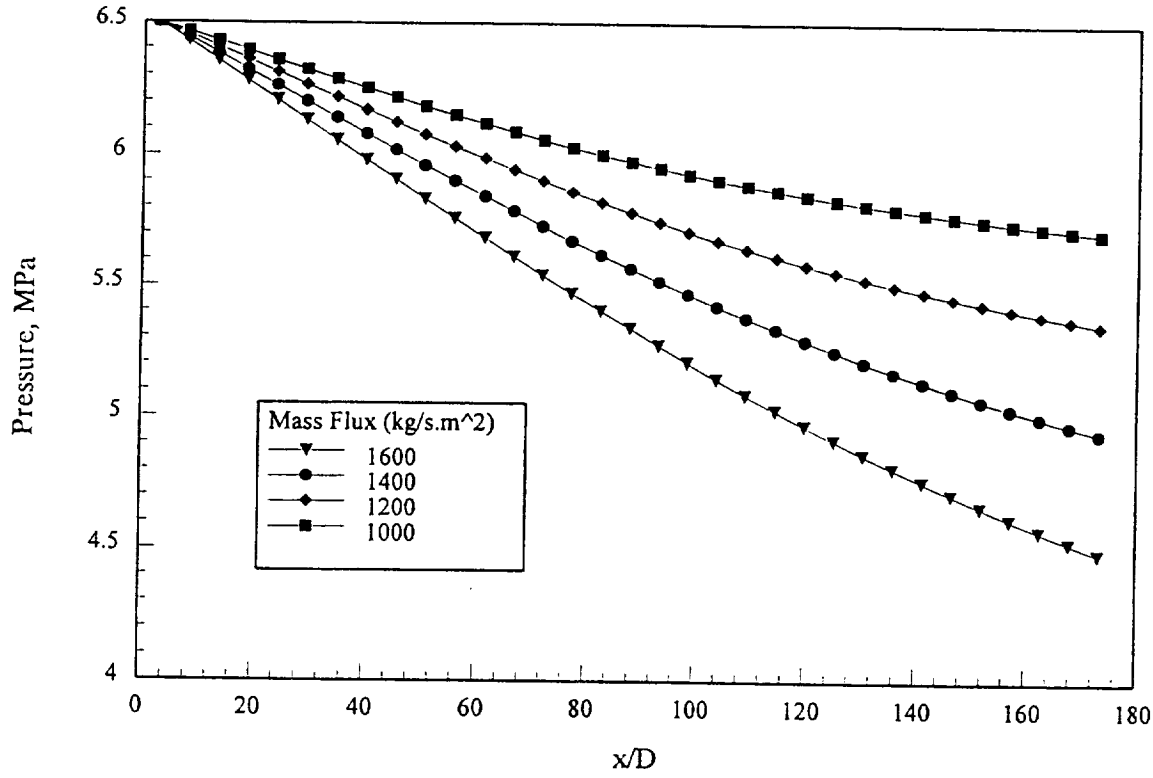

Figure 5-12 Pressure distribution for various mass flux.

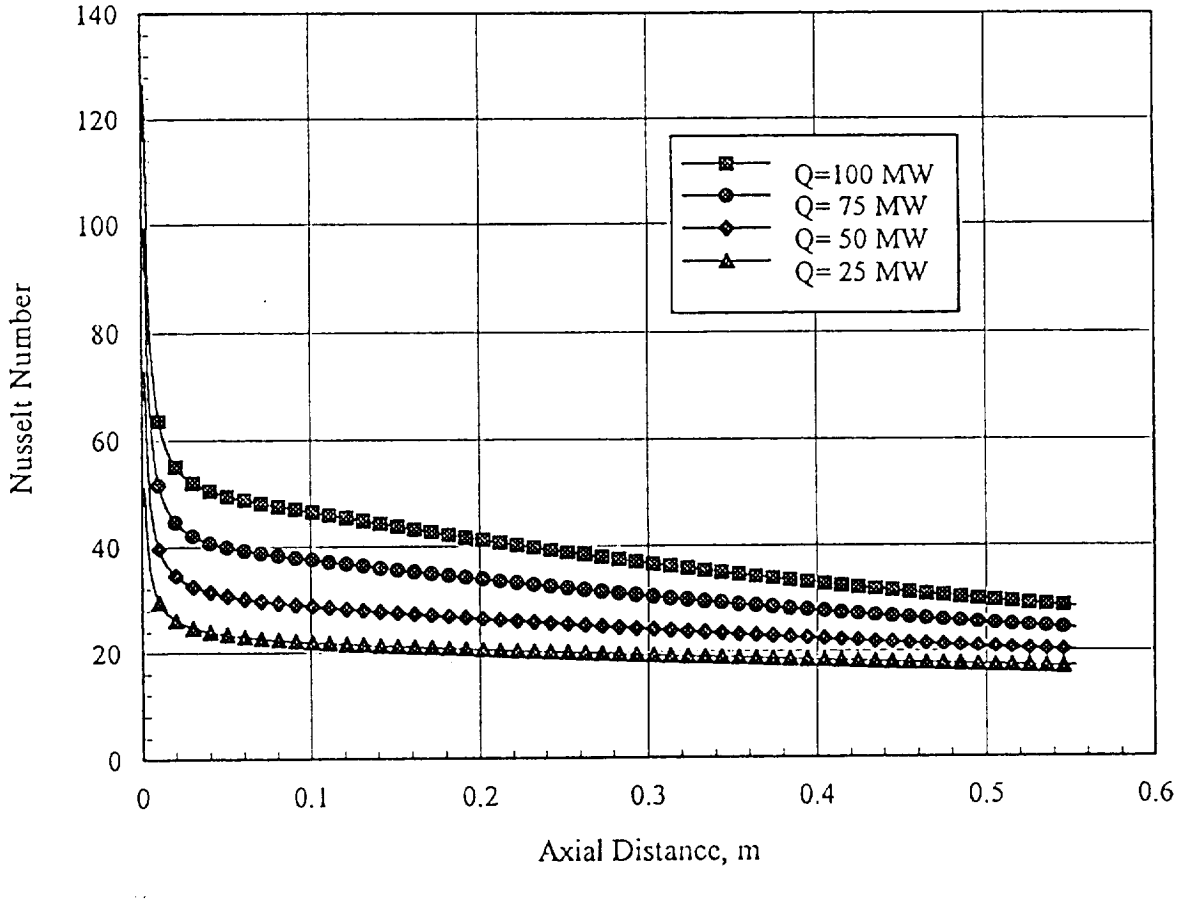

Figure 5-13 Local Nusselt number variation (G=45kg/m^2.s).

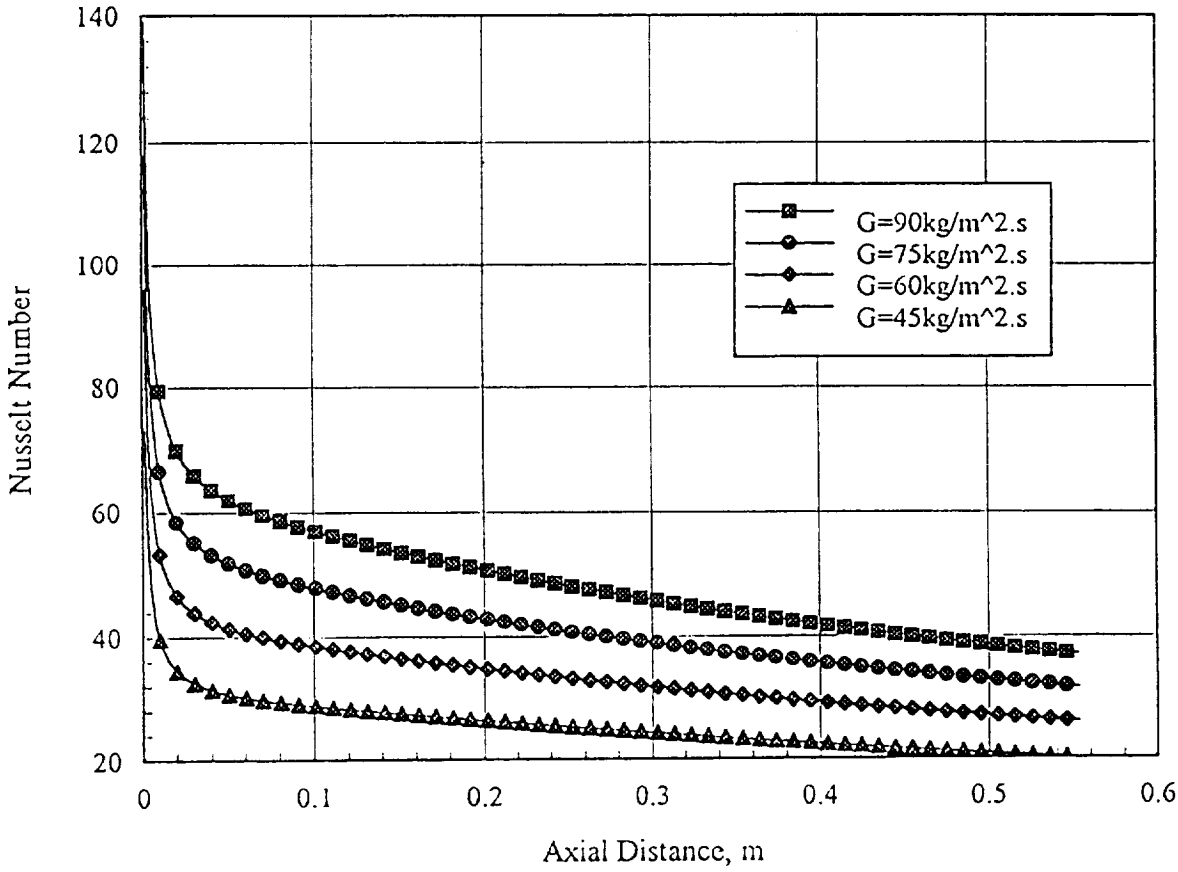

Figure 5-14 Local Nusselt number variation (Q=50 MW).

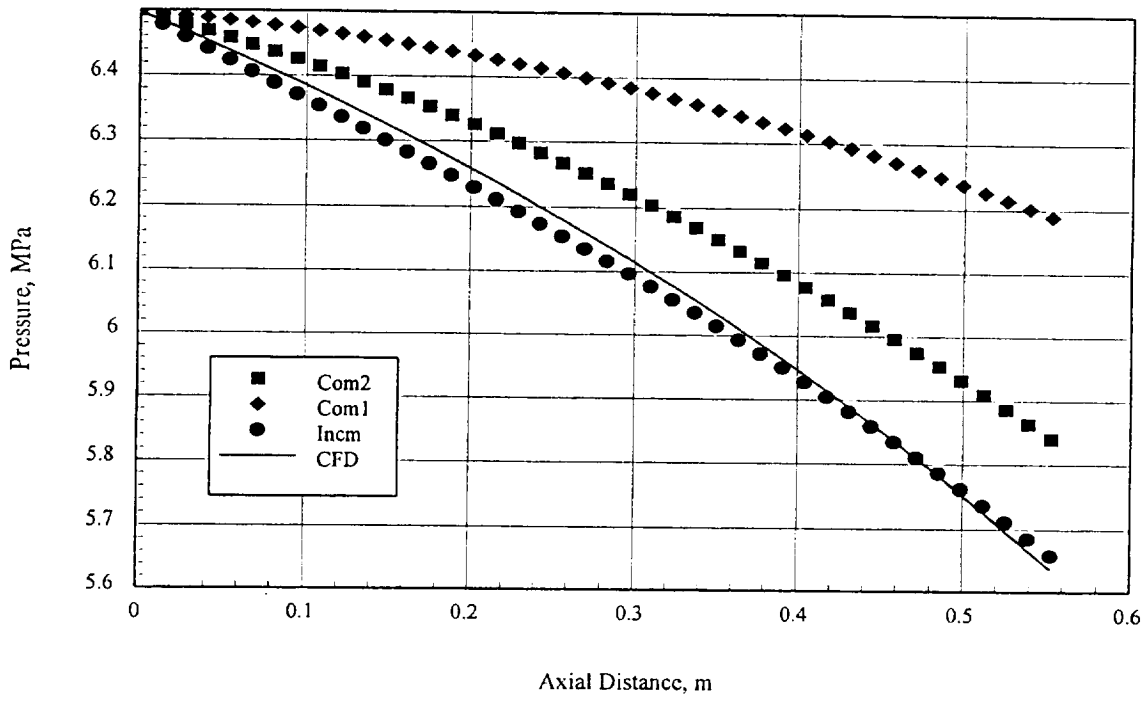

Figure 5-15 Pressure drop correlation comparison.

$$\Delta P = G^2\left[\left(\frac{1}{\rho_2}-\frac{1}{\rho_1}\right)+2f\frac{\Delta Z}{D}\left(\frac{1}{\rho_m}\right)\right] \qquad (5\text{-}11)$$

Figure 5-15 shows the axial pressure distribution in the heated flow channel as calculated by the detailed Navier-Stokes solver and also by Equations (5-9), (5-10) and (5-11). In Figure 5-15, Incm implies equation (5-9) which is found in Reference [2]; Com1 implies equation (5-10) and Com2 implies equation (5-11) which can be found in Reference [22]. From this analysis it is evident that the equation (5-9) provided the best agreement with the numerical results. This is mainly due to the fact that the thermal evolution of the flow is taken into account in the equation (5-9), which is much closer to the governing equation used for the CFD calculation.

5.3 Calculations for XNR2000 Nuclear Rocket Core

The XNR2000 is a fast-spectrum cermet-fueled nuclear reactor that heats hydrogen in a two-pass folded-flow configuration and delivers the hydrogen propellant to the nozzle chamber before expansion through a nozzle.[14] The total engine flow rate is 12.1 kg/s and cycle operates at a chamber pressure and temperature of 5.5 MPa and 2850°K. The engine delivers 111.2kN of thrust at a thrust to weight ratio of 5.1 and a specific impulse of 944 seconds including kinetic and boundary layer effects in the nozzle. The XNR2000 reactor core consists of 90 fuel elements in the outer core and 61 in the inner core. the equivalent inner core diameter is 29.2 cm while that of the outer core is 45.94 cm.

This study considers a turbulent flow of hydrogen in a circular tube with a variety of thermal boundary conditions. The computational models are used to evaluate and compare the applicability of a number of widely used correlations for Nusselt number to the high temperature and high heat flux conditions of hydrogen cooled nuclear rocket

cores. In these systems the surface heat flux ranges from 10 to 1000 MW/m^2 , the flow channel outlet temperature can be as high as 3200^o K, the ratio between diameter and total length varies from 150 to 1000 and the Reynolds number of the flow is in the range of 10^4 to 10^6 . The total flow length in this design is 0.55 m, and the tube diameter is 0.0032m resulting in L/D=165. The grid mesh is 90x50. A stagnation inlet pressure of 6.85 MPa and an back pressure of 6.55 MPa are used. The thermal boundary conditions and Reynolds numbers for two cases considered in this section are listed in following table:

Table 5.1 Thermal conditions and Reynolds number for XNR2000 rocket core.

Case	T_{in} (K)	T_w (K)	q" (MW/m^2)	Reynolds Number
1 (Uniform T_w)	500	500+2300z/L	-	20000
2 (Uniform q'')	500	-	7+15sin(πz/L)	15000

In computation procedure, approximately 1000 time steps and 5 seconds CPU time per time step are required to reach a steady state. The final temperature residual is less than 0.00001.

5.3.1 Non-dimensional Velocity and Temperature Profiles

The non-dimensional velocity profiles for the uniform heat flux boundary condition case are presented in Figure 5-16. It can be seen that the profiles rapidly accelerate very near the wall before flattening out and increase slightly toward the centerline, which is characteristic of turbulent velocity profiles. The flow reached a fully developed state within 20.9 diameters of the entrance. This is very close to the results obtained by Barbin and Jones.[6] The non-dimensional temperature profiles are shown in Figure 5-17. This figure illustrates high temperature gradients at the inlet region and

flattens out downstream as the bulk temperature increases. The temperature profiles achieve fully developed conditions at the approximate 121.9 diameters from the tube entrance. These results indicate that a velocity profile achieves the fully developed regime before a fully developed temperature profile is obtained, that is the thermal entrance length did not exceed the hydrodynamic entrance length. Due to temperature dependent properties used for hydrogen, the temperature profiles shown in Figure 5-17 are slightly different for those predicted for constant properties. Viscosity and thermal conductivity of hydrogen are strong functions of temperature. They lead the values for hydrogen to be significantly different at the wall and at the centerline temperatures.

5.3.2 Nusselt number calculations

The Nusselt number was calculated for both cases listed in the Table 5.1, as shown in Figure 5-19. This figure indicates that the magnitude of Nusselt number appeared to be mainly affected by Reynolds number. The higher the Reynolds number, the higher the Nusselt number. The shapes of the two cases have different characteristics. Downstream of the entrance the Nusselt number gradually increased, after initially decreasing for uniform heat flux case, exhibiting a slight difference with the uniform wall temperature case. It is due to that the trend of Nusselt number for case 1 is mainly dependent upon the magnitude of dT/dr, but for case 2 it is mainly dependent upon the difference between T_w and T_b. So, these different trends between the uniform wall boundary and uniform heat flux boundary result in a slightly different heat transfer mechanism.

Among the long list of correlations for the Nusselt number, four correlations which seem to have more relevance to the heat transfer in a nuclear rocket core are chosen for this analysis. It should be noted that some of these correlations have been developed based on experimental data which are not fully compatible with the boundary conditions used in cases analyzed here. These correlations are used as a point of reference not to

justify the validity of computational results. Figure 5-18 compares the numerical results with four Nusselt number correlations without axial distance and property corrections. These correlations include the Colburn equation, the Gnielinski correlation, the Karman-Boelter-Martinelli equation and the Notter-Sleicher correlation. the Gnielinski correlation[16] is an updated version of the Petukhov-Kirillov correlation[33] where the range of Reynolds number and Prandtl number has been expanded. For the high temperature and high heat flux hydrogen flow cases, a correction factor for the axial distance and real gas property must be used. Figure 5-19 shows a comparison between the numerical results and the Nusselt number correlations when the axial distance and property corrections are applied. The Petukhov-Kirillov-Gnielinski equation, when combined with the Perkins and Worsoe-Schmidt axial distance correction and the Notter-Sleicher property correction has the best agreement with the numerically calculated Nusselt number, differing by less than 3% at the last section measured.

Figures 5-18 and 5-19 vividly show the importance of using distance and property corrections.

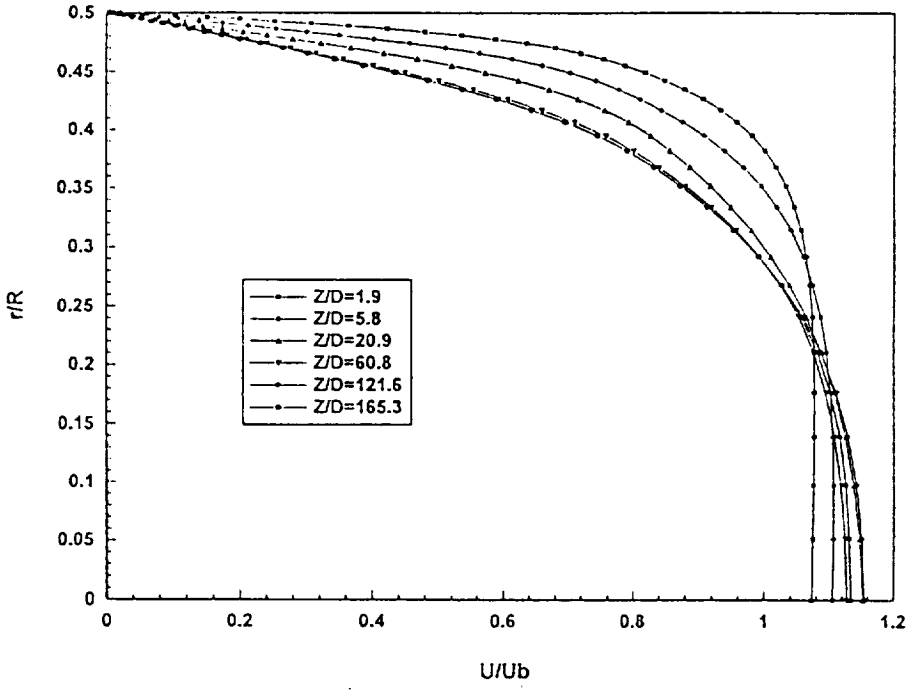

Case 1

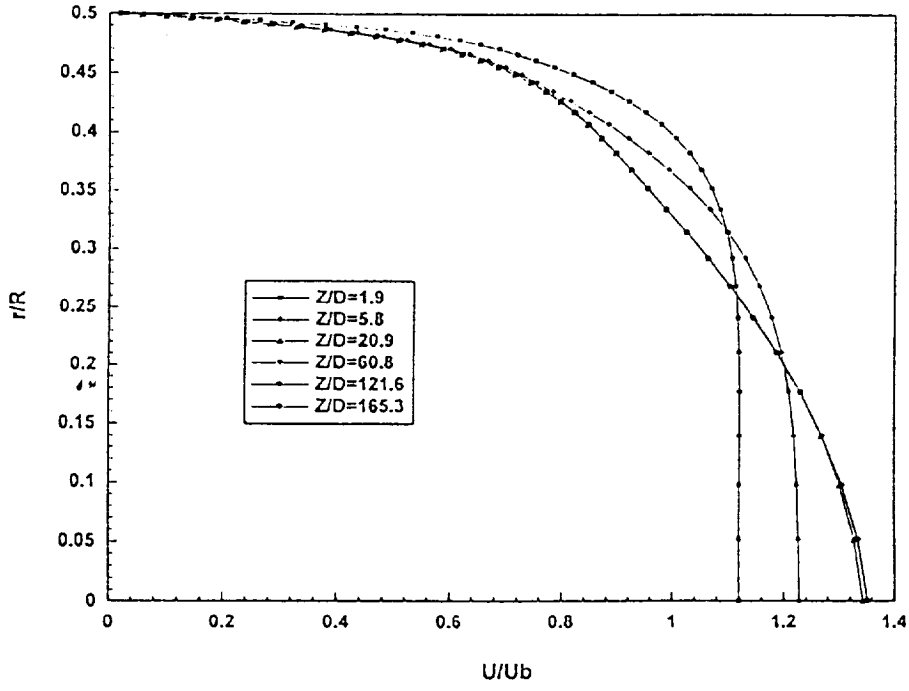

Case 2

Figure 5-18 Non-dimensional velocity profiles at 6 axial locations.

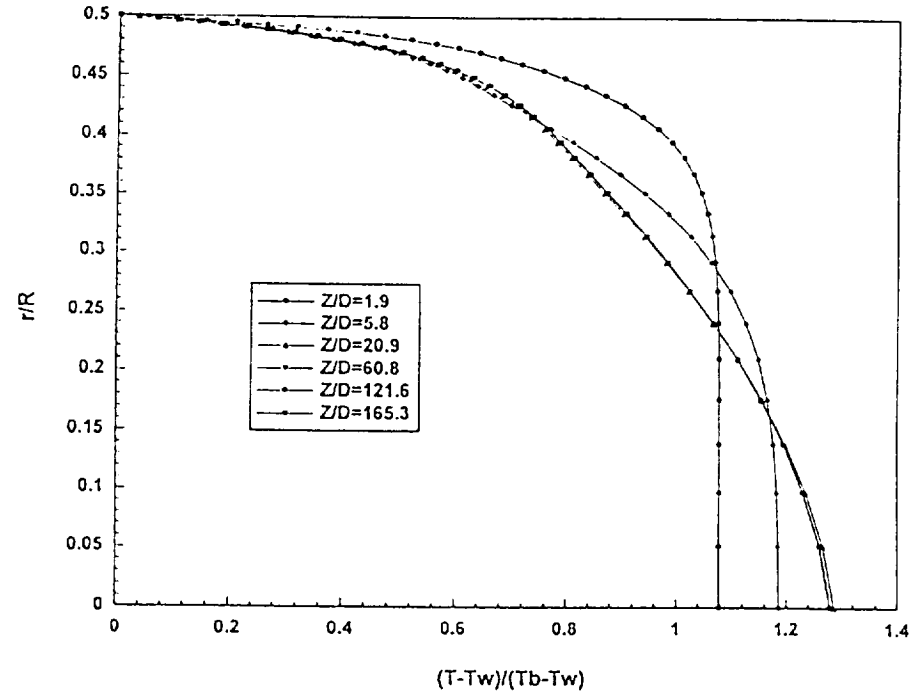

Case 1

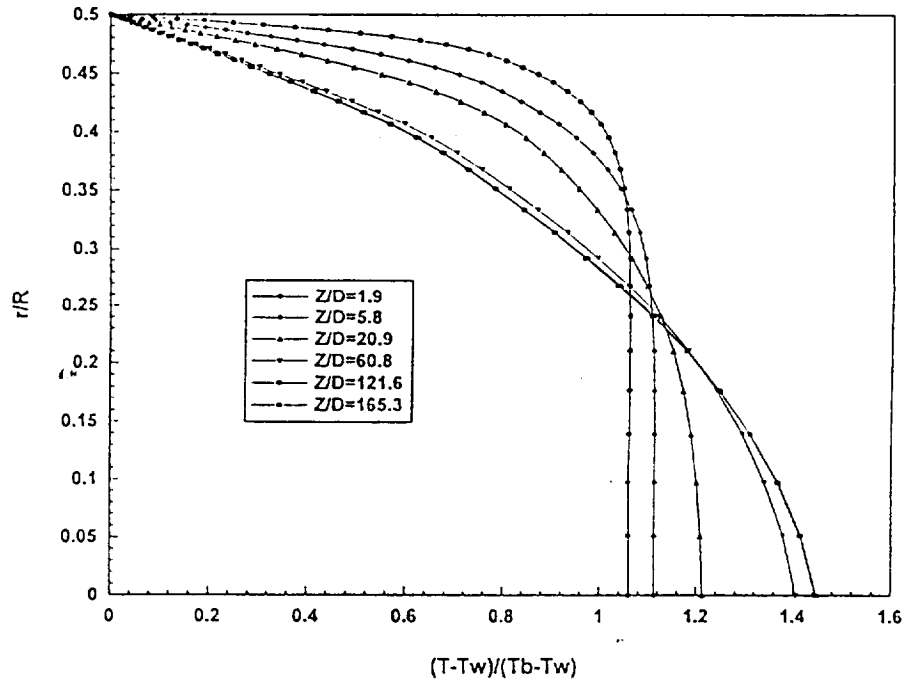

Case 2

Figure 5-19 Non-dimensional temperature profiles at 6 axial locations

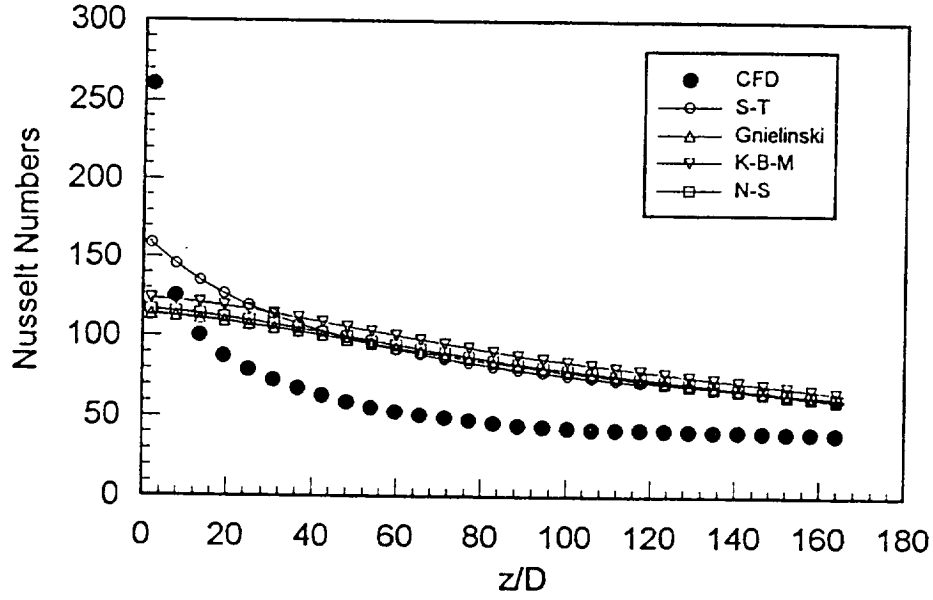

Case 1

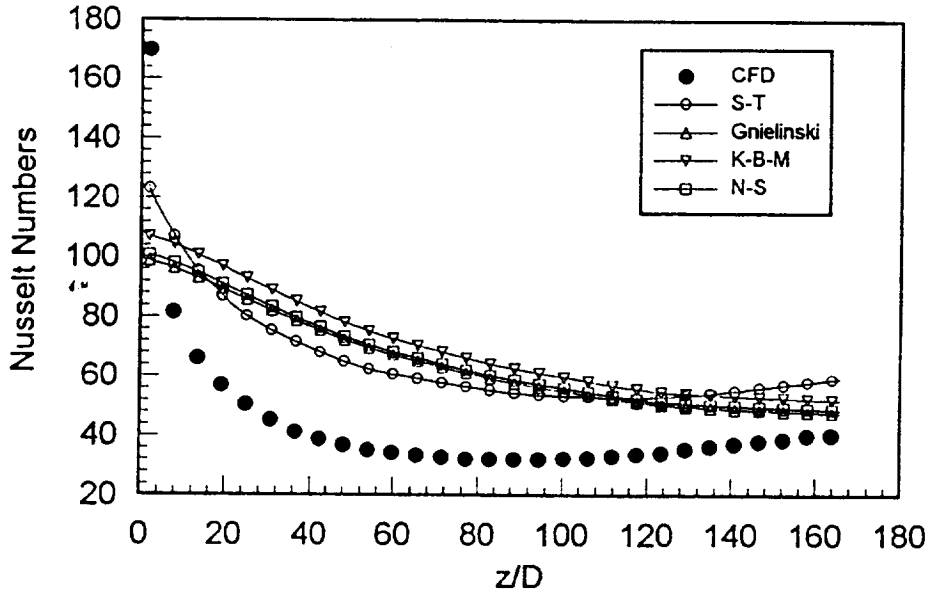

Case 2

Figure 5-20 Comparison of the numerically calculated Nusselt number with the correlations without correction.

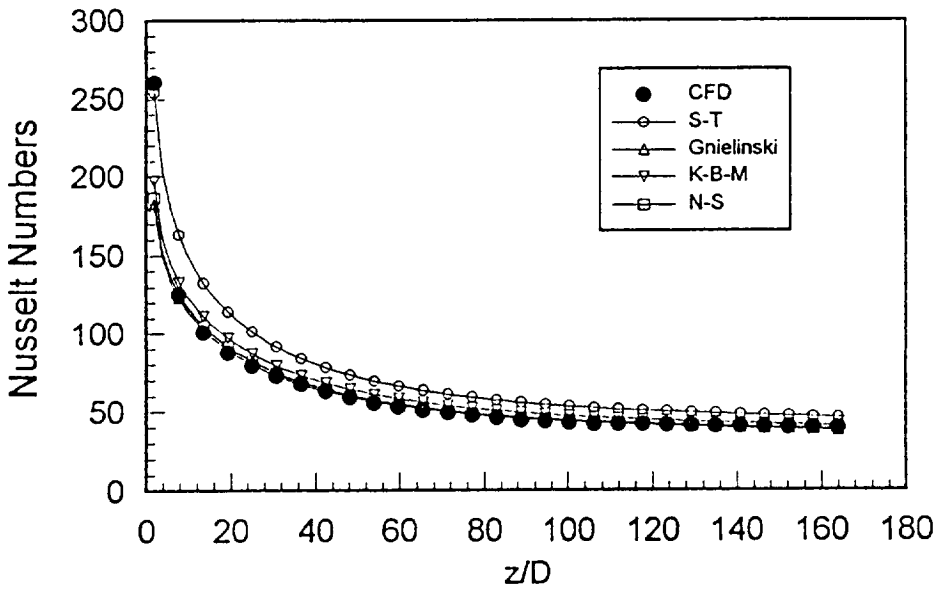

Case 1

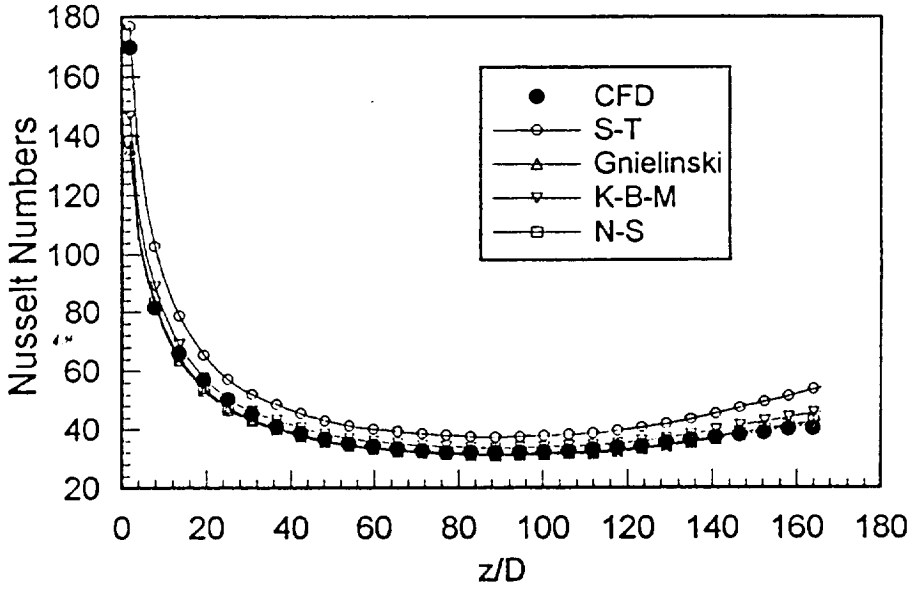

Case 2

Figure 5-21 Comparison of the numerically calculated Nusselt number with the correlations including axial distance and property correction factors.

CHAPTER 6
SUMMARY AND CONCLUSIONS

A computational model based on the axisymmetric, thin-layer Navier-Stokes equations has been proposed to investigate the convective, radiative and conductive heat transfer in nuclear reactors. An implicit-explicit, finite volume, MacCormack method in conjunction with the Gauss-Seidel line iteration procedure is utilized to solve the governing equations. The subsonic and supersonic flows of Hydrogen, Helium and Uranium Tetrafluoride under variable boundary conditions, such as adiabatic, isothermal and constant heat flux, are employed to simulate coolant flow on reactor cores. An enthalpy-rebalancing scheme is implemented to allow the convergence solutions to be obtained with the application of a wall heat flux. A two-dimensional method based on finite element technique is used to investigate the geometric behavior of nuclear reactor fuel elements. Using the developed models the following studies have been completed.

1. Thin layer Navier-Stokes equations Due to the flow field at a high Reynolds number, the thin-layer Navier-Stokes equations are used as the governing equations in this study. In the thin-layer approximation to the full Navier-Stokes equations, the viscosity terms containing derivatives parallel to the body surface, which are in inverse of Reynolds number, are neglected. As a result, a substantial fraction of the available computer storage and time is expended in resolving the normal gradients in the boundary layer. In these calculations, the values of y^+ at nearest the wall are less than 2. So a highly stretched grid system is generated to lead stability and convergence. Good agreement

between the computed results and prior calculations in the literature indicate the validity of the governing equations.

2. Numerical modeling A hybrid implicit-explicit, MacCormack scheme based on the finite volume approach is employed to solve the governing equations. This numerical algorithm has a rapid convergence compared to a simple explicit method. Normally, less than 1000 iterations are needed to reach the steady-state for any flow conditions and any fine grid system taken. MacCormack method is one of the most efficient of the second-order scheme and the most popular two step Lax-Wendroff method for solving problems with shock-capturing schemes. The calculations of this study indicate the good stability, consistency and efficiency.

3. Turbulence model The Baldwin and Lomax two-layer algebraic turbulence model is used in this study. For this turbulence model, the effects of turbulence are simulated in terms of an eddy viscosity coefficient μ_t. Thus, in stress terms of Navier-Stokes equations, the molecular coefficient of viscosity μ is replaced by $\mu+\mu_t$. This model simplifies the calculations of turbulent kinetic energy and eddy diffusivity of energy and avoids the necessity for finding the edge of the boundary layer. It is used to yield faster convergence at reasonable accuracy.

4. Radiative heat transfer model The Rosseland diffusion approximation is used to simulate compressible, turbulent and developing flow of a radiative nongray gas in gas core reactors. A well-known Rosseland mean absorption coefficient is adopted for the approximation, which successfully made use of the diffusion theory in the radiation calculation. This method is simpler to formulate and calculate in radiation heat transfer. Good agreement between the computed results and the previous calculation in the literature indicates the accuracy of the Rosseland radiation model.

5. Thermal conduction model A Finite Element code ANSYS is used to investigate the geometric behavior of fuel elements of a reactor core, which include plate, pin, tubular and square lattice honeycomb. Based on the investigation a dimentionless number, δ number, is defined with respect to void parameter α. The δ number can be used to control temperature gradients, which is important for the lifetime of reactor components. The δ number also provides an efficient method to calculate the centerline temperature, instead of the time-consuming CFD procedure.

6. Wall heat transfer model and enthalpy rebalancing scheme Two boundary conditions, constant wall temperature and constant wall heat flux, on the outside surface of straight tube were included within the study. The relation of the boundary conditions is found based on the Fourier's law. The difficulties in obtaining converged solutions with heat flux boundary conditions were addressed. An enthalpy rebalancing scheme was developed. The implementation of the enthalpy balancing scheme allowed convergent solutions to be obtained with the application of a wall heat flux. This method has been proven successful when problems with heat flux boundary condition are to be solved.

7. Validation of modeling The numerical models were used to calculate the separation angle and drag force over a sphere which is bounded in a cylindrical tube. For this classic project, good agreement between numerical results and the measured data in the experiment indicated the validity of the developed models. Many different Nusselt number equation, property corrections and axial distance corrections were investigated to qualify the numerical calculation. Results demonstrated that the Petukhov-Kirillov-Gnielinski equation combined with Perkins and Worsoe-Schmidt axial distance correction and the Notter-Sleicher property correction is the most relevant to this study. This results also implied the assessment of the numerical models.

8. Internal heat generation The effect of internal heat generation on the heat transfer in the gas core reactors is examined for a variety of power densities, 100W/cc, 500W/cc and 1000W/cc. The maximum temperature, corresponding with the heat generation rates, are 2150°K , 2750°K and 3550°K, respectively. This analysis shows that the maximum temperature is strongly dependent on the value of heat generation rate and also indicated that a heat generation rate higher than 1000W/cc is necessary to maintain the gas temperature at about 3500°K, which is typical temperature required to achieve high efficiency in the gas core reactors.

9. Convective and radiative heat flux The convective and radiative heat fluxes are predicted for the gas core reactors. The maximum value of heat flux occurs at the exit of the reactor core. Radiative heat flux increases with higher wall temperature. This behavior is due to the fact that the radiative heat flux is strongly dependent on wall temperature. This study also found that at temperature close to 3500°K the radiative heat flux is comparable with the convective heat flux.

The above accomplishments clearly demonstrate that the numerical model for convective, conductive and radiative heat transfer has the ability to simulate the heat transfer performance of nuclear reactor cores. This model can be used to predict the important information about heat transfer in nuclear reactor systems, and to qualify the classic empirical correlations which have been used for many years. There is no doubt that the numerical model is a reliable computational tool for heat transfer analysis in nuclear reactor analysis.

REFERENCES

[1] Anderson, D. A., Tannehill, J. C. and Pletch, R. H., Computational Fluid Mechanics and Heat Transfer, Hemisphere Publishing Corporation, 1984.

[2] Anghaie, S., "Reactor Thermal Hydraulics," Class Notes, University of Florida, Gainesville, Florida, 1992.

[3] Anghaie, S., "Thermophysical Properties of UF_4 at High Temperatures (1,000°K <T<10,000°K)", Internal Report, University of Florida, Gainesville, 1992.

[4] Anghaie, S., Feller, G. J., Peery, S. D. and Parsley, C., "A Numerical Simulation Package for Analysis of Neutronics and Thermal Fluids of Space Nuclear Power and Propulsion Systems", American Institute of Physics, 1993.

[5] Baldwin, B. S. and Lomax, H., "Thin Layer Approximation and Algebraic Model for Separated Turbulent Flows", AIAA 16th Aerospace Sciences Meeting, Huntsville, Alabama, AIAA 78-257, pp. 1-15, 1978.

[6] Barbin, A. R. and Jones, A. R., "Turbulent Flow in Inlet Region of a Smooth Pipe", Journal of Basic Engineering, 10(1), pp. 29-34, 1963.

[7] Briley, J. and McDonald, H., "Solution of the Three-dimensional Compressible Navier-Stokes Equations by an Implicit Technique", Proceeding of 4th International Conference on Numerical Method in Fluid Dynamics, New York, pp. 35-38, 1975.

[8] Chakravarthy, S. R., "Relaxation Methods for Unfactored Implicit Upwind Schemes", AIAA Paper No. 84-0165, 1984.

[9] Chiang, S. T., Hoffmann, K. A. and Rutledge, W. H., "Comparison of Flux-Vector Splitting Schemes for Finite Difference and Finite Volume Technique," AIAA Paper No. 91-0170, 1991.

[10] Chung, S. W., "Analysis of Radiative and Convective Energy Transport Processes in Ultrahigh Temperature Vapor Core Reactors", Ph.D. dissertation, University of Florida, Gainesville, 1992.

[11] Chung, S. W. and Anghaie, S., "A Computational Model for Determination of Wall Heat Transfer Rate Due to Flow of Very High Temperature, Optically Thick Gas",

NURETH-5, Proceedings of Fifth International Topical Meeting on Reactor Thermal Hydraulics, Salt Lake City, UT, 1992.

[12] Dam, H. V. and Hoogenboom, J. E., "Physics of a Gaseous Core Reactor", Nuclear Technology, 10(3), pp. 359-368, 1983.

[13] Diaz, N. J., Anghaie, S., Dugan, E. T. and Maya, I., "Ultrahigh Temperature Reactor and Energy Conversion Research Program", INSPI proposal to AFWAL, 1988.

[14] Feller, G. J., "Nuclear Design Methodology of a Compact Fast-Spectrum Beryllium-Reflected Reactor", Ph. D. dissertation, University of Florida, Gainesville, 1994.

[15] Given, A. J., "Engine System Simulation and Core Thermo-Fluid Dynamics of Nuclear Thermal Propulsion Rockets", Master's thesis, University of Florida, Gainesville, 1993.

[16] Grielinski, V., "New Equations for Heat and Mass Transfer in Turbulent Pipe and Channel Flow", International Chemical Engineering, 16(2), pp. 359-368, 1976.

[17] Hoffmann, K. A., Computational Fluid Dynamics for Engineers, Engineering Education System, Austin, Texas, 1989.

[18] Hoogenboom, J. E., Dam, H. V. and Kuijper, J. C., "The Temperature Distribution in A Gas Core Fission Reactor", Annuals of Nuclear Energy, 18(4), pp. 183-195, 1991.

[19] Hosegood, S. B.., "Development of Very High Temperature Reactors for Process Heat Supply", Proceedings of the International Conference on High Temperature Reactor and Process Applications, London, England, pp. 242-250, 1974.

[20] Hrisch, C., Numerical Computation of Internal and External Flows, John Wiley and Sons, New York, Vol. 2, 1994.

[21] Im, K. H. and Ahluwalia, R. K., "Combined Convection and Radiation in Rectangular Ducts", International Journal of Heat and Mass Transfer, 27(2), pp. 221-231, 1984.

[22] Kays, W. M. and Perkins, H. C., "Forced Convection Internal Flow in Ducts", Handbook of Heat Transfer Fundamentals, McGraw-Hill, New York, 1985.

[23] Knight, D. D., "A Hybrid Explicit-Implicit Numerical Algorithm for the Three-Dimensional Compressible Navier-Stokes Equations", AIAA Journal, 22(8), pp. 1056-1063, 1984.

[24] Kumar, R., "Drag Measurement on a Suspended Sphere and Its Application to Corrosive Gas Viscosity Measurement", Ph.D. dissertation, University of Florida, Gainesville, 1992.

[25] Lawrence, S. L. and Tannehill, J. C., "Application of the Implicit MacCormack Scheme to the Parabolized Navier-Stokes Equations", AIAA Journal, 22(12), pp. 1755-1763, 1984.

[26] MacCormack, R. W., "The Effect of Viscosity in Hypervelocity Impact Cratering", AIAA Paper No. 69-354, 1969.

[27] MacCormack, R. W., "A Numerical Method for Solving the Equations of Compressible Viscous Flow", AIAA Journal, 20(9), 1982.

[28] MacCormack, R. W., "Current Status of Numerical Solutions of the Navier-Stokes Equations", AIAA 23rd Aerospace Science Meeting, Reno, Nevada, AIAA Paper 85-032, pp. 1-21, 1985.

[29] Napolitano, M. and Walters, R. W., "An Incremental Block-Line-Gauss-Seidel Method for the Navier-Stokes Equations", AIAA Paper 85-0033, 1985.

[30] Oliver, C. C. and Dugan, E. T., "Thermophysical Properties of UF_6-He Mixture Relevant to Circulating Gas Core Reactor Systems", Nuclear Technology, 69(2), May, 1985.

[31] Ozisik, M. N., Heat Conduction, John Wiley and Sons, New York, 1980.

[32] Patch, R., "Status of Opacity Calculations for Application to Uranium-Fueled Gas-Core Reactor", Proceedings of Symposium on Research on Uranium Plasma and Their Technological Applications, University of Florida, Gainesville, Florida, pp. 165-171, 1970.

[33] Petukhov, M., "Heat Transfer and Friction in Turbulent Pipe Flow with Variable Physical Properties", Advances in Heat Transfer, Academic, New York, pp. 503-564, 1970.

[34] Reynolds, W. C., Thermodynamic Properties in SI, Stanford University, Stanford, California, 1982.

[35] Schlichting, H., Boundary Layer Theory, McGraw-Hill, Inc., 1979.

[36] Schwartz, H. R., "Numerical Analysis, A Comprehensive Introduction", John Wiley and Sons Ltd., 1989.

[37] Seo, T., Kaminski, D. A. and Jensen, M. K., "Combined Convection and Radiation in Simultaneously Developing Flow and Heat Transfer with Nongray Gas Mixtures", Numerical Heat Transfer, 26(1), pp. 49-66, 1994.

[38] Shah, R. K. and Johnson, R. S., "Correlations for Fully Developed Turbulent Flow through Circular and Noncircular Channels", Proceedings of the 6th International Heat and Mass Transfer Conference, Madras, India, pp. 75-96, 1981.

[39] Siegel, R. and Howell, J. R., Thermal Radiation Heat Transfer, Hemisphere Publishing Corporation, 1981.

[40] Soufiani, A. and Taine, J., "Application of Statistical Narrow-Band Model to Coupled Radiation and Convection at High Temperature", International Journal of Heat and Mass Transfer, 30(3), pp. 437-447, 1987.

[41] Steger, J. L. and Warming, R. F., "Flux Vector Splitting of the Inviscid Gas Dynamic Equations with Application to Finite-Difference Methods", NASA TM D-78605, 1979.

[42] Sparrow, E. M., and Cess, R. D., Radiation Heat Transfer, Hemisphere Publishing Corporation, 1978.

[43] Sutton, G. W., and Sherman, A., Engineering Magnetohydrodynamics, McGraw-Hill, Inc., 1965.

[44] Todreas, N. E., and Kazimi, M. S., Nuclear System (I), Thermal Hydraulic Fundamentals, Hemisphere Publishing Corporation, New York, 1990.

[45] Vargaftik, N. B., Handbook of Physical Properties of Liquids and Gases, Hemisphere Publishing Corporation, 1987.

[46] Viegas and Rubesin, M. W., "On the Use of Wall Function as a Boundary Conditions for Two-dimensional, Separated Compressible Flows", AIAA 23rd Aerospace Sciences Meeting, Reno, Nevada, AIAA 85-0180, pp. 1-11, 1985.

[47] Viskanta, R. and Grosh, R. J., "Boundary Layer in Thermal Radiation Absorbing and Emitting Media", International Journal of Heat and Mass Transfer, 5(4), pp. 759-806, 1962.

REPORT DOCUMENTATION PAGE

Form Approved
OMB No. 0704-0188

1. AGENCY USE ONLY (*Leave blank*)	2. REPORT DATE	3. REPORT TYPE AND DATES COVERED
	April 1996	Final Contractor Report

4. TITLE AND SUBTITLE

A Computational Fluid Dynamic and Heat Transfer Model for Gaseous Core and Gas Cooled Space Power and Propulsion Reactors

5. FUNDING NUMBERS

WU-233-01-0N
C-NAS3-26314

6. AUTHOR(S)

S. Anghaie and G. Chen

7. PERFORMING ORGANIZATION NAME(S) AND ADDRESS(ES)

University of Florida
Ultrahigh High Temperature Reactor and Energy Conversion Program
Innovative Nuclear Space Power and Propulsion Institute
Gainesville, Florida 32611

8. PERFORMING ORGANIZATION REPORT NUMBER

E-9882

9. SPONSORING/MONITORING AGENCY NAME(S) AND ADDRESS(ES)

National Aeronautics and Space Administration
Lewis Research Center
Cleveland, Ohio 44135-3191

10. SPONSORING/MONITORING AGENCY REPORT NUMBER

NASA CR-198389

11. SUPPLEMENTARY NOTES

Project Manager, Harvey S. Bloomfield, Power Technology Division, NASA Lewis Research Center, organization code 5440, (216) 433-6131.

12a. DISTRIBUTION/AVAILABILITY STATEMENT

Unclassified - Unlimited
Subject Categories 20 and 66

This publication is available from the NASA Center for Aerospace Information, (301) 621-0390.

12b. DISTRIBUTION CODE

13. ABSTRACT (*Maximum 200 words*)

A computational model based on the axisymmetric, thin-layer Navier-Stokes equations is developed to predict the convective, radiation and conductive heat transfer in high temperature space nuclear reactors. An implicit-explicit, finite volume, MacCormack method in conjunction with the Gauss-Seidel line iteration procedure is utilized to solve the thermal and fluid governing equations. Simulation of coolant and propellant flows in these reactors involves the subsonic and supersonic flows of Hydrogen, Helium and Uranium Tetrafluoride under variable boundary conditions. An enthalpy-rebalancing scheme is developed and implemented to enhance and accelerate the rate of convergence when a wall heat flux boundary condition is used. The model also incorporated the Baldwin and Lomax two-layer algebraic turbulence scheme for the calculation of the turbulent kinetic energy and eddy diffusivity of energy. The Rosseland diffusion approximation is used to simulate the radiative energy transfer in the optically thick environment of gas core reactors. The computational model is benchmarked with experimental data on flow separation angle and drag force acting on a suspended sphere in a cylindrical tube. The heat transfer is validated by comparing the computed results with the standard heat transfer correlations predictions. The model is used to simulate flow and heat transfer under a variety of design conditions. The effect of internal heat generation on the heat transfer in the gas core reactors is examined for a variety of power densities, 100 W/cc, 500 W/cc and 1000 W/cc. The maximum temperature, corresponding with the heat generation rates, are 2150°K, 2750°K and 3550°K, respectively. This analysis shows that the maximum temperature is strongly dependent on the value of heat generation rate. It also indicates that a heat generation rate higher than 1000 W/cc is necessary to maintain the gas temperature at about 3500°K, which is typical design temperature required to achieve high efficiency in the gas core reactors. The model is also used to predict the convective and radiation heat fluxes for the gas core reactors. The maximum value of heat flux occurs at the exit of the reactor core. Radiation heat flux increases with higher wall temperature. This behavior is due to the fact that the radiative heat flux is strongly dependent on wall temperature. This study also found that at temperature close to 3500°K the radiative heat flux is comparable with the convective heat flux in a uranium fluoride failed gas core reactor.

14. SUBJECT TERMS

Reactor modeling; Heat transfer; Computational fluid dynamics; Nuclear power and propulsion

15. NUMBER OF PAGES

120

16. PRICE CODE

A06

17. SECURITY CLASSIFICATION OF REPORT	18. SECURITY CLASSIFICATION OF THIS PAGE	19. SECURITY CLASSIFICATION OF ABSTRACT	20. LIMITATION OF ABSTRACT
Unclassified	Unclassified	Unclassified	

National Aeronautics and
Space Administration

Lewis Research Center
21000 Brookpark Rd.
Cleveland, OH 44135-3191